



UNIVERSITY OF GRAZ

MASTER THESIS (MSc)

**Ab-initio Investigations of the Electronic
Structure of Armchair Graphene
Nanoribbons on the Au(111) Surface**

Lukas Reicht

supervised by
Peter PUSCHNIG

March 6, 2021

Abstract

Armchair graphene nanoribbons (AGNR) have gained increased attention in the recent years, because it became possible to produce them atomically precise via a bottom-up approach. Due to their tunable band gap, AGNRs have the potential to be used in opto-electronic devices and therefore could replace silicon in specific applications. Given these prospects, it is not surprising, that a fair amount of research has gone into understanding their electronic structure. However there is still a lack in understanding how surfaces affect their electronic structure.

This work tries to fill this gap by investigating the effect of a Au(111) surface on the electronic structure of 7-, 9- and 13-AGNR, which are the AGNRs that are probably the most relevant for technical applications. Special focus is placed on the simulation of angle-resolved photoemission spectroscopy (ARPES) experiments. The ever increasing resolution of ARPES allows the direct measurement of the electronic band structure. In order to understand the results of ARPES experiments, simulations of it are essential. Additionally to the ARPES simulations, various other aspects of the AGNRs were investigated with ab-initio simulations. These include the electronic band structure, density of states (DOS), band gap, adsorption position on Au(111), adsorption height and charge density.

To perform these ab-initio investigations, density functional theory (DFT) is employed in this work. Using the Kohn-Sham orbitals from the DFT simulation, the photoemission intensities of ARPES experiments were calculated. Simulated ARPES band and momentum maps of 7-AGNR/Au(111) are compared to multiple experiments. They consistently show good agreement, thereby confirming the validity of the used methods.

Kurzzusammenfassung

Armchair-Graphen-Nanobänder (AGNR) haben in den letzten Jahren erhöhte Aufmerksamkeit erlangt, da es möglich wurde, sie über einen Bottom-up-Ansatz atomar präzise herzustellen. Aufgrund ihrer anpassbaren Bandlücke haben AGNRs das Potenzial, in opto-elektronischen Bauelementen eingesetzt zu werden und könnten daher Silizium in bestimmten Anwendungen ersetzen. In Anbetracht dieser Aussichten ist es nicht verwunderlich, dass bereits viel Forschung betrieben wurde, um ihre elektronische Struktur zu verstehen. Allerdings gibt es immer noch eine Lücke im Verständnis, wie Oberflächen ihre elektronische Struktur beeinflussen.

Diese Arbeit versucht, diese Lücke zu schließen, indem sie den Einfluss einer Au(111)-Oberfläche auf die elektronische Struktur von 7-, 9- und 13-AGNR untersucht, also der AGNRs, die für technische Anwendungen wahrscheinlich am relevantesten sind. Besonderes Augenmerk wird dabei auf die Simulation von winkelaufgelösten Photoemissionsspektroskopie (ARPES)-Experimenten gelegt. Die immer höhere Auflösung der ARPES erlaubt die direkte Messung der elektronischen Bandstruktur. Um die Ergebnisse von ARPES-Experimenten zu verstehen, sind deren Simulationen unerlässlich. Zusätzlich zu den ARPES-Simulationen wurden verschiedene andere Aspekte der AGNRs mit ab-initio-Simulationen untersucht. Dazu zählen die elektronische Bandstruktur, die Zustandsdichte (DOS), die Bandlücke, die Adsorptionsposition auf Au(111), die Adsorptionshöhe und die Ladungsdichte.

Um die ab-initio-Simulationen durchzuführen, wird in dieser Arbeit die Dichtefunktionaltheorie (DFT) verwendet. Mit Hilfe der Kohn-Sham-Orbitale aus der DFT-Simulation wurden die Photoemissionsintensitäten der ARPES-Experimente berechnet. Die ARPES-Simulationen stimmen großteils mit den Experimenten überein und bestätigen damit die Gültigkeit der verwendeten Methoden.

Contents

1	Introduction	1
2	Methodological Background	2
2.1	Density Functional Theory	2
2.1.1	Cutoff Energy and k-Mesh	4
2.1.2	Approximations to the Exchange-Correlation Potential	5
2.2	VASP and Van der Waal Interactions	6
2.3	ARPES	7
3	Implementation and Computational Details	11
3.1	Initialisation and Relaxation of the freestanding AGNR	12
3.2	Adsorption of AGNR on Au(111)	13
3.3	Convergence	14
4	Results	19
4.1	Choice for Starting Geometry and Thickness of Vacuum Slab	19
4.2	Adsorption Sites of 7-, 9- and 13-AGNR on Au(111)	19
4.2.1	7-AGNR on Au(111)	19
4.2.2	9-AGNR on Au(111)	21
4.2.3	13-AGNR on Au(111)	21
4.2.4	Comparison of Energies and Adsorption Heights	22
4.3	Electronic Structure of 7-AGNR	25
4.3.1	Band Structure and Density of States (DOS)	25
4.3.2	Photoemission Band Maps	28
4.3.3	Photoemission Momentum Maps	37
4.3.3.1	Symmetry Argument for Momentum Maps	37
4.3.3.2	Differences in Momentum Maps due to Adsorption Positions	38
4.3.3.3	Comparison with Senkovskiy et al.	40
4.3.3.4	Additional Comparisons with Experimental Data	40
4.4	Electronic Structure of 9-AGNR	46
4.4.1	Band Structure and DOS	46
4.4.2	Photoemission Band Maps	48
4.4.3	Photoemission Momentum Maps	50
4.5	Electronic Structure of 13-AGNR	52
4.5.1	Band Structure and DOS	52
4.5.2	Photoemission Band Maps	55
4.5.3	Photoemission Momentum Maps	55
4.6	Comparison between 7-, 9- and 13-AGNR	59
4.6.1	Band Gaps	59
4.6.2	Charge Density	60
4.6.3	Momentum Maps of freestanding 7-, 9- and 13-AGNR	61
5	Conclusion	64
6	Acknowledgements	65

1 Introduction

Graphene nanoribbons have gained increasing attention in the recent years, due to their successful bottom-up fabrication and their tunable band gap. While there exist several types of graphene nanoribbons, like zigzag and chevron, this work focuses solely on armchair graphene nanoribbons (AGNR). A fascinating property of AGNRs is that with increasing width of the AGNRs, their band gap is decreased. The typical notation is to label the AGNR by the number of carbon atoms along their short side. For example 7-AGNR in Fig. 6 has a width of 7 carbon atoms. By now, AGNRs with many different widths have been produced: 3-AGNR [1], 5-AGNR [2, 3], 7-AGNR [4], 9-AGNR [5], 13-AGNR [6], 14-AGNR [4], 18-AGNR [7] and 21-AGNR [4]. Considering how recent some of these discoveries are, one can see that it is a very active field of research.

Pursuing a bottom-up approach, AGNRs can be produced atomically precise, as was first shown for the 7-AGNR [8]. This precision is crucial, if one wants to use them in future technology. A possible application of such AGNRs is to produce transistors out of them, which have a lateral feature size of only 1 nm and which are atomically thin [9]. The fabrication of such has been achieved for 7-AGNR, 9-AGNR and 13-AGNR [10, 9]. A good understanding of their electronic structure is required to utilize their potential successfully.

Angle-resolved photoemission spectroscopy (ARPES) is an indispensable tool in understanding the electronic structure of nanostructures. In order to better understand the results of this experimental technique, a simulation of ARPES is needed. Such a simulation from first principles is the main focus of this work. When ARPES is performed, AGNRs are typically produced on a Au(788) surface. This surface forms 3.8 nm wide terraces, which locally look like a Au(111) surface [11]. Said terraces have the advantage that the AGNRs align themselves with the edge of the terrace, which is necessary if one wants to perform ARPES on them. While ab initio calculations of freestanding AGNRs have been performed, such calculations of AGNR on a Au(111) surface have not been carried out yet, at least to the best of the author's knowledge. This work fills this gap by performing density functional theory (DFT) simulations, followed by an ARPES simulation of 7-AGNR, 9-AGNR and 13-AGNR on Au(111). Out of all AGNRs, these three are presumably the most relevant for technical applications.

In addition to the ARPES simulation, other analysis of the electronic structure has been performed using DFT. DFT simulations have become very popular in the recent years. In this formalism the many-body Hamiltonian, given by Eq. 1, is cleverly approximated, thereby allowing an ab-initio simulation of a relatively large number of atoms. DFT allows to calculate a vast number of properties for many interesting systems. In this work, the focus lies on understanding the electronic structure on a fundamental level. Thus, besides the ARPES simulations, the band structure as well as the density of states (DOS) are calculated. Additionally, the band gap, adsorption position on Au(111), adsorption height and charge density are analyzed.

In Sec. 2, an introduction into the used methods is given. In Sec. 3, computational details, the initial geometry and convergence tests are presented. The results of this work are given in Sec. 4. When applicable, they are compared to experiments. Directly after the results are given, they are analyzed.

2 Methodological Background

In this section a brief introduction to density functional theory (DFT) will be given. The approximations made within DFT will be explained, including the generalized gradient approximation (GGA). To supplement this approximation, a correction term accounting for Van der Waal interactions by Grimme et al. [12] is introduced and will be discussed. This presentation of DFT is followed by an introduction to the Vienna ab-initio simulation Package (VASP) [13], which is the software used to perform all DFT calculations in this work. Finally ARPES experiments and their simulation will be explained.

2.1 Density Functional Theory

Using atomic units the Hamiltonian for N electrons and K nuclei reads

$$H = -\frac{1}{2} \sum_{i=1}^N \nabla_i^2 + \sum_{i=1}^N \sum_{j>i}^N \frac{1}{|\mathbf{r}_i - \mathbf{r}_j|} - \sum_{i=1}^N \sum_{k=1}^K \frac{Z_k}{|\mathbf{r}_i - \mathbf{R}_k|} - \frac{1}{2M_k} \sum_{k=1}^K \nabla_k^2 + \sum_{k=1}^K \sum_{l>k}^K \frac{Z_k Z_l}{|\mathbf{R}_k - \mathbf{R}_l|} \quad (1)$$

\mathbf{R}_k denote positions of nuclei, \mathbf{r}_i denote positions of electrons, M_k are the masses of the nuclei and Z_k are the electric charges. These five terms describe from left to right the kinetic energy of the electron T , the electron-electron interaction V_{ee} , the electron-nuclei interaction, the kinetic energy of the nuclei and the nuclei-nuclei interaction. The Born-Oppenheimer approximation is used, which assumes the nuclei to be fixed in space, thereby the next-to-last term in Eq. 1 is ignored and the last term enters the equation only as an additive constant. This approximation is justified by the relatively slow movement of the nuclei due to their higher mass compared to electrons. Then the positions of the nuclei \mathbf{R}_k only enter the equation as parameters and we can rewrite Eq. 1 as

$$H = -\frac{1}{2} \sum_{i=1}^N \nabla_i^2 + \sum_{i=1}^N \sum_{j>i}^N \frac{1}{|\mathbf{r}_i - \mathbf{r}_j|} + \sum_{i=1}^N v(\mathbf{r}_i) = T + V_{ee} + \sum_{i=1}^N v(\mathbf{r}_i) \quad (2)$$

where we have rewritten the electron-nuclei interaction by introducing the external potential

$$v(\mathbf{r}) = - \sum_{k=1}^K \frac{Z_k}{|\mathbf{r} - \mathbf{R}_k|} \quad (3)$$

The basis of DFT is the finding of Hohenberg and Kohn that " $v(\mathbf{r})$ is (to within a constant) a unique functional of $n(\mathbf{r})$; since, in turn, $v(\mathbf{r})$ fixes H we see that the full many-particle ground state is a unique functional of $n(\mathbf{r})$ " [14]. This so-called Hohenberg-Kohn theorem is proven in the following. The Rayleigh-Ritz minimal principle

$$E = \min_{\Psi} \langle \Psi | H | \Psi \rangle \quad (4)$$

states that one gets the energy if this matrix element is minimized by varying the normalized trial function Ψ . It can also be formulated in terms of the electron density $n(\mathbf{r})$

$$n(\mathbf{r}) = N \int \Psi^*(\mathbf{r}, \dots, \mathbf{r}_N) \Psi(\mathbf{r}, \dots, \mathbf{r}_N) d\mathbf{r}_2 \dots d\mathbf{r}_N \quad (5)$$

Two steps are needed: First, for a given trial density $n(\mathbf{r})$ the wave functions resulting in it are varied. These are denoted by $\Psi \rightarrow n(\mathbf{r})$. An energy functional of the density is defined by

$$E[n(\mathbf{r})] = \min_{\Psi \rightarrow n(\mathbf{r})} \langle \Psi | H | \Psi \rangle = \min_{\Psi \rightarrow n(\mathbf{r})} \langle \Psi | T + V_{ee} | \Psi \rangle + \int d^3v(\mathbf{r})n(\mathbf{r}) = F[n(\mathbf{r})] + \int d^3v(\mathbf{r})n(\mathbf{r}) \quad (6)$$

where the Hamiltonian 2 is inserted and the universal function $F[n(\mathbf{r})]$ is introduced. In a second step, the energy functional has to be minimized over all densities

$$E = \min_{n(\mathbf{r})} E[n(\mathbf{r})] = \min_{n(\mathbf{r})} \left\{ F[n(\mathbf{r})] + \int d^3v(\mathbf{r})n(\mathbf{r}) \right\} \quad (7)$$

This equation is the Hohenberg-Kohn minimum principle. Searching for the minimum of this equation with fixed electron number $N = \int d^3r n(\mathbf{r})$ as Lagrangian multiplier yields

$$\delta \left\{ F[n(\mathbf{r})] + \int d^3v(\mathbf{r})n(\mathbf{r}) - \mu \int d^3r n(\mathbf{r}) \right\} = 0 \quad (8)$$

where μ is the Lagrangian parameter. From this expression it follows that

$$\frac{\delta F[n(\mathbf{r})]}{\delta n(\mathbf{r})} + v(\mathbf{r}) = \mu \quad (9)$$

This equation states that the external potential $v(\mathbf{r})$ is (up to a constant μ) uniquely determined by the ground state density $n(\mathbf{r})$. The potential $v(\mathbf{r})$ fixes H , as can be easily seen in Eq. 2. Thus, the full many-particle ground state is a unique functional of $n(\mathbf{r})$, as stated in the Hohenberg-Kohn theorem.

Instead of the wave function, the electron density $n(\mathbf{r})$ is the central quantity in DFT. Building on the Hohenberg-Kohn theorem (Eq. 9) and the Hamiltonian in Eq. 2, a derivation of the Kohn-Sham equations will be presented in the following. These are the central equations, that are solved in a DFT simulation. We introduce an auxiliary system of non-interacting electrons, that has the Hamiltonian

$$H_s = -\frac{1}{2} \sum_{i=1}^N \nabla_i^2 + \sum_{i=1}^N v_s(\mathbf{r}_i) = \sum_{i=1}^N h_s(\mathbf{r}_i) \quad (10)$$

Formally this is a fictitious system without a physical interpretation at this point. Per definition it does not include an electron-electron interaction, like Eq. 2 does. The Hamiltonian can be written as a sum over single particle Hamiltonians $h_s(\mathbf{r}_i)$. The important idea now is, that the so-called Kohn-Sham potential $v_s(\mathbf{r})$ is chosen in such a way that Eq. 10 yields the same electron density $n(\mathbf{r})$ as Eq. 2. Because Eq. 10 is a sum of single particle Hamiltonians, the N -electron wave function can be written exactly as a single Slater determinant $|\Phi\rangle$, which obeys the eigenvalue equation

$$H_s |\Phi\rangle = E |\Phi\rangle \quad (11)$$

We apply the Hohenberg-Kohn minimum principle in the same way as above.

$$E[n(\mathbf{r})] = \min_{\Phi \rightarrow n(\mathbf{r})} \langle \Phi | H_s | \Phi \rangle = \min_{\Phi \rightarrow n(\mathbf{r})} \langle \Phi | T | \Phi \rangle + \int d^3v_s(\mathbf{r})n(\mathbf{r}) = T_s[n(\mathbf{r})] + \int d^3v_s(\mathbf{r})n(\mathbf{r}) \quad (12)$$

The functional $T_s[n(\mathbf{r})]$ was introduced. It describes the kinetic energy of a system of non-interacting electrons. In the same manner as above, the ground state energy can be obtained by minimizing over all densities with fixed electron number N .

$$\delta \left\{ T_s[n(\mathbf{r})] + \int d^3v_s(\mathbf{r})n(\mathbf{r}) - \mu_s \int d^3r n(\mathbf{r}) \right\} = 0 \quad (13)$$

Hence it follows that

$$\frac{\delta T_s[n(\mathbf{r})]}{\delta n(\mathbf{r})} + v_s(\mathbf{r}) = \mu_s \quad (14)$$

Eqs. 9 and 14 can be equated, since the constants μ and μ_s can be absorbed in $v_s(\mathbf{r})$.

$$\frac{\delta F[n(\mathbf{r})]}{\delta n(\mathbf{r})} + v(\mathbf{r}) = \frac{\delta T_s[n(\mathbf{r})]}{\delta n(\mathbf{r})} + v_s(\mathbf{r}) \quad (15)$$

Here we implicitly assume that $n(\mathbf{r})$ is of such a form that it arises both from H as well as from H_s . It turns out that this is no restriction in practical applications. In order to proceed, the universal functional $F[n(\mathbf{r})]$ is split into known parts and the yet unknown part is put into the so-called exchange correlation functional $E_{xc}[n(\mathbf{r})]$.

$$F[n(\mathbf{r})] = T_s[n(\mathbf{r})] + U[n(\mathbf{r})] + E_{xc}[n(\mathbf{r})] \quad (16)$$

$U[n(\mathbf{r})]$ is the Hartree energy. It describes the classical electrostatic self-repulsion of the charge density $n(\mathbf{r})$. Insertion of Eq. 16 into Eq. 15 gives an expression for the Kohn-Sham potential $v_s(\mathbf{r})$

$$v_s(\mathbf{r}) = v(\mathbf{r}) + \frac{\delta U[n(\mathbf{r})]}{\delta n(\mathbf{r})} + \frac{\delta E_{xc}[n(\mathbf{r})]}{\delta n(\mathbf{r})} = v(\mathbf{r}) + v_H([n], \mathbf{r}) + v_{xc}([n], \mathbf{r}) \quad (17)$$

where the Hartree potential $v_H(\mathbf{r})$ and the exchange-correlation potential $v_{xc}(\mathbf{r})$ were introduced. Thus, the Kohn-Sham potential $v_s(\mathbf{r})$ is a sum of the external potential $v(\mathbf{r})$, and Hartree potential $v_H(\mathbf{r})$ and the exchange-correlation potential $v_{xc}(\mathbf{r})$. The Kohn-Sham potential can be used to calculate the single-particle orbitals $\varphi_j(\mathbf{r})$

$$\left[-\frac{1}{2}\Delta + v_s(\mathbf{r})\right]\varphi_j(\mathbf{r}) = \epsilon_j\varphi_j(\mathbf{r}) \quad (18)$$

The eigenstates of this equation are the Kohn-Sham orbitals $\varphi_j(\mathbf{r})$, which are single-particle orbitals. The Kohn-Sham energies ϵ_j are energies of these orbitals and can be interpreted physically via Janak's theorem [15]. The electron density $n(\mathbf{r})$ can be calculated by

$$n(\mathbf{r}) = \sum_{j=1}^N |\varphi_j(\mathbf{r})|^2 \quad (19)$$

Eqs. 17, 18 and 19 are the Kohn-Sham equations, which are at the heart of DFT. The groundbreaking improvement of this formalism is that solving the Kohn-Sham Eqs. 17, 18 and 19 is computationally cheaper than solving 2, since it scales with the electron number cubed N^3 instead of exponentially e^N .

However there are some shortcomings that one has to be aware of:

- The Eqs. 17, 18 and 19 need to be solved self-consistently, i.e. iteratively, since $v_H(\mathbf{r})$ and $v_{xc}(\mathbf{r})$ depend on $n(\mathbf{r})$.
- One starts with an initial guess for the charge density and then minimizes the energy. Therefore DFT is a ground state theory. This means that strictly speaking it describes the system at temperature $T = 0$ K.
- There are still approximations necessary to make the problem tractable. These approximations apply to $v_{xc}(\mathbf{r})$ and will be discussed in Sec. 2.1.2.

A widespread way of solving 17, 18 and 19 for a crystal is to use a plane wave basis set. This means that the Kohn-Sham orbitals are expanded in terms of plane waves, as will be done in the next chapter.

2.1.1 Cutoff Energy and k-Mesh

Without diving into too many details, k-space sampling and cutoff energy will be introduced in the following. Bloch's theorem can be applied in a periodic potential. According to which, solutions of the Schrödinger equation have the form of a Bloch wave

$$\phi_{\mathbf{k}}(\mathbf{r}) = e^{i\mathbf{k}\mathbf{r}} u_{\mathbf{k}}(\mathbf{r}) \quad (20)$$

where $u_{\mathbf{k}}(\mathbf{r})$ is periodic with the periodicity of the supercell, $u_{\mathbf{k}}(\mathbf{r} + \mathbf{G}) = u_{\mathbf{k}}(\mathbf{r})$. It can be expanded in terms of a set of plane waves

$$u_{\mathbf{k}}(\mathbf{r}) = \sum_{\mathbf{G}} c_{\mathbf{G}} e^{i\mathbf{G}\mathbf{r}} \quad (21)$$

with a sum over reciprocal lattice vectors \mathbf{G} . By inserting Eq. 21 into 20, one obtains

$$\phi_{\mathbf{k}}(\mathbf{r}) = \sum_{\mathbf{G}} c_{\mathbf{k}+\mathbf{G}} e^{i(\mathbf{r}+\mathbf{G})\mathbf{r}} \quad (22)$$

This sum extends over infinitely many reciprocal lattice vectors \mathbf{G} , which is of course not practical. Therefore, one approximates this sum by cutting it off at a cutoff G_{cut} .

$$\phi_{\mathbf{k}}(\mathbf{r}) = \sum_{\mathbf{G}}^{|\mathbf{G}+\mathbf{k}| < G_{cut}} c_{\mathbf{k}+\mathbf{G}} e^{i(\mathbf{r}+\mathbf{G})\mathbf{r}} \quad (23)$$

This cutoff is related to a so-called cutoff energy via

$$E_{cut} = \frac{1}{2}G_{cut}^2 \quad (24)$$

It has to be checked, whether the calculation is converged with respect to the cutoff energy. In practice, this means that the result of the calculation should not change significantly, if the cutoff energy is increased any further.

Since Bloch waves in the form of Eq. 23 are in play, integrals of the form

$$g = \int_{BZ} g(\mathbf{k}) d\mathbf{k} \quad (25)$$

arise. This integral is defined in reciprocal space and over all points in the Brillouin zone. The reciprocal space is sampled by a mesh of \mathbf{k} -points. One has to check whether or not the used \mathbf{k} -mesh is sufficiently dense. Convergence tests of the calculations with respect to the \mathbf{k} -mesh as well as the cutoff energy are performed in Sec. 3.3.

For a more detailed introduction to DFT the reader is referred to one of the many books on density functional theory, e.g. the book by Sholl and Steckel [16] for a practical introduction.

2.1.2 Approximations to the Exchange-Correlation Potential

There exist many different approximations to the exchange-correlation potential $v_{xc}(\mathbf{r})$, which can be categorized using the so-called Jacob's ladder in Fig. 1. The higher on the ladder the more computational resources are required, while simultaneously the accuracy of the calculation generally increases. However, this is not always true and for a few cases methods on lower rungs give a more accurate result. The picture presented here is a simplification insofar as there exist more categories than depicted in Fig. 1 and there are also subcategories.

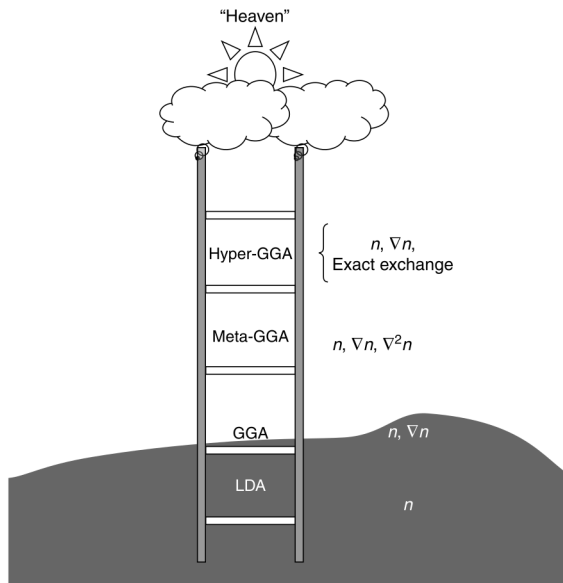


Figure 1: Jacob's Ladder shows different types of functionals leading to the "Heaven of Chemical Accuracy". The picture is taken from the book "Density Functional Theory" by Sholl and Steckel [16].

In the local density approximation (LDA) the exchange correlation potential the same as the one for a spatially uniform electron gas with the same density as the local electron density. Thus it depends only on the electron density n and the exchange correlation energy is given by

$$E_{xc}^{LDA}[n] = \int n(\mathbf{r}) e_{xc}^{unif}(n(\mathbf{r})) d^3 r \quad (26)$$

where $e_{xc}^{unif}(n(\mathbf{r}))$ is the exchange-correlation energy per particle of a uniform electron gas of charge density $n(\mathbf{r})$.

The next higher rung is the generalized gradient approximation (GGA). Here the exchange-correlation potential not only depends on n , but also on the gradient of the electron density ∇n . It is in general more accurate than LDA, because it also takes varying electron densities to some

extent into account. Nevertheless it is relatively fast to compute, allowing many atoms in the supercell. Therefore it is the functional of choice for all simulations made in this work.

The meta-GGA functional depends on n , ∇n , and $\nabla^2 n$. Finally at the fourth rung in Jacob's ladder, there are hyper-GGA functionals, which include contributions of the exact exchange energy together with a GGA functional. As already mentioned, the list of functionals presented here is not exhaustive. For example there exist hybrid functionals, which are any functionals that incorporate the exact exchange. Thus hyper-GGAs can also be referred to as hybrid-GGAs.

2.2 VASP and Van der Waal Interactions

The Vienna Ab initio Simulation Package (VASP) is a software package used to perform DFT simulations. It comprises a variety of methods, but in the following only the ones relevant for this work are considered. VASP has a plane wave basis set, and it uses the projector-augmented wave (PAW) method [17, 18] or ultra-soft pseudopotentials [19, 20]. In this work the former is used. The wave functions near atomic nuclei are hard to describe by plane waves, since they oscillate quickly and thus a large energy cutoff would be necessary. This problem is mitigated by replacing the true potential near to the nuclei by a smooth pseudo-potential. This is justified by the fact that the electrons further away from the nucleus play a more significant role in chemical bonding. The PAW method is a generalization of this pseudopotential approach. In addition the frozen core approximation is applied in all VASP calculations, thereby fixing the core electrons to a reference atomic system.

A general caveat of DFT simulations is that, due to the approximations made to the exchange-correlation functional, they are quite limited when it comes to phenomena that include Van der Waal (vdW) interactions. The exact solution of Eq. 2 would automatically incorporate the exact vdW contribution to the total energy as this contribution is strictly contained in the electron correlation energy. There is a vast number of approaches that try to incorporate vdW interactions [21]. A category of these approaches is called DFT-D, which includes DFT-D1, DFT-D2 and DFT-D3. These three can be seen as three generations of the DFT-D method. The oldest method is the DFT-D1 and the newest, most sophisticated one is the DFT-D3. In VASP one can switch on the DFT-D3 correction of Grimme et al. [12], thereby adding the following energy term:

$$E_{disp} = -\frac{1}{2} \sum_{i=1}^{N_{at}} \sum_{j=1}^{N_{at}} \sum_{\mathbf{L}}' \left(f_{d,6}(r_{ij,L}) \frac{C_{6ij}}{r_{ij,L}^6} + f_{d,8}(r_{ij,L}) \frac{C_{8ij}}{r_{ij,L}^8} \right) \quad (27)$$

where the summation is over all atoms N_{at} and all translations of the unit cell $\mathbf{L} = (l_1, l_2, l_3)$. The prime indicates that $i \neq j$ for $\mathbf{L} = 0$. C_{6ij} denotes the geometry-dependent dispersion coefficients for the atom pair ij . $f_{d,6}(r_{ij,L})$ is a damping function, that is used to avoid unphysical behavior for small distances. $r_{ij,L}$ is the distance between atom i in the reference cell $\mathbf{L} = 0$ and atom j in the cell \mathbf{L} . Eq. 27 includes the first and second correction to the Van der Waal interaction, which scale like $\frac{1}{r^6}$ and $\frac{1}{r^8}$ with the distance between two atoms. Despite this method's popularity, one has to keep in mind that, as Hermann et al. put it, "the spectrum of behaviors of vdW interactions in real materials is vast, reflecting the intricacies of electronic structure theory, and an effort to capture all this complexity purely from geometry is a formidable task" [21]. Nevertheless this method was used, due to its outstanding computational speed and its generally reasonable accuracy.

A benchmark comparison between different vdW methods applied on AGNRs was not found in the literature. However a comparison between the range-separated many-body dispersion (MBD) method, which is among the most accurate methods, and DFT-D3 was made by Blood-Forsythe [22]. It shows that the DFT-MBD method is more accurate than DFT-D3 in predicting the intermonomer distance of benzene monomers. A comparison of the methods applied to the buckyball catcher host-guest complex shows that the distance between the catcher host and the buckyball is 8.45 Å with DFT-D3 and 8.31 Å with DFT-MBD. In lack of a higher level calculation, it cannot be concluded with certainty, which of these two values is closer to the true distance. The DFT-MBD method's computational cost is comparable to the one for DFT-D3, which makes it a possible alternative to the DFT-D3 method.

VASP allows the usage of the GGA version of Perdew, Burke and Ernzerhof (GGA-PBE) [23], which is used in this work.

2.3 ARPES

Angle-resolved photoemission spectroscopy (ARPES) is an experimental technique that can be used to measure the binding energy E_b as well as the wave vector \mathbf{k} of electrons in a solid. In Fig. 2 one can see the basic principle of such an experiment. The light is created by a discharge lamp, a laser or a synchrotron. It hits the sample and an electron is emitted via the photoelectric effect. The electron's kinetic energy E_{kin} is then measured in an energy analyzer. The part of the electron's momentum, that is parallel to the sample's surface is conserved, while the momentum perpendicular to the surface is in general not conserved, however it can be recovered by suitable methods. The component of the electron's momentum, which are parallel to the sample are given by

$$k_x = \sqrt{\frac{2m_e E_{kin}}{\hbar^2}} \sin(\theta) \cos(\varphi) \quad (28)$$

$$k_y = \sqrt{\frac{2m_e E_{kin}}{\hbar^2}} \sin(\theta) \sin(\varphi) \quad (29)$$

with the kinetic energy of the electron E_{kin} and the angles θ and φ as defined in Fig. 2. The binding energy of the electron E_b can be calculated via the formula

$$E_{photon} = E_b + W + E_{kin} \quad (30)$$

E_{photon} is the energy of the incoming photon, which must be larger than the binding energy E_b plus the work function W . The excess energy of the electron is in the form of kinetic energy E_{kin} .

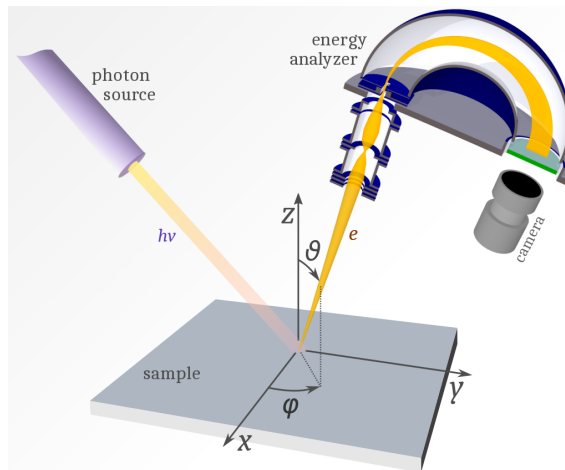


Figure 2: Overview of an ARPES experiment. The picture is copied from [24] and licensed under the Creative Commons Attribution-Share Alike 4.0 International license.

One generally presents the results of such an ARPES experiment as a plot of the photoemission intensity $I(k_x, k_y)$ as a function of k_x and k_y or as $I(E_b, k_x)$ or $I(E_b, k_y)$. The $I(k_x, k_y)$ -plot is synonymously called momentum map or k-map. The $I(E_b, k_x)$ and $I(E_b, k_y)$ -plots are called band maps.

This experiment can be simulated in different ways. For all ARPES simulations in this work a program, which was developed by Peter Puschnig and extended by Daniel Lüftner in his PhD thesis [25], was employed and a derivation of the used method will be given here. In this method it is assumed that the photoemission process happens at an instant, called the "sudden approximation". Additionally, all many-body interactions are ignored. We make use of the one-step model of photoemission, where the excitation and emission of the electron is treated as a single coherent step [26, 27]. We start with Fermi's golden rule for the intensity I

$$I \propto |\langle \Psi_f | H_{int} | \Psi_i \rangle|^2 \times \delta(E_{photon} - E_b - W - E_{kin}) \quad (31)$$

Here, H_{int} describes the interaction between the system and the photon. Ψ_i is the initial state of the system, while Ψ_f is the final state of the system with the outgoing electron. The delta

distribution ensures energy conservation. The Hamiltonian of an electron in an electromagnetic field is

$$\begin{aligned}
H &= \frac{1}{2m_e} \left(\mathbf{p} - \frac{e}{c} \mathbf{A} \right)^2 + eV(\mathbf{r}) = \\
&= \underbrace{\frac{\mathbf{p}^2}{2m_e} + eV(\mathbf{r})}_{H_0} + \underbrace{\frac{e}{2m_e c} (\mathbf{A}\mathbf{p} + \mathbf{p}\mathbf{A}) + \frac{e^2}{2m_e c^2} \mathbf{A}^2}_{H_{int}}
\end{aligned}$$

We neglect the last term with \mathbf{A}^2 , since it can be considered to be small for conventional light sources. Using the commutation relation $[\mathbf{p}, \mathbf{A}] = i\hbar \nabla \mathbf{A}$ and neglecting terms with $\nabla \mathbf{A}$, we can write $\mathbf{A}\mathbf{p} + \mathbf{p}\mathbf{A} = 2\mathbf{A}\mathbf{p}$. Therefore H_{int} is proportional to $\mathbf{A}\mathbf{p}$ and we get

$$I \propto |\langle \Psi_f | \mathbf{A}\mathbf{p} | \Psi_i \rangle|^2 \times \delta(E_{photon} - E_b - W - E_{kin}) \quad (32)$$

The neglect of terms with $\nabla \mathbf{A}$ is not necessarily legitimate for surfaces [27], however as we seek a rather qualitative understanding of ARPES images it is justified. Up to this point the final and initial state wave functions include all electrons. As mentioned, it is assumed that the interaction is instantaneous, leaving all electrons but the interacting one unchanged. We thus assume that there is no interaction between the emitted electron and the rest of the system. Therefore we can factorize the wave function into two independent parts, which are the wave function of the emitted electron ψ_f and the wave function of the $N - 1$ remaining electrons Ψ_f^{N-1} . This product has to be properly antisymmetrized. The same splitting can be done for the initial wave function as well. We thus have a single particle wave function and a sum over electrons i [25, 28]

$$I \propto \sum_i |\langle \psi_f | \mathbf{A}\mathbf{p} | \psi_i \rangle|^2 \times \delta(E_{photon} - E_i - W - E_{kin}) \quad (33)$$

where ψ_i is the initial state of the i th electron and E_i its binding energy.

In order to further simplify the evaluation of Eq. 33, the final state ψ_f is approximated as a plane wave. This yields a very simple equation for the intensity I , in which the Fourier transform of the initial state $\tilde{\psi}_i$ is used.

$$\sqrt{I} \propto |\mathbf{A}\mathbf{k}| \times |\tilde{\psi}_i| \quad (34)$$

As initial states we will use the Kohn-Sham orbitals, which are the result of a DFT calculation. This is yet another approximation. It has been argued, that imaging experiments show Dyson orbitals for which one may simply take Kohn-Sham orbitals as zeroth approximation [28]. Of course another approximation lies within the calculation of Kohn-Sham orbitals, since it cannot be carried out exactly, as is explained in Sec. 2.1.2.

The factor $|\mathbf{A}\mathbf{k}|$ in Eq. 34 contains information about the incidence angle of the photon. This angle could be chosen to be equal to some experiment, that one wants to simulate. In this work it was refrained from doing so, because there is no specific experimental setup, that one wants to reproduce here. Therefore the factor $|\mathbf{A}\mathbf{k}|$ in Eq. 34 was left out in all simulations.

Putting Eq. 34 into practice, Fig. 3 shows how a momentum map is obtained from a DFT simulation. The red hemisphere in this figure has the radius

$$k = \sqrt{\frac{2m_e E_{kin}}{\hbar^2}} \quad (35)$$

It is a surface of constant binding energy, as can be easily seen when comparing Eq. 35 to Eqs. 28 and 29. The steps shown in Fig. 3 are an illustration for a single molecular orbital ψ_i , while in Eq. 33 there is a sum over many initial states i .

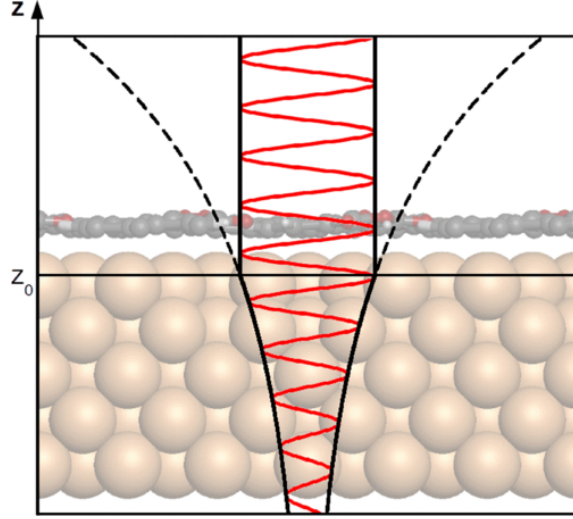


Figure 4: Illustration of the damped wave function, whose formula is given in Eq. 36. This figure was taken from Lüftner et al. [32].

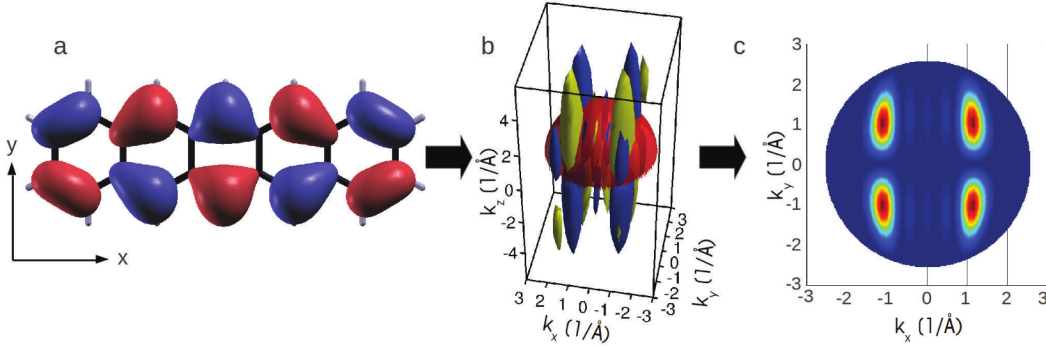


Figure 3: Steps to obtain a simulated ARPES momentum map. a) Real space image of the highest occupied molecular orbital (HOMO) of pentacene resulting from a DFT simulation. b) A Fourier transformation of the pentacene orbitals. The red hemisphere is a surface of constant binding energy and indicates, where the picture of the momentum map is taken. c) This momentum map is a hemispherical cut through the orbitals in the previous picture. These figures were taken from Daniel Lüftner's PhD thesis [25].

The method described here runs into a problem, when applied to larger systems, because in an actual ARPES experiment only the surface of a material is probed. Such probing depths are in the order of 5-10 Å in the ultraviolet regime [29, 30]. Up to this point, this is not accounted for in our theoretical description. This experimental fact, that photoemission is a surface process, stems on the one hand from the finite penetration depth of the incoming photon beam, which is in the order of 1000 Å. On the other hand, and most importantly, the outgoing electrons also have a limited mean free path, which comes from electron-electron and electron-phonon interactions and is in the order of only 5 Å [31]. The former effect is neglected, since the photon's mean free path is much larger than the electron's mean free path. To account for the latter effect, the plane wave final state is damped by an exponential function, which is specified by the two parameters z_0 and γ . The height of the plane, at which the damping begins, is z_0 and the damping strength is γ , as illustrated in Fig. 4. The damped wave function is then given by

$$|\psi_f\rangle_d = e^{i\mathbf{k}\mathbf{r}} e^{\gamma(z-z_0)} \quad (36)$$

On a side note, the inelastic mean free path (IMFP) $\frac{1}{\gamma}$ can be described by a universal curve. Such curves can be seen in Fig. 5 for an electron in metals.

The parameters z_0 and γ are here only roughly estimated. An empirically justified value would be around $\gamma = 0.5 \text{ \AA}^{-1}$, which would corresponds to a mean free path of $\frac{1}{\gamma} = 2 \text{ \AA}$. A reasonable

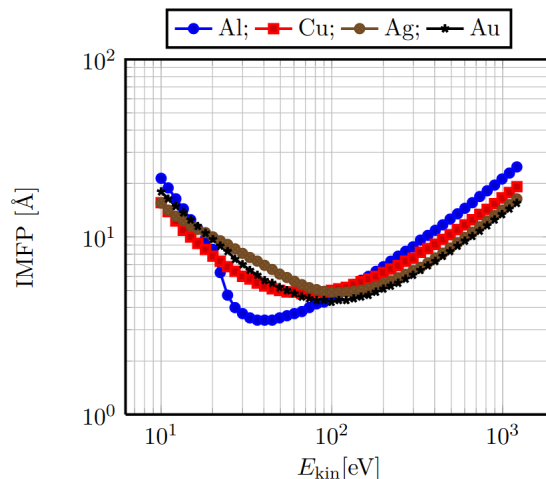


Figure 5: Universal curve of the inelastic mean free path for the materials Al, Cu, Ag and Au. The data for the curve comes from [33]. The figure is taken from [34].

setting for z_0 would be to set it centrally between the AGNR and the topmost gold layer. In the resulting ARPES momentum maps, which are shown in Sec. 4, one can see that this choice for z_0 and γ damps the contribution from the gold quite strongly, since barely any gold features are visible. This setting will thus be termed "strong damping" in the following. In order to see more gold features, a second setting is employed, in which $\gamma = 0.1 \text{ \AA}^{-1}$ and z_0 is at the topmost gold layer. This setting will be referred to as "weak damping" in the following. A convenient side effect of this formalism is that one can filter out the contribution of the AGNR by setting strong damping. This can be seen very clearly, when comparing the freestanding AGNR and the AGNR on gold including strong and weak damping with each other. In this way, one can learn about the role, that the gold plays on the ARPES pictures and better understand the experimental results.

It should be noted, that the values for z_0 and γ are empirical and thus in a way oppose the ab initio spirit of this work. However this is acceptable, because tuning the damping parameters mainly just affects the ratio between the contribution of the AGNR and the gold. It should be kept in mind, when analyzing the resulting ARPES simulations, that the strength of the gold's contribution is adjusted by the damping parameters.

3 Implementation and Computational Details

In this section the computational details as well as the working steps of the DFT simulations will be explained. The software, which was used in this work, is partially described in Secs. 2.2 and 2.3. It includes VASP [13, 18], the Atomic Simulation Environment (ASE) [35], an ARPES simulation program developed by Peter Puschnig and extended by Daniel Lüftner [32] and code for post-processing a VASP calculation, which was developed by Peter Puschnig and his group.

The settings used for all simulations can be seen compactly by looking at an INCAR-File, which is one of the input files that are handed over to VASP:

```
# INCAR created by Atomic Simulation Environment
SIGMA = 0.200000
EDIFF = 1.00e-06
SYMPREC = 1.00e-04
ALGO = Fast
GGA = PE
PREC = Accurate
ISMEAR = 1
IVDW = 11
LORBIT = 11
```

The energy cutoff is determined by `PREC = Accurate`. This setting means that the largest `ENMAX` value is taken from the `POTCAR` file. `ENMAX` amounts to `ENCUT = 400 eV` for carbon, `ENCUT = 250 eV` for hydrogen and `ENCUT = 230 eV` for gold. Therefore this setting is equal to setting **ENCUT = 400 eV**, which is the value of choice for all calculations, except the convergence tests in Sec. 3.3. The formula for the energy cutoff is given in Eq. 24. Furthermore the following settings were made:

- By setting `ISMEAR = 1`, Methfessel-Paxton smearing of order 1 is used [36]. The width of the smearing is set to `SIGMA = 0.2`.
- The convergence criterion was defined to be `EDIFF = 1.00e-06`. As mentioned in the introduction, the Kohn-Sham Eqs. 17, 18 and 19 need to be solved self-consistently. This self consistency loop is stopped, once the change in total energy between two steps is smaller than `EDIFF`.
- `ALGO = Fast` selects a mixture of the Davidson and RMM-DIIS algorithms, which are used to solve the Kohn-Sham Eqs. 17, 18 and 19. The former is used for the initial phase, then VASP switches to the latter one.
- `GGA = PE` sets the Perdew-Burke-Ernzerhof exchange-correlation functional [23].
- `IVDW = 11` activates the zero damping DFT-D3 method of Grimme, as described in Sec. 2.2.
- The chosen `LORBIT` tag tells VASP to write the `DOSCAR` and `PROCAR` file, which is necessary to calculate the projected density of states (pDOS).

In order to obtain the equilibrium positions of the atoms, one starts with an initial guess of the geometry and then performs a so-called relaxation of the structure. For each step of this relaxation the Kohn-Sham Eqs. 17, 18 and 19 are solved self-consistently. Then the positions of the ions are updated (by Eq. 37 in our case), thereby trying to minimize either the total energy or the forces on the atoms. This relaxation of the ionic positions is needed, because we applied the Born-Oppenheimer approximation, according to which the motion of the electrons and nuclei can be treated separately. So far only the electronic problem in Eq. 2 has been considered. In order to approximately solve Eq. 1, which is the Hamiltonian prior to the Born-Oppenheimer approximation, we also need to take the ionic motions into account. The settings for the relaxation were chosen to be:

```
POTIM = 0.150000
SMASS = 0.400000
EDIFFG = -1.00e-02
IBRION = 3
```

IBRION = 3 enables ionic relaxation via damped molecular dynamics. The following damped second order equation of motion is used for the update of the ionic degrees of freedom:

$$\ddot{\mathbf{x}} = -2\alpha\mathbf{F} - \mu\dot{\mathbf{x}} \quad (37)$$

where POTIM sets the scaling constant for the step width α and SMASS sets the damping factor μ . This EDIFFG setting brings the relaxation to a stop, when all forces are smaller than $0.01 \text{ eV } \text{\AA}^{-1}$.

The adsorption of an AGNR on a gold surface, as further described in Sec. 3.2, results in a net dipole moment in the direction perpendicular to the slab. This would be conflicting with the periodic boundary conditions. To counteract this problem, VASP gives the option of switching on an artificial dipole layer in the spirit of Neugebauer and Scheffler [37]. This dipole layer compensates the system’s dipole moment. It has the advantage that leading errors in the forces are corrected and the work-function can be calculated for asymmetric slabs, as was done in Sec. 4.6.2. A disadvantage is that convergence can slow down considerably, thus the VASP team recommends to pre-relax the structure without the dipole layer first. This was done and then for the relaxation with the dipole layer the following parameters were added to the INCAR file:

```
IDIPOL = 3
LDIPOL = .TRUE.
LVHAR = .TRUE.
```

IDIPOL = 3 switches on monopole/dipole and quadrupole corrections to the total energy in the direction perpendicular to the surface of the slab. LDIPOL activates the aforementioned dipole layer. By setting LVHAR = .TRUE. the total local potential, which is saved in the LOCPOT file, contains the electrostatic contributions only (ionic + Hartree), which will be used for later analysis in Sec. 4.6.2.

After the structure is relaxed, DFT simulations without ionic updates are performed with a denser k-mesh. These are necessary so that the quantities of interest are converged with respect to the k-mesh.

3.1 Initialisation and Relaxation of the freestanding AGNR

An initial geometry of the AGNR was created using ASE with a bond length of 1.42 \AA between each carbon atom. It was relaxed with the settings described in Sec. 3. Here, a dipole layer is not necessary, because the AGNR has no net dipole moment due to its mirror symmetry around the x-, y- and z-axis. In addition to the above-mentioned settings, the tag ISIF = 3 was set to relax the unit cell shape and volume together with the atomic positions. With such a setting, however, the thickness of the vacuum slab will gradually decrease during the relaxation. Therefore, starting with a relatively large vacuum of 15 \AA , 100 relaxation steps with ISIF = 3 were performed. After that a relaxation with fixed unit cell was performed.

The SYMPREC tag determines how accurate the positions of the atoms must be specified. By increasing it from $1.00\text{e-}5$ to SYMPREC = $1.00\text{e-}04$, VASP can detect the D_{2h} symmetry of the system easier.

3.2 Adsorption of AGNR on Au(111)

In Fig. 6 an overview of the 7-AGNR on Au(111) system can be seen. In this section the steps of how this structure is created will be explained.

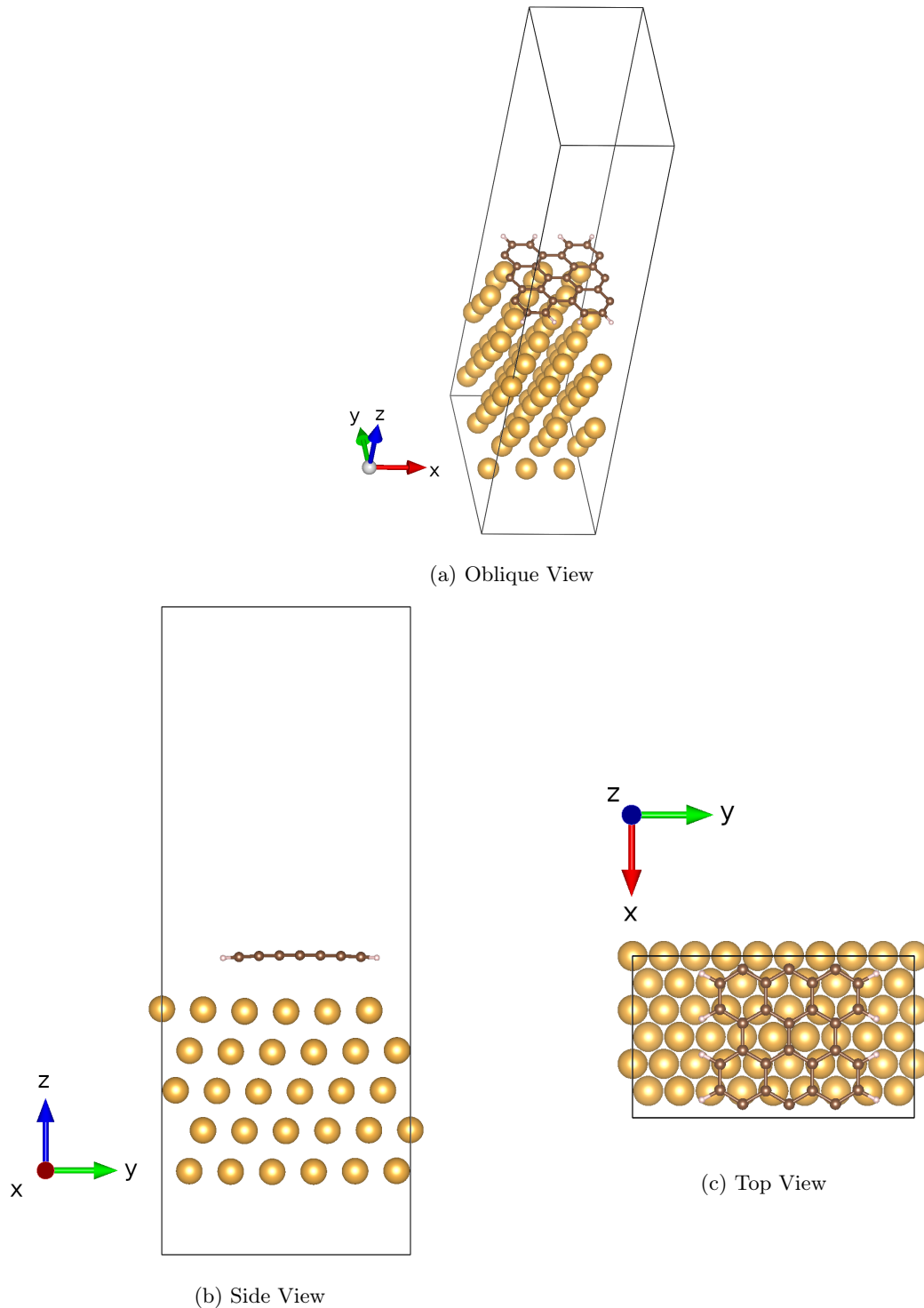


Figure 6: Overview of 7-AGNR on five layers of a Au(111) surface. The red, green and blue arrows of the coordinate system denote the x-, y- and z-direction respectively.

First a Au(111) surface with an orthogonal unit cell is created. This can be easily done with ASE in Python:

```
from ase.build import fcc111
```

```
gold = fcc111('Au', (1,2,5), orthogonal=True, periodic=True)
```

This yields a unit cell with two gold atoms per layer and a default experimental lattice constant $a = 4.08 \text{ \AA}$, that the ASE authors took from a book by Ashcroft and Mermin [38]. For all calculations, with the exception of the convergence tests discussed in Sec. 3.3, five layers of gold were used. Before combining the AGNR with the gold, a relaxation was performed for each of them separately.

When a DFT simulation of an AGNR on Au(111) should be performed, one of the materials has to be stretched or compressed, so that both systems can be brought together into one unit cell. This is necessary, because due to the periodic boundary conditions, a common repeat unit for the AGNR and the Au(111) surface slab has to be found. Such a system is then called a commensurate structure. Since the nanoribbon is a 1-dimensional system, its unit cell has to be aligned with that of the gold only in one direction, the x-direction in this case. It just so happens that, if the unit cell of the nanoribbon is multiplied by 2 in the x-direction and the unit cell of the gold is multiplied by 3 in the x-direction, they both align with about 0.7% difference. Here, the experimental lattice parameter was used for gold and for the AGNR the lattice parameter was optimized via DFT calculations, as described in the previous section. In order to reach alignment of both unit cells, the positions of the gold atoms were multiplied by 0.99313, thereby compressing it by about 0.7% in all directions.

Next, the y-direction is considered. In Fig. 6 one can see that it is parallel to the surface of the slab and nanoribbon. The question of how many times the unit cell of the gold should be multiplied in that direction is a trade-off between accuracy and computational speed. On the one hand one would like much space between the nanoribbons, so they do not interfere with each other in the simulation. On the other hand by increasing the number of atoms in the unit cell N , the computation time scales like N^3 . For 7-AGNR on gold, it was decided to multiply the unit cell of the gold by 6 in the y-direction, leaving 5.7 \AA between the hydrogen atoms of each nanoribbon in that direction. For 9-AGNR this value is 8.26 \AA , and for 13-AGNR it is 8.33 \AA , multiplying the gold unit cell by 8 and 10 respectively.

Summing everything up and looking at 7-AGNR as an example, the nanoribbon's primitive cell is multiplied by (2,1,1) and that of gold by (3, 6, 5). This amounts to 126 atoms in the unit cell for 7-AGNR on gold. Applying an analogous procedure, for 9-AGNR there are 164 atoms in the unit cell and for 13-AGNR there are 210. The increase in computation time relative to 7-AGNR can be roughly estimated to be $(\frac{164}{126})^3 = 2.2$ for 9-AGNR and $(\frac{210}{126})^3 = 4.6$ for 13-AGNR.

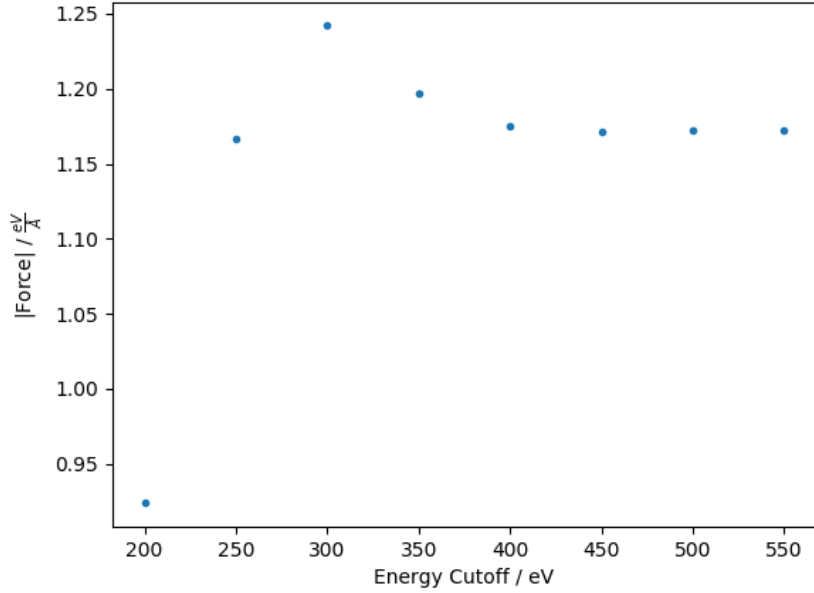
3.3 Convergence

We have also performed a convergence test with respect to the energy cutoff and the k-mesh for each differently sized nanoribbon (7-AGNR, 9-AGNR and 13-AGNR) on Au(111). Four different adsorption positions of each AGNR are investigated, as will be described in Sec. 4.2. Only the one with the lowest energy, which is the "bond hollow" adsorption site, is used for the convergence test. The results of the convergence tests can be seen in Fig. 7a for the energy cutoff and in Fig. 7b for the k-mesh. To decrease computation time the lower two gold layers were removed, leaving the slab with three gold layers. For the convergence test of the energy cutoff a relatively small k-mesh of $5 \times 2 \times 1$ was chosen, again to save computational resources. A random carbon atom was moved in the x-direction by 0.02 \AA for the energy cutoff convergence test and by 0.01 \AA for the k-mesh convergence test. The latter displacement was chosen lower due to convergence issues of the algorithm. This does not make any difference for the test, because the relative noise is still very low.

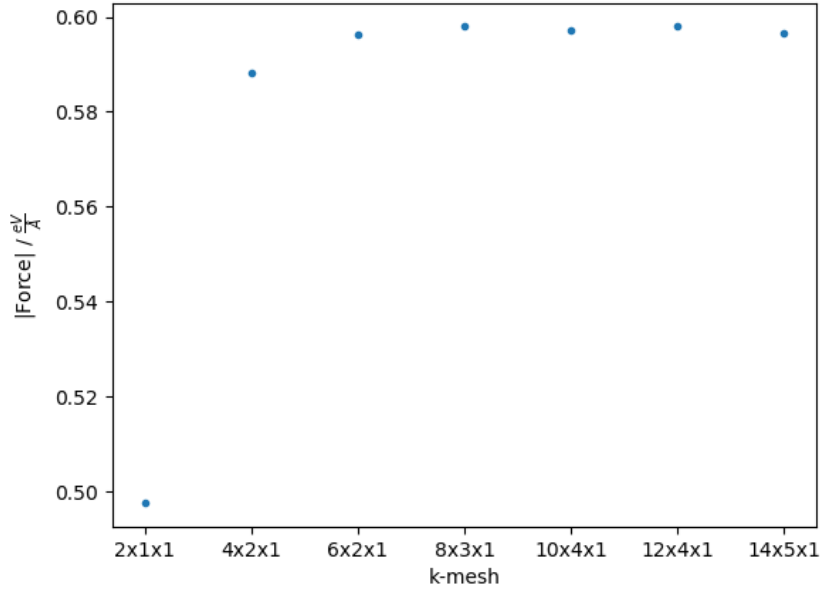
For the energy cutoff convergence test, an energy cutoff of 400 eV was regarded as a good initial guess. Values around 400 eV were selected in a 50 eV interval and a DFT simulation was performed for each of them. All components (in x-, y-, and z-direction) of the force converge in the same manner. In Figs. 7a and 7b the components of the force are not depicted, but only its norm is shown for better clarity. Evaluating the results in Fig. 7, one can see that the energy cutoff of 400 eV was indeed a good choice. This value was then used for the k-mesh convergence test.

As a starting point for the k-mesh convergence test, it was initially guessed that the k-mesh $8 \times 3 \times 1$ should be a reasonable choice. Then the values of the k-meshes were selected by taking

certain percentages of the k-mesh $8 \times 3 \times 1$ and rounding the result. Of course in the z-direction there should always be just one k-point, since the system is 2-dimensional. Taking 25%, 50%, 75%, 100%, 125%, 150% and 175% of $8 \times 3 \times 1$, results in the values on the x-axis of Fig. 7b. In this figure it can be seen that the k-mesh of $8 \times 3 \times 1$ produced converged results. This is also the case for the $6 \times 2 \times 1$ -k-mesh, which one could use in order to decrease the computation time.



(a) Convergence test for energy cutoff



(b) Convergence test for k-meshes

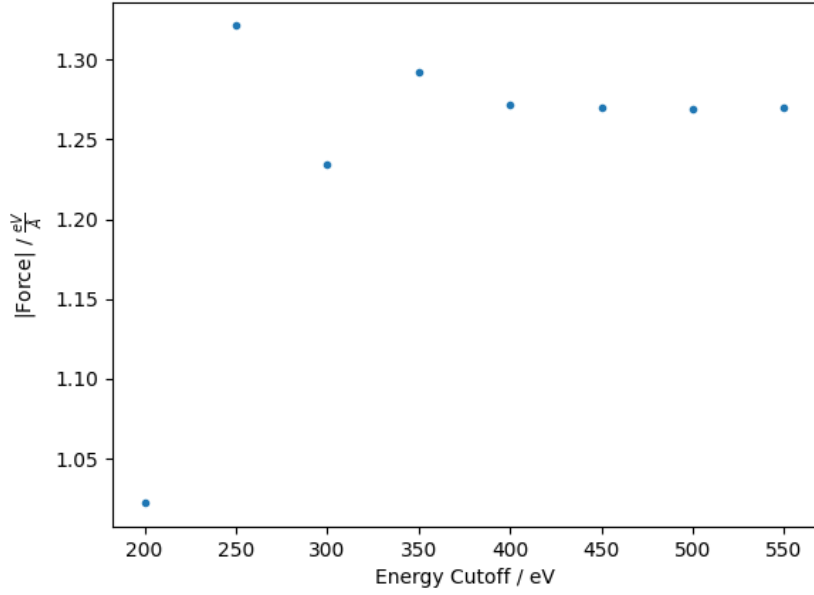
Figure 7: The relaxed 7-AGNR on gold in the "bond hollow" adsorption position was used for convergence tests. A randomly selected carbon atom was moved by 0.02 \AA in the x-direction for the energy cutoff test and by 0.01 \AA for the k-mesh test. The norm of the force on that atom is shown.

For 9-AGNR on gold, a k-mesh of $4 \times 1 \times 1$ was used for the energy cutoff convergence test.

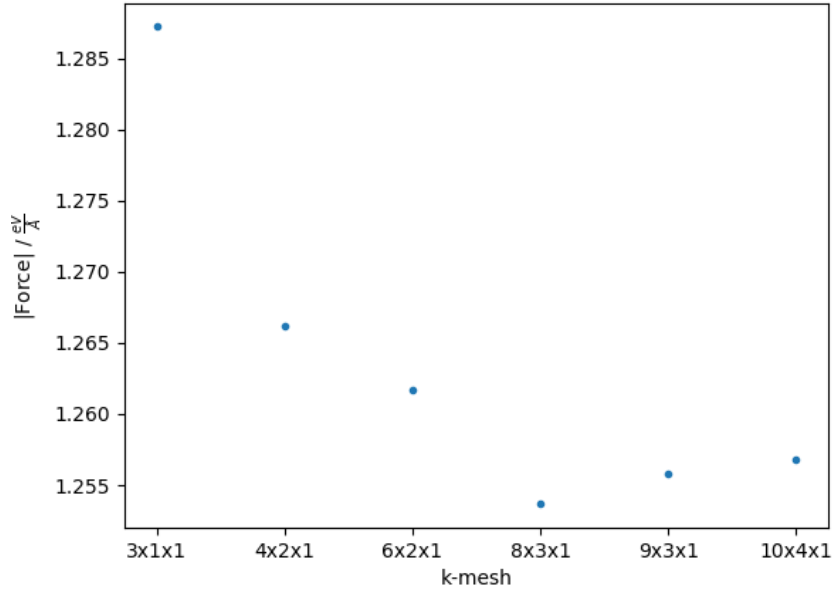
The procedure of choosing different k-meshes is the same as for 7-AGNR, except that a different initial guess was made, namely $6 \times 2 \times 1$ instead of $8 \times 3 \times 1$. For 9-AGNR the unit cell is larger in the y-direction, therefore fewer k-points are needed. Taking the percentages 50%, 75%, 100%, 125%, 150% and 175% yields the k-meshes seen in Fig. 8b. As can be seen in Fig. 8a, an energy cutoff of 400 eV is sufficient, thus this value was used for the k-mesh convergence test.

Looking at Fig. 8b, at a first glance it seems as if the calculations are not converged for a k-mesh of $6 \times 2 \times 1$, however when looking at the y-axis one sees that the values fluctuate only marginally. The difference between the norm of the force for a k-mesh of $6 \times 2 \times 1$ and $10 \times 4 \times 1$ is only about 0.4 %, therefore a k-mesh of $6 \times 2 \times 1$ can be regarded as converged.

Prior to the convergence tests the systems were relaxed. For the relaxation of 9-AGNR on gold a k-mesh of $6 \times 1 \times 1$ was used for some adsorption positions, while for others it was reduced to $3 \times 1 \times 1$ in order to save computational resources. This difference in k-meshes is not relevant, as long as both produce reasonably well converged results. For a k-mesh of $3 \times 1 \times 1$ one can see in Fig. 8b that this is barely the case, however when performing a relaxation it is fine, as long as a DFT simulation with a denser k-mesh is performed afterwards, when one wants to compute the properties of the material. This was done, and in particular, when comparing the energies in Fig. 13 the same k-mesh, namely $6 \times 2 \times 1$, was used for all adsorption sites.



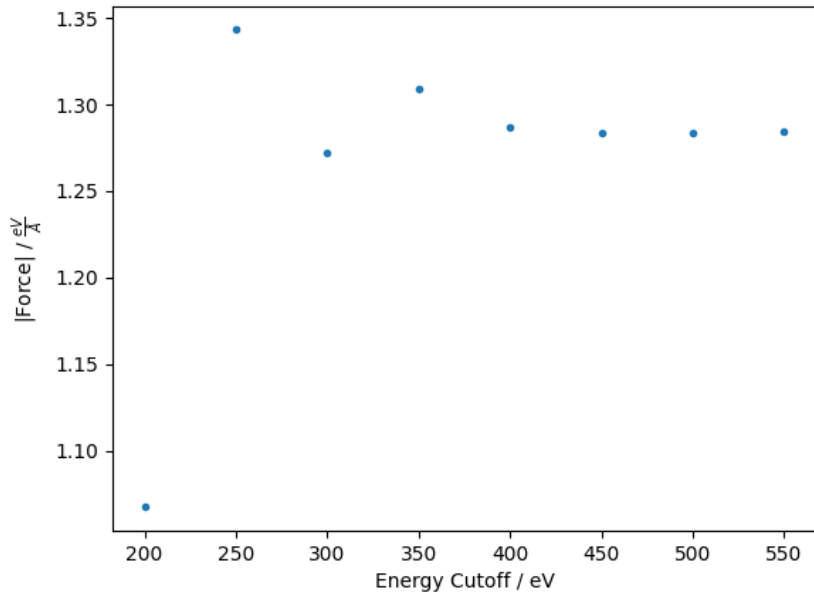
(a) Convergence test for energy cutoff



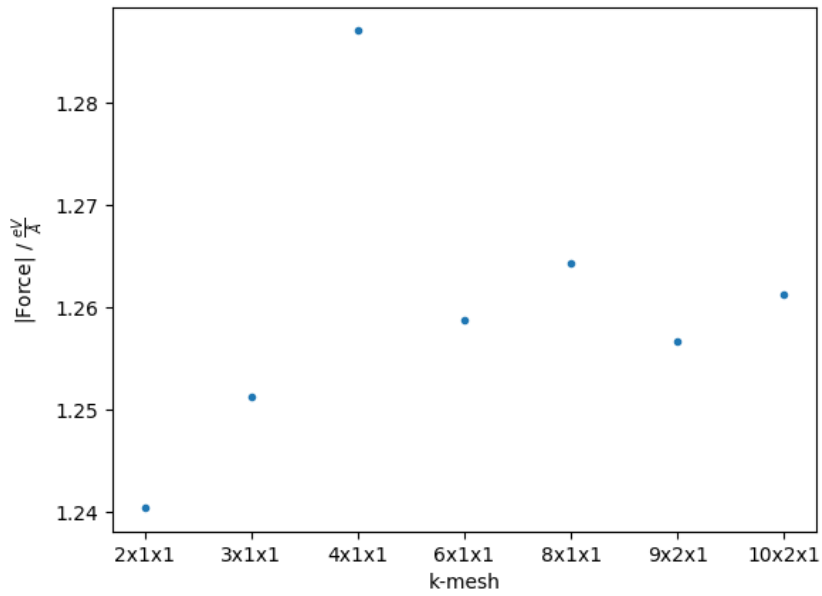
(b) Convergence test for k-meshes

Figure 8: The relaxed 9-AGNR on the "bond hollow" adsorption site was used for these convergence tests. The norm of the force on a random carbon atom, that was moved by 0.02 \AA in the x-direction, is depicted.

Analog calculations to the ones above are made for 13-AGNR. Here a k-mesh of $6 \times 1 \times 1$ was deemed as a reasonable initial guess. From this the percentages 25%, 50%, 75%, 100%, 125%, 150% and 175% were taken, resulting in the k-meshes seen in Fig. 9b. As above, the energy cutoff of 400 eV is shown to be appropriate. The difference between the force for $6 \times 1 \times 1$ and $10 \times 2 \times 1$ is about 0.2 %, thus a k-mesh of $6 \times 1 \times 1$ is deemed converged.



(a) Convergence test for energy cutoff



(b) Convergence test for k-meshes

Figure 9: Analog to the AGNRs above, the 13-AGNR on the "bond hollow" adsorption site was used for convergence tests. The norm of the force on a carbon atom, that was moved by 0.02 \AA in the x-direction, is depicted.

4 Results

In this section the results of the simulations are presented and compared with the literature, when appropriate. Instead of labeling the axis with x , y and z , as was done in the previous sections, the notation is here adapted to make it more intuitive. Namely, the component of the wave vector, that is parallel to the AGNR, is denoted by k_{\parallel} and its component perpendicular to it is denoted by k_{\perp} . This corresponds to the x - and y -direction respectively in Fig. 6. A new label of the z -direction is not needed in this section, since the component of the wave vector perpendicular to the surface of the sample is in general not conserved in an ARPES experiment, and thus no simulation of it was performed. The orientation of Figs. 10, 11 and 12 is consistent with the momentum maps, like e.g. Fig. 30, in the sense that the direction perpendicular to the AGNR is on the horizontal axis and the direction parallel to the AGNR in on the vertical axis for all figures.

4.1 Choice for Starting Geometry and Thickness of Vacuum Slab

Since the choice of the starting conditions affects the number of steps for the ionic relaxation and hence the computation time of a DFT simulation, it is important to start from an educated guess. The 7-AGNR was initially placed 3 Å above the gold substrate. Through relaxation it moved up to about 3.26 Å, confirming that these starting conditions are indeed reasonable. The 9-AGNR and 13-AGNR were placed 3.4 Å above the gold and relaxed to the values seen in Fig. 14.

The thickness of the vacuum slab used in this work ranges between 20 and 23 Å. These variations are not expected to affect the results, as long as the vacuum is large enough so that the slabs do not interact with each other in the direction perpendicular to their surface, which is the z -direction in this case. The chosen values fulfill this criterion, since the wave functions of the atoms decrease exponentially and the charge density is almost zero for a long distance, as can be seen in Sec. 4.6.2. When comparing systems with each other, of course the same vacuum is used. The reason, why the vacuum is sometimes varied, is that there was a numerical problem involving the relaxation with the dipole layer, which led to the calculation not converging. It was found that this problem is mitigated by increasing the vacuum and moving the system (almost) to the bottom of the unit cell, instead of placing it in the middle of the unit cell.

4.2 Adsorption Sites of 7-, 9- and 13-AGNR on Au(111)

To the best of the author's knowledge it is not yet clear which adsorption sites AGNRs prefer on a Au(111) surface. Due to the alignment of the AGNRs along the Au(788) terraces, their orientation is given in the case at hand. The remaining problem of finding the adsorption position on the Au(111) with given orientation is, however, still non-trivial. One possibility to determine this adsorption site would be to define a 2-dimensional grid and make a DFT simulation for each of the grid points. The energies of the systems on each grid point would then give an energy landscape, where the point with the lowest energy would approximately correspond to the actual adsorption position. However this procedure was adjudged to consume too many computational resources. Rather it was decided to look at just a couple of adsorption positions, defined in Fig. 10 for 7-AGNR, and compare their energies and adsorption heights.

4.2.1 7-AGNR on Au(111)

For 7-AGNR on Au(111) these positions are characterized on the one hand by the positioning of as many carbon atoms in the top, hollow and bridge position as possible and, on the other hand, by the location of the bonds between the carbon atoms on these three positions. Coincidentally the "atom bridge" position is identical with the "atom top" position. Analogously the "bond bridge" position is the same as the "bond top" position. Therefore only four of the six positions are distinguishable from each other.

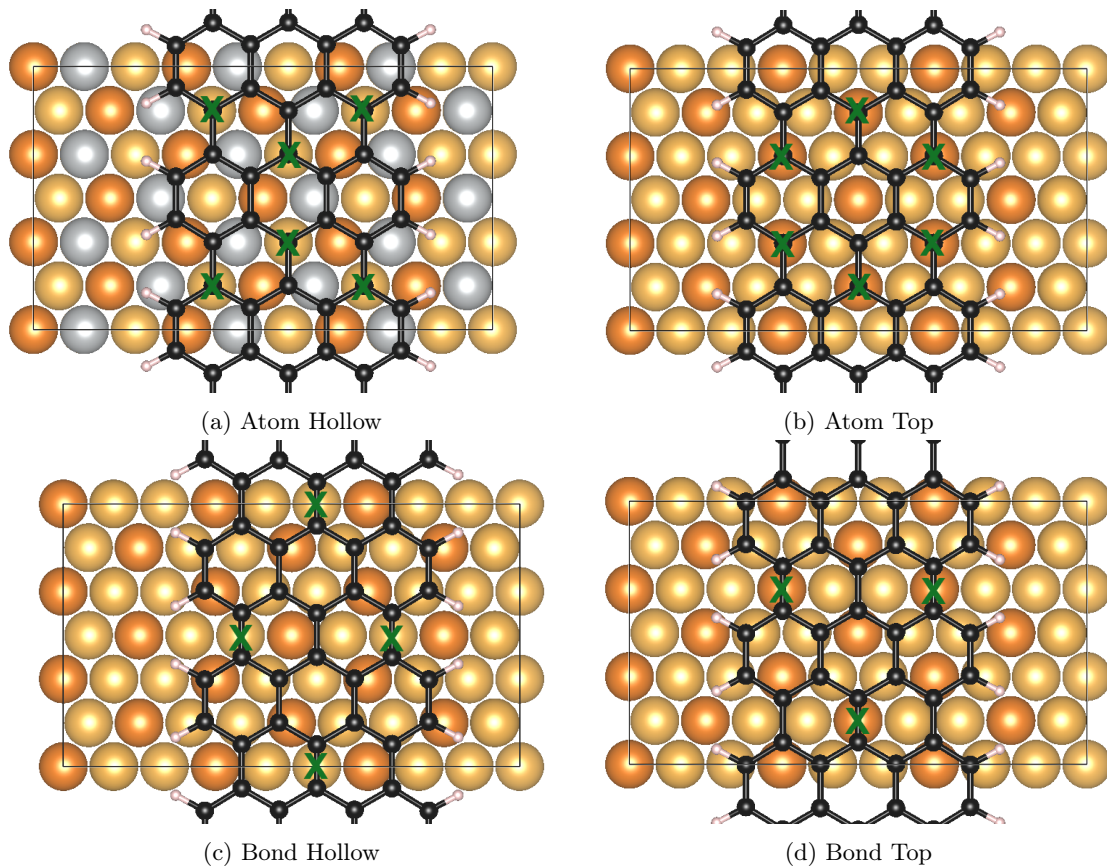


Figure 10: Top view of the four adsorption sites 10a "atom hollow", 10b "atom top", 10c "bond hollow" and 10d "bond top" of 7-AGNR on Au(111). The topmost gold layer was colored dark orange, while the lower ones are golden yellow. In Fig. 10a the second layer from the top was colored silver, while for all other pictures it was refrained from doing so, to increase clarity. The green crosses help to understand the nomenclature, e.g. they mark the atoms in the hollow position in Fig. 10a. The axis are the same as in Fig. 6c.

Note that the systems in Figs. 10a, 10b and 10c have a mirror symmetry about the horizontal axis, that is in the middle of the unit cell. The "bond top" configuration (Fig. 10d) does not have this symmetry. Note that this definition of positions is not unique. For example there is another possibility of defining the "atom hollow" position, which has the same number of carbon atoms in the hollow position.

4.2.2 9-AGNR on Au(111)

Adsorption positions of 9-AGNR on Au(111) are defined in analogy to the ones for 7-AGNR.

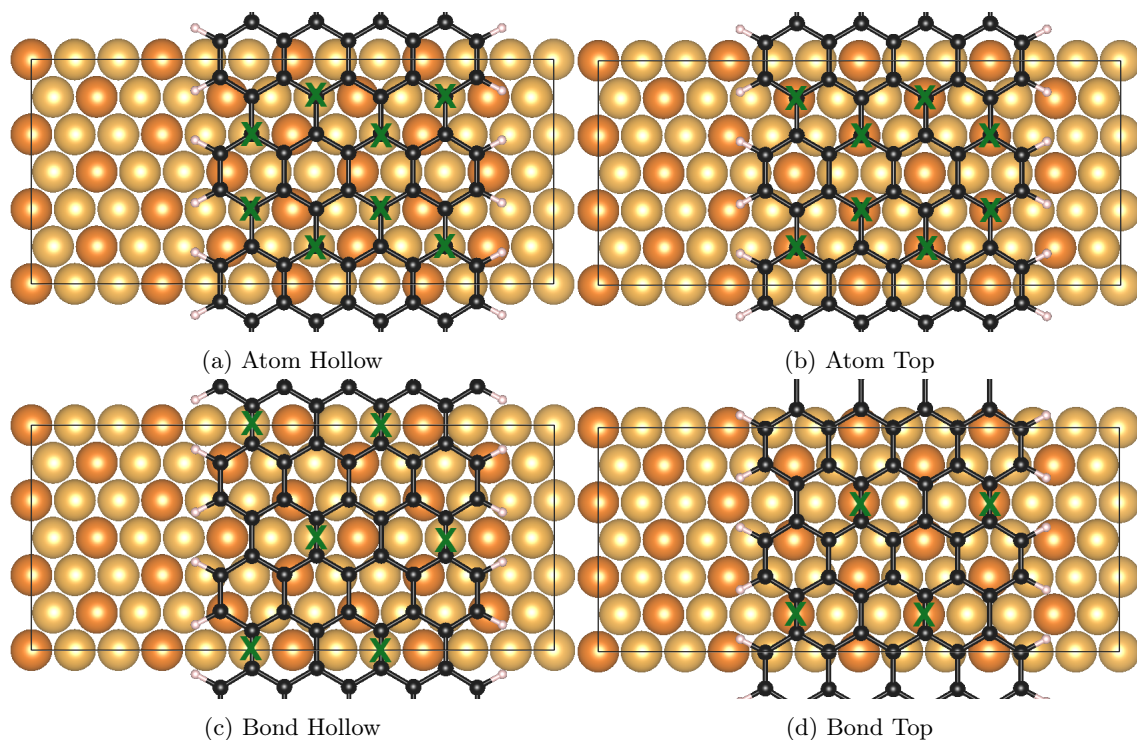


Figure 11: Adsorption sites for 9-AGNR are defined in analogy to the ones for 7-AGNR (Fig. 10). The topmost gold layer was colored dark orange, while the lower four are golden yellow.

4.2.3 13-AGNR on Au(111)

Continuing in the same manner, adsorption positions for 13-AGNR are defined in Fig. 12.

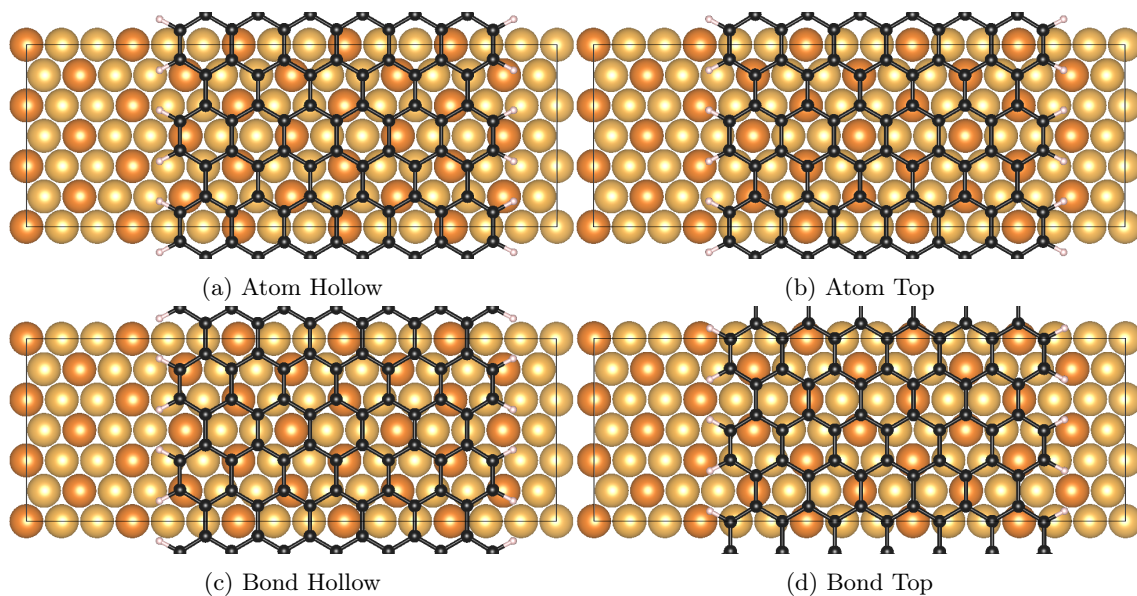


Figure 12: Adsorption sites for 13-AGNR are defined in analogy to the ones for 7-AGNR and 9-AGNR. The topmost gold layer was colored dark orange, while the lower four are golden yellow.

4.2.4 Comparison of Energies and Adsorption Heights

DFT simulations of all configurations in Figs. 10, 11 and 12 were performed. In this section it will be explained how the energies and adsorption heights are obtained and the results will be discussed.

First, we focus on a comparison of the total energies of the relaxed structure, where in Fig. 13, we present total energy differences to the most favorable configuration for each ribbon. Note that those values are based on total energies extrapolated to zero smearing is depicted, denoted by VASP as $energy(\sigma \rightarrow 0)$. Due to the usage of a smearing parameter σ , the total energy is only correct in the limit $\sigma \rightarrow 0$. On a side note, taking the free energy yields the same results here. The difference between the energies of different adsorption positions, which is the quantity of interest, would be the same, i.e. Fig. 13 would look the same, but the normalization values would be slightly different. The used k-mesh was $8 \times 5 \times 3$ for 7-AGNR, $6 \times 2 \times 1$ for 9-AGNR and $6 \times 1 \times 1$ for 13-AGNR.

Inspecting Fig. 13, two types of comparisons can be made: firstly, the comparison of different adsorption positions ("atom top", "atom hollow" etc.) for each differently sized nanoribbon individually. Secondly, the overall picture for 7-AGNR can be compared to that of 9-AGNR and 13-AGNR. By focusing on just one nanoribbon in Fig. 13, e.g. 7-AGNR, one can see that the largest difference is the one between the "bond top" and "bond hollow" position and it amounts to 48 meV. Taking into account the thermal energy at room temperature, the system has an energy of $\frac{1}{2}k_B T_{room} = 12.5 \text{ meV}$ per degree of freedom, concluding that the energy differences are small, but not negligible with respect to the following consideration: The adsorption positions that were considered here are only a local minimum in the energy landscape. If one wants to properly determine, whether the AGNRs shift between any of these positions due to thermal fluctuations, one would need to determine the energy barriers between said local minima. There could be just a low energy barrier, in which case the AGNRs would shift from the bond top position to the bond hollow (or some other low energy position) by thermal fluctuations. These energy barriers also determine whether the AGNRs stay in their minimum energy position, or diffuse to other low energy positions.

Moving on to the second type of comparison, which is the one where the differently sized AGNRs are compared with each other, one can see that Fig. 13 looks very similar for 7-AGNR, 9-AGNR and 13-AGNR. The reason for this is that their positions are defined in a analogous fashion in Figs. 10, 11 and 12. However in these definitions there are inherently some differences due to the non-commensurability of the structure, leading to the differences in energies.

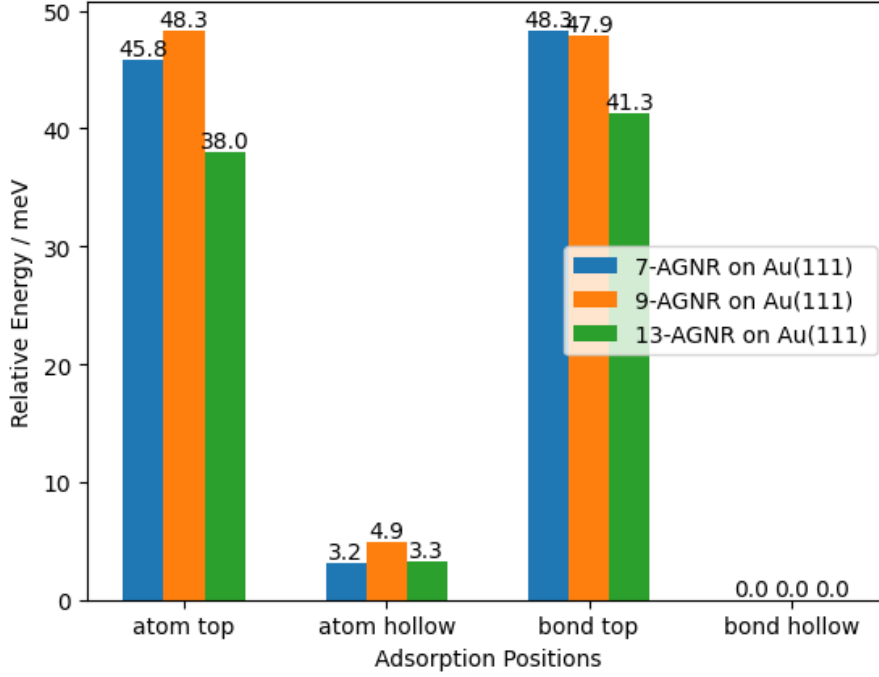


Figure 13: The total energy for different adsorption positions and AGNRs of different sizes are depicted. The relative energy is normalized to be zero for the "bond hollow" position, for which we find total energies of -615.0474 eV, -798.4238 eV and -1057.0719 eV for 7-, 9- and 13-AGNR respectively. The energies are given per unit cell, therefore they are of course larger for the larger unit cells.

The adsorption energy E_{ad} of the AGNRs on Au(111) can be calculated via

$$E_{ad} = E_{AGNR+Au(111)} - (E_{AGNR} + E_{Au(111)}) \quad (38)$$

where $E_{AGNR+Au(111)}$ is the total energy of the AGNR on Au(111), E_{AGNR} is the total energy of the freestanding AGNR and $E_{Au(111)}$ is the total energy of the Au(111) surface. E_{ad} is -2.741 eV, -3.139 eV and -4.615 eV in the "bond hollow" position for the 7-, 9- and 13-AGNR respectively. The E_{ad} of the other positions can be calculated by adding these values to the ones in Fig. 13.

Secondly, we analyze the adsorption heights. They are calculated by taking the average of the z-coordinate of the topmost gold layer and the nanoribbon (including hydrogen atoms) respectively, and then subtracting this height of the gold layer from that of the nanoribbon.

Inspecting Fig. 14, one can see a clear trend regarding the width of the ribbon: the wider the ribbon, the larger the adsorption height. The maximum difference in adsorption heights for 7-AGNR is between the "atom top" and "bond top" position and amounts to 0.007 Å, which is probably negligibly small. In contrast to the situation for the energies, the adsorption heights look more dissimilar for differently sized nanoribbons. While the heights of 9-AGNR and 13-AGNR look somewhat similar, the "bond top" position for 7-AGNR is an outlier in that regard. For 9-AGNR and 13-AGNR it looks like the adsorption heights correlate with the energy. However this has to be taken with caution, since the differences in adsorption heights are very small, therefore they are susceptible to noise of any kind.

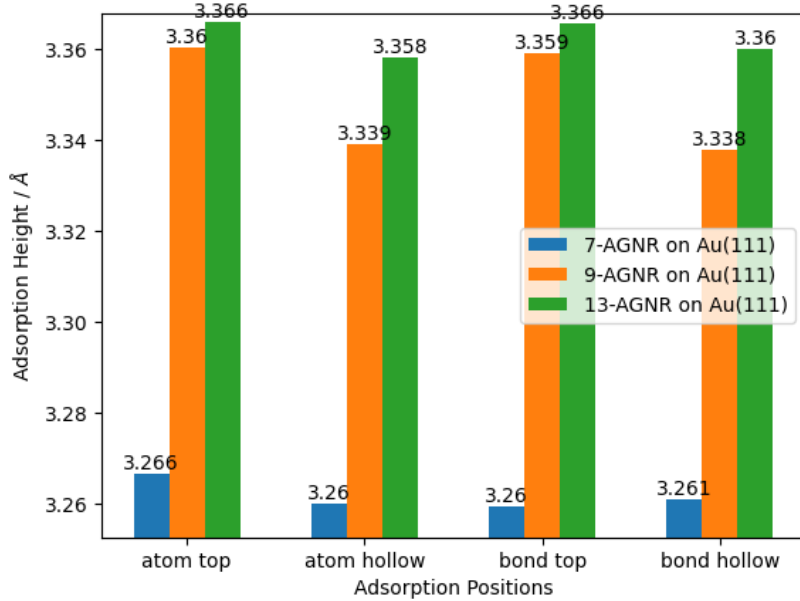


Figure 14: The adsorption heights for different adsorption positions and AGNRs of different sizes are depicted. Note that these values are very close together, therefore noise due to the uncertainty of the calculation is relatively high compared to these values.

Weiß et al. measured the adsorption height of 7-AGNR on Au(111) to be $2.59 \pm 0.05 \text{ \AA}$ for the carbon atoms at the edge of the AGNR and $3.20 \pm 0.03 \text{ \AA}$ for the carbon atoms in the middle [39]. Taking the average over all carbon atoms, this amounts to $3.03 \pm 0.04 \text{ \AA}$. The corresponding value in this work is calculated to be 3.29 \AA . It is the average adsorption height of the carbon atoms in the "bond hollow" adsorption position of 7-AGNR on Au(111). At this point, it should be noted that the adsorption heights in Fig. 14 are calculated for fully hydrogenated AGNRs. A comparison between simulation and experiment is presented in Table 1. There, one can see that the bending of the 7-AGNR is significantly stronger in the experiment, than it is in the simulation. Weiß et al. recognize that the 0.7 \AA difference between edge carbon atoms and the carbon backbone is "a massive distortion". They say, it "suggests substantial edge dehydrogenation, which at our annealing temperatures is indeed expected, followed by the formation of local covalent bonds between the C2 atoms [carbon atoms at the edge] and the Au(111) substrate." [39] Such a dehydrogenation is not considered in my simulation, explaining the different adsorption heights of the edge atoms. The low height of the edge atoms in the experiment of course lowers the average adsorption height. This explains the 0.3 \AA difference of the average height between experiment and simulation. The adsorption heights of the carbon atoms in the middle agree well, with only a 0.1 \AA difference between simulation and experiment. Additionally to the AGNR, Weiß et al. investigated (3,1)-GNR/Cu(111), which shows a bending of 0.14 \AA without dehydration. They give an explanation of this bending (Fig. 5 [39]), that may be applied to our case of simulated 7-AGNR/Au(111).

Table 1: The adsorption heights of 7-AGNR on Au(111), that were calculated in this work, are compared to experimental adsorption heights [39]. The simulated adsorption heights are those of the "bond hollow" adsorption site. The units are \AA .

	Simulation	Experiment [39]
Carbon atoms in the middle	3.31	3.20 ± 0.03
Carbon atoms at the edge	3.23	2.59 ± 0.05
Average over all carbon atoms	3.29	3.03 ± 0.04

To end this section, it will be discussed, what role the vdW-correction plays on the adsorption height. Klein et al. investigated the adsorption height of azulene and naphthalene on Ag(111) and Cu(111), calculated using DFT combined with different vdW methods [40]. They applied the following methods:

- **PBE-D3**, which was also applied in this work [12]. In contrast to this work, Klein et al. used the Becke-Johnson damping function [41]. It can be invoked by setting $IVDW = 12$ in the VASP INCAR file.
- **PBE-vdW^{surf}** "The vdW^{surf} approach [42, 43] includes the collective electronic response of the substrate in the determination of the vdW parameters (C_6 coefficients, polarizabilities and vdW radii) by combining the pairwise Tkatchenko-Scheffler (TS) method [44] with the Lifshitz-Zaremba-Kohn theory [45, 46]." [40]
- **PBE-MBD**, which stands for Many-Body Dispersion. "The MBD method [47, 48] accounts for collective many-body vdW effects beyond the pairwise approximation by representing the atomic response functions (within the random phase approximation) by a set of quantum harmonic oscillators interacting via the dipole-dipole interaction potential." [40]
- **PBE-D3^{surf}** is proposed by Klein et al. as an improvement of the DFT-D3 method. "D3^{surf} is [...] a rather simple extension of the original D3 scheme by adding C_6 coefficients for higher coordination number where none were available yet." [40]

To summarize the results of Klein et al., it can be said that all four methods produce satisfactory results. They all show a comparative average error of 0.04-0.07 Å (see Table 3 in [40]). Applied to our situation of an AGNR on Au(111), we can thus expect that the PBE-D3 method performs reasonably well.

4.3 Electronic Structure of 7-AGNR

In this section, the electronic structure of 7-AGNR will be investigated. First, the simulated band structure of freestanding 7-AGNR and the density of states (DOS) of freestanding 7-AGNR and 7-AGNR on Au(111) will be presented. Secondly, photoemission band maps of freestanding 7-AGNR as well as those of 7-AGNR on Au(111) are shown. These simulated band maps will be compared with experiments. Thirdly, momentum maps of freestanding 7-AGNR and 7-AGNR on Au(111) are presented. It is investigated, to what extent the different adsorption positions influence the momentum maps. Additionally, momentum maps are compared with the literature and with experiments, which were performed by Xiaosheng Yang and co-workers [49].

4.3.1 Band Structure and Density of States (DOS)

In the following, the band structure of freestanding 7-AGNR will be investigated. Then, the simulated density of states (DOS) of freestanding 7-AGNR and 7-AGNR on Au(111) will be presented.

Band structure calculations are typically performed in two steps. First, a self-consistent DFT calculation is performed with a k-mesh spanning the whole Brillouin zone, for example a $64 \times 8 \times 8$ k-mesh. Secondly, the electron density of this first run is taken and kept constant during a second calculation. In this calculation, an optimized $\Gamma - X$ k-mesh can be used. For example, if one wants to perform a band structure calculation along $\Gamma - X$, like in Fig. 19, a k-mesh of $128 \times 1 \times 1$ might be taken. One can check, if convergence with respect to a specific k-mesh is reached, by performing another calculation with a denser k-mesh. For example, one might perform a calculation with a $64 \times 1 \times 1$ and a $128 \times 1 \times 1$ k-mesh. If both band structures, that result from these calculations, look the same, then the band structure is converged with respect to the $64 \times 1 \times 1$ k-mesh. This procedure can be applied to all quantities that are calculated in this work. It will be applied to the DOS, band maps and momentum maps as well.

The band structure of freestanding 7-AGNR is depicted in Fig. 15. There, one can identify a band gap of 1.61 eV. Zhu et al. [50] performed a DFT simulation with local-density approximation (LDA), finding a band gap of 1.59 eV, which is similar to the result of this work. A more detailed analysis of the band gaps will be given in Sec. 4.6.1.

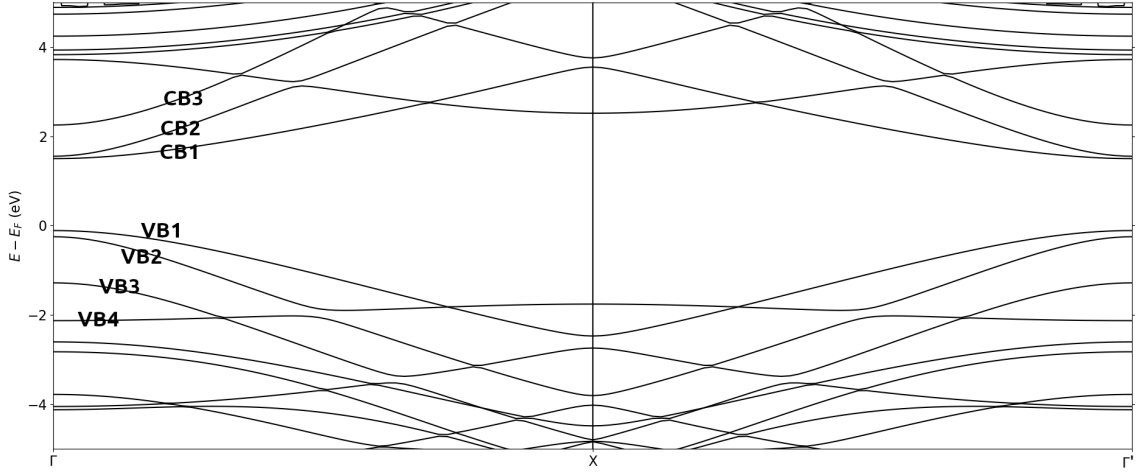


Figure 15: The band structure of freestanding 7-AGNR parallel to the ribbon is shown. 64 k-points are used in this direction. The unit cell is 4.287 \AA long this direction and the distance $\Gamma - X$ is equal to $\frac{\pi}{4.287} = 0.733 \text{ \AA}^{-1}$. The distance $\Gamma - \Gamma'$ is thus 1.466 \AA^{-1} long, where Γ' denotes the Γ -point in the second Brillouin zone. The four highest valence bands (VB) and the three lowest conduction bands (CB) are marked.

Moving on to the density of states (DOS), these are not only interesting on their own, but will be also important for the selection of momentum maps in Sec. 4.3.3.4. There, momentum maps are compared to experiment. Due to practical reasons, these are not depicted for all binding energies. Rather, only the relevant binding energies are chosen. These are identified by looking at the density of states (DOS) and choosing the binding energies, for which the AGNR has a high DOS. These peaks in the DOS correspond to binding energies, at which the momentum maps have a high photoemission intensity. Therefore it is expected that the features, that are seen in these momentum maps are brighter and can be seen easily in the experiment. In addition to the criterion of high DOS, it was also tried to choose binding energies, for which the momentum maps are somewhat representative for momentum maps at other binding energies as well. In the case of 7-AGNR on Au(111), the binding energies -0.4 eV , -1 eV and -1.8 eV were identified as binding energies of interest for a momentum map.

A comparison between the DOS of the freestanding 7-AGNR and the 7-AGNR on Au(111) is worthwhile. There is a band gap between around 0 eV and 1 eV . In the literature it is shown experimentally that the decoupling of graphene nanoribbons from a metal substrate affects their band gap [51, 7], thus some differences between the electronic structure of freestanding AGNR and AGNR on a Au(111) surface are expected.

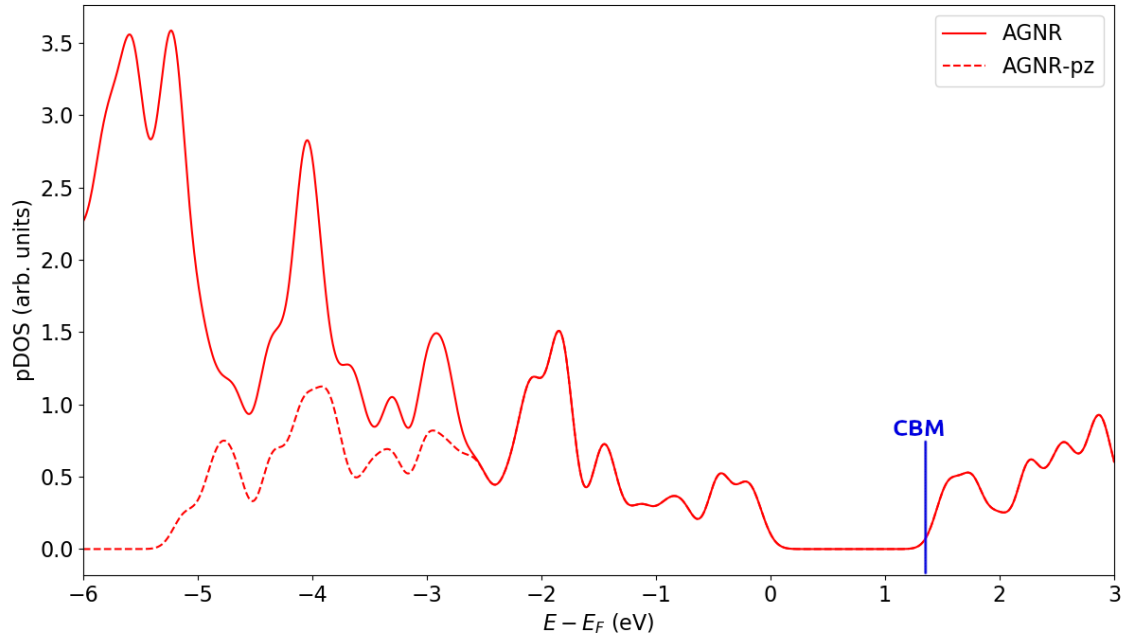


Figure 16: The DOS of the freestanding 7-AGNR is shown. It is smeared with 0.1 eV and a $64 \times 8 \times 8$ k-mesh was used. The lowest conduction band minimum (CBM) is indicated by a blue line.

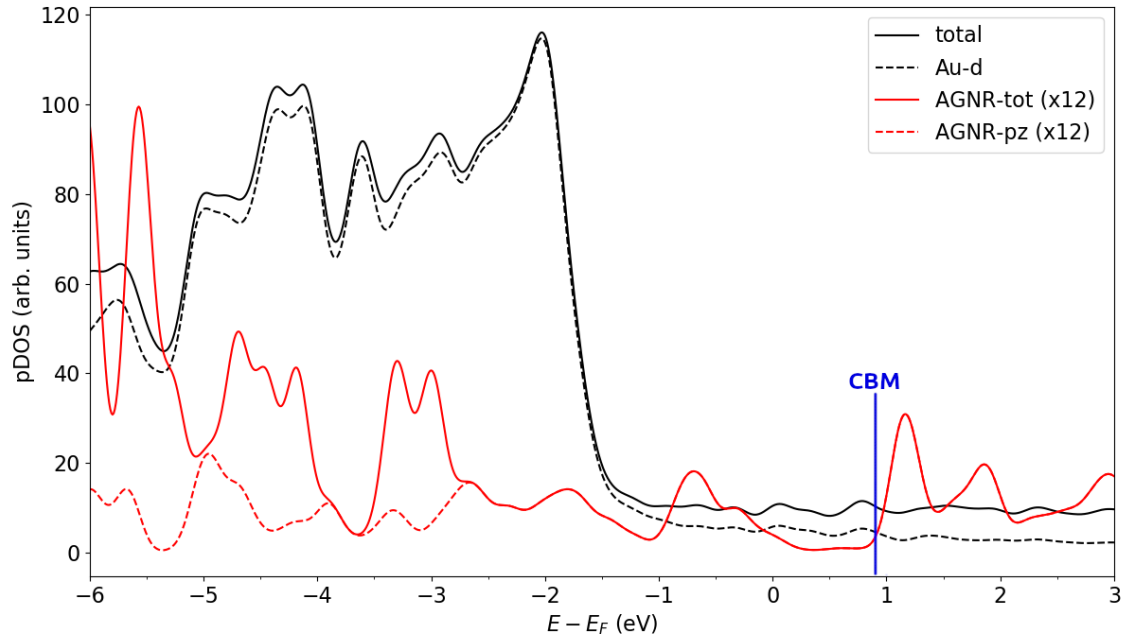


Figure 17: The DOS of 7-AGNR on Au(111) is shown. It is smeared with 0.1 eV and a $9 \times 6 \times 5$ k-mesh was used.

We adopt the convention of counting the binding energy as is shown in this DOS. This must not be confused with another common way of counting it, in which the sign is the opposite. Due to the adsorption of the AGNR on gold, the binding energies of the electrons change. So in order to align the k-maps of the freestanding AGNR with the corresponding ones on gold, the binding energy of the former was rigidly shifted to align the pictures. This way it was found that the binding energy of the freestanding 7-AGNR should be shifted by -0.4 eV. As an example, the k-map of freestanding 7-AGNR at 0.0 eV is compared to the one of 7-AGNR on gold at -0.4 eV.

This shift of -0.4eV can also be seen in the DOS, if one looks closely. For example, it can be seen by investigating the onset of the peak corresponding to the lowest conduction band minimum (CBM), which is indicated by blue lines. It is at 1.35eV in Fig. 16 and at 0.9eV in Fig. 17, corresponding to a shift of about -0.45eV .

For a later comparison with photoemission experiments, it should be kept in mind that a GGA calculation typically underestimates the total valence band width of carbon based aromatic systems. This is illustrated in Fig. 18 which compares the DOS of graphene calculated with GGA with a hybrid functional calculation (HSE), which is known to result in a valence band width in better agreement with experiments. Taking this into account, it can be expected that the simulated ARPES k-maps should be compared to the experimental ones at higher binding energies.

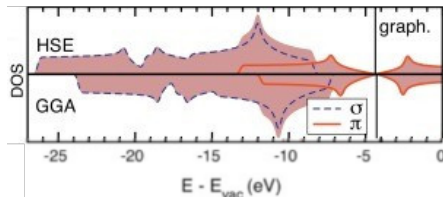


Figure 18: The DOS calculated with a GGA functional is compressed with respect to the DOS calculated with the range-separated hybrid functional HSE functional. The picture is taken from Puschnig et al. [52].

This section will be ended with a note on convergence. In Sec. 3.3 it is shown that the forces on atoms are converged with respect to the k-mesh. However this does not necessarily mean, that all physical properties are converged with respect to the k-mesh. The DOS needs a relatively dense k-mesh to fully converge. For example the DOS of 7-AGNR on gold is not fully converged for a $6 \times 3 \times 1$ k-mesh, whereas the forces on atoms are converged with that k-mesh, as was shown in Sec. 3.3. Nevertheless, it was found that the DOS of 7-AGNR on gold looks almost identical for a k-mesh of $9 \times 6 \times 5$ and $8 \times 5 \times 3$, thereby confirming that it is (almost) converged. It is not a problem to choose a high k-mesh for the freestanding 7-AGNR, since the calculation is fast. Therefore the DOS of freestanding 7-, 9- and 13-AGNR is well converged with respect to the k-mesh. However the DOS of the 7-, 9- and 13-AGNR on Au(111) should be taken with a pinch of salt, since they may not be fully converged with respect to the k-mesh.

4.3.2 Photoemission Band Maps

The term "band map" refers to a plot of the photoemission intensity $I(E_b, k_{\parallel})$ or $I(E_b, k_{\perp})$, where the two axis are the components of the wave vector k_{\parallel} or k_{\perp} and the binding energy of the electron E_b . Assuming that the ARPES simulation with its approximations is correct, it should resemble the band structure. A band map overlain by the band structure can be seen in Fig. 19. Band maps of freestanding 7-AGNR will be presented and the connection to the band structure will be highlighted. Band maps of 7-AGNR on Au(111) will be compared with experiment and the freestanding 7-AGNR.

A general aspect of band maps and momentum maps (to be presented in Secs. 4.3.3, 4.4.3 and 4.5.3) is that they contain artifacts if the smearing is set too low with respect to the density of the k-mesh. An example of such an artifact is that a continuous band appears to consist of several disconnected emission features. These artifacts can be prevented by choosing a denser k-mesh. All calculations were checked for artifacts and a calculation with more k-points was performed when needed and if feasible. As an example, the momentum maps of freestanding 7-, 9- and 13-AGNR were tested for convergence with respect to the k-mesh by performing the momentum map simulation with a 50% denser k-mesh in all directions. The momentum maps look exactly the same for both k-meshes, thereby proving the convergence of the momentum map with respect to the k-mesh. For the AGNR on Au(111) it is, for computational reasons, in some cases not feasible to perform a calculation with a denser k-mesh. In these cases one sees artifacts and one should imagine that the dotted lines in these pictures are in reality solid lines.

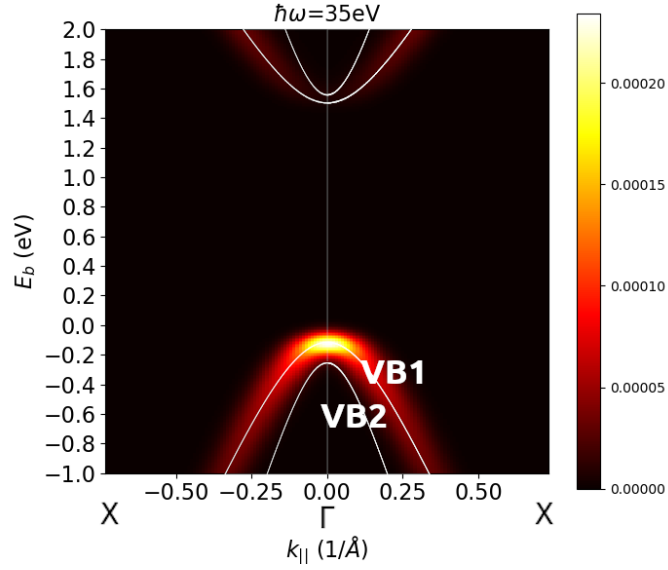


Figure 19: A simulated band map of freestanding 7-AGNR along k_{\parallel} is shown. The colors specify the photoemission intensity in arbitrary units. As an overlay, the white lines are the band structure of Fig. 15. The horizontal axis spans from -0.733 \AA^{-1} to 0.733 \AA^{-1} . It has the same length as in Fig. 15, but is shifted. The Γ - and X -point as well as the two highest valence bands (VB1, VB2) are indicated. k_{\perp} is fixed at 0 \AA^{-1} , as will be the case in all following band maps, where it is not specified otherwise.

As explained in the introduction, the ARPES band maps and momentum maps are calculated from Eq. 34. In this equation, the incident photon comes into play via the factor $|\mathbf{A}\mathbf{k}|$. One can choose an angle of incidence of the photon. This angle could be chosen to be equal to some experiment, that one wants to simulate. In this work it was refrained from doing so, because there is no specific experimental setup, that one wants to reproduce here. Therefore the polarization factor $|\mathbf{A}\mathbf{k}|$ appearing in Eq. 34 was left out in all simulations.

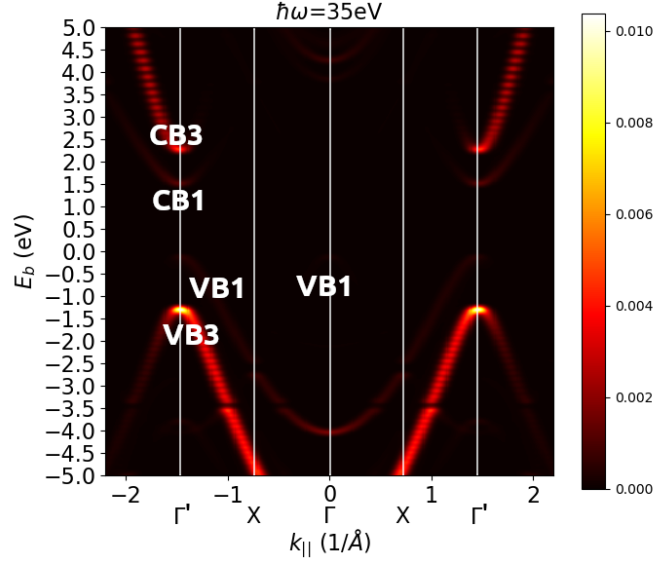


Figure 20: A simulated band map of freestanding 7-AGNR along the armchair direction is shown. k_{\parallel} is between -2.2 \AA^{-1} and 2.2 \AA^{-1} , thus its range is three times larger than in Fig. 19. Slight artifacts can be seen, since the lines are supposed to be continuous, instead of dotted, as is the case here. A look on the color bar on the right reveals that the maximum photoemission intensity is about 50 times as strong as in Fig. 19. Therefore it is very hard to see the bands, which are depicted in Fig. 19. One can clearly see that the bands in the second Brillouin zone are much brighter than the ones in the first Brillouin zone.

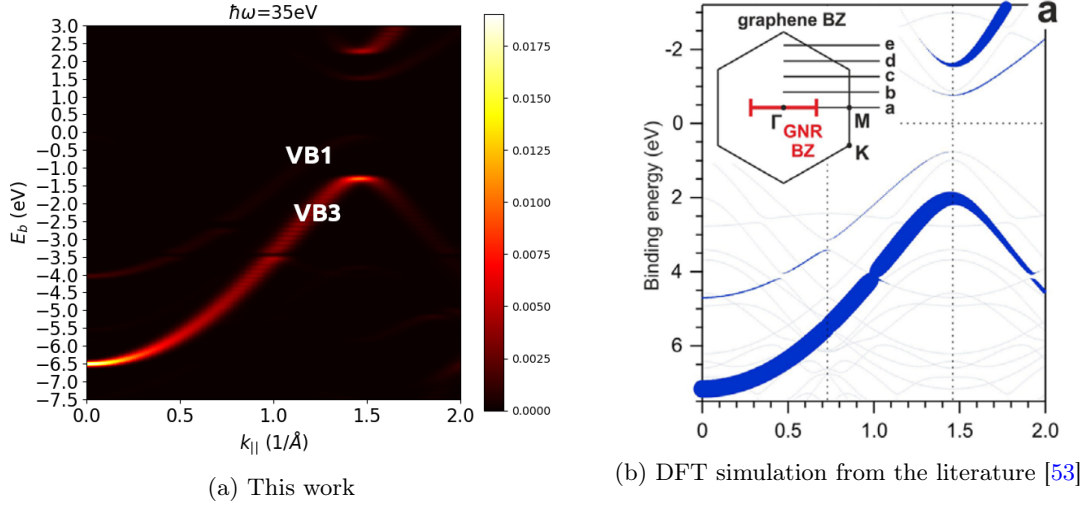


Figure 21: Band maps of freestanding 7-AGNR are shown. Note that the binding energy is defined differently in this work than it is defined by Senkovskiy et al. The difference between the definitions is a factor of -1. There is a shift between the two pictures of about 0.8 eV, which is equal to half the band gap and comes from different definitions of the Fermi energy E_F .

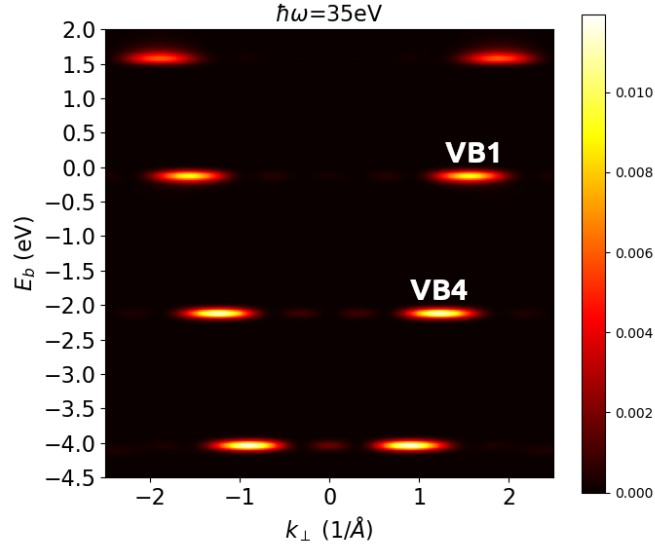


Figure 22: A simulated band map of freestanding 7-AGNR along k_{\perp} , i.e. the zig-zag direction of the AGNR, is shown. k_{\parallel} is fixed at 0 \AA^{-1} .

The band maps in Figs. 20 and 22 are checked with the momentum maps for consistency. So far, the band maps shown in this chapter are the ones of the freestanding 7-AGNR. In the following the band maps of 7-AGNR on Au(111) are presented. Due to more atoms in the unit cell and the resulting computational costs, these band maps have to be calculated with a courser k-mesh in some cases. Therefore the smearing has to be set larger and one may see artifacts of the calculation.

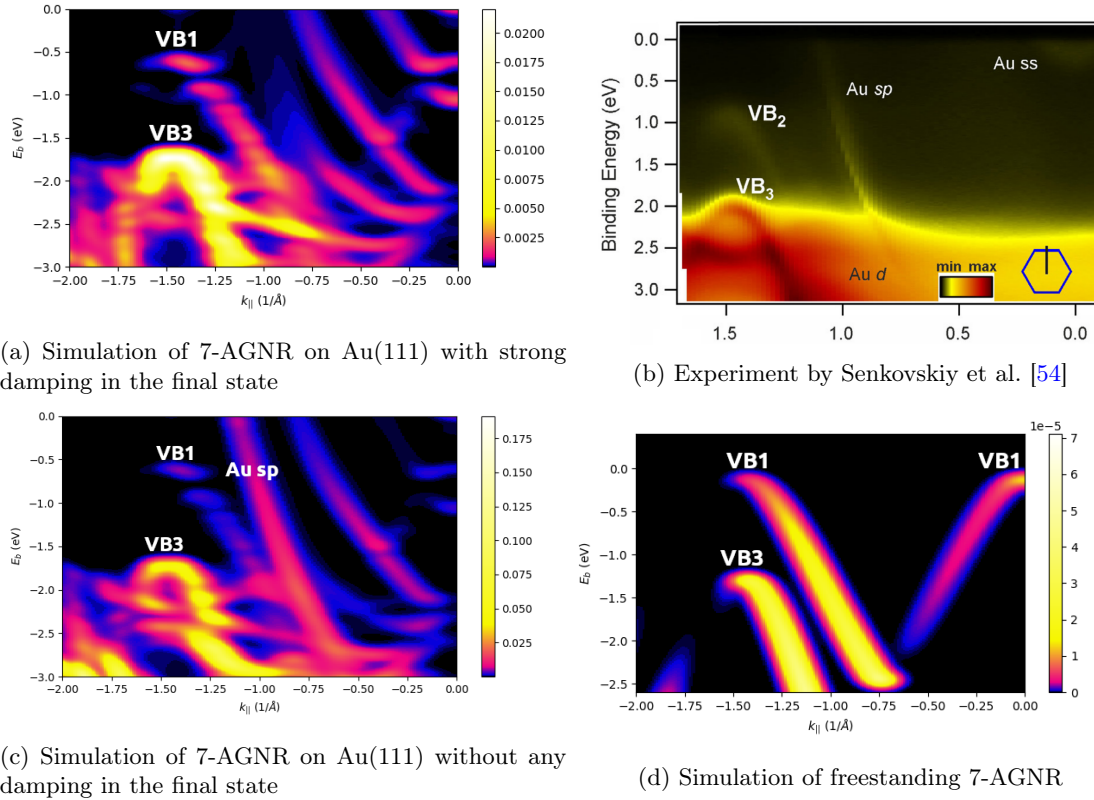


Figure 23: Band maps of 7-AGNR on gold parallel to the ribbon are shown. The simulated band maps (Figs. 23a, 23c, 23d) are smeared with $\sigma_E = 0.05$ eV and $\sigma_k = 0.05$ \AA^{-1} . The experiment is performed on 7-AGNR on Au(788) [54], while the simulations are performed on a Au(111) surface. k_{\perp} is fixed at 0 \AA^{-1} . The bands in the upper part of the simulation (Figs. 23a, 23c) have a much lower photoemission intensity than the ones in the lower part of the picture. In order to make the upper part better visible, a logarithmic colormap was used. All simulations are converged with respect to the k-mesh. A $128 \times 1 \times 1$ k-mesh was used for 7-AGNR on Au(111) as well as for freestanding 7-AGNR. In Fig. 23d, the E_b -axis range is chosen to be 0.4 eV higher to align it with the other pictures.

For a meaningful comparison of the Figs. 23a, 23b and 23d, the respective definition of the Fermi level should be considered. For the freestanding 7-AGNR (Fig. 23d), the Fermi level has been set to the top of VB_1 , while for 7-AGNR/Au(111) it is calculated self-consistently for the combined system. When comparing with the experimental energy alignment, limitations of the computational approach become evident. In the experiment, the highest valence band (VB_1) is 0.87 ± 0.03 eV below the Fermi energy and the VB_2 is 0.93 ± 0.03 eV below the Fermi energy. In the simulation of 7-AGNR on Au(111) the VB_1 is 0.61 ± 0.05 eV below the Fermi energy. Therefore, the bands of the simulated 7-AGNR on Au(111) appear to be shifted upwards by 0.26 eV compared to the experiment. For the simulated freestanding 7-AGNR, the VB_1 is 0.11 eV below the Fermi energy due to the definition of the Fermi energy for this case mentioned above.

A comparison between Figs. 23a and 23c reveals, which bands come from the 7-AGNR and Au(111) respectively. For example the emission signatures labeled with "Au *sp*-band" can be clearly identified to arise from the gold, since it is strong in Fig. 23c, but absent in Fig. 23a. With the settings that were used in this work, the Au *d*-states can not be simulated properly, as will be explained in Sec. 4.3.3.4. In essence one would need more layers of gold [55, 56]. Therefore the Au *d*-states, that can be seen below $E_b = 2.2$ in Fig. 23b, are not present in the simulation. In summary the main features of the experiment are also present in the simulation.

There is a discrepancy between the simulation of freestanding 7-AGNR and the experiment. Namely, in Fig. 23d the highest band is the VB_1 , while in the experiment (Fig. 23b) this band is identified as VB_2 by Senkovskiy et al. [54]. When the freestanding 7-AGNR, like in Fig. 23d, is depicted at different k_{\perp} -values, it can be seen that the VB_1 is brighter than the VB_2 between $k_{\perp} = 0$ \AA^{-1} and 0.10 \AA^{-1} . Then, between $k_{\perp} = 0.11$ \AA^{-1} and 0.70 \AA^{-1} the VB_2 is brighter than

the VB_1 . Therefore, according to the simulation of the freestanding 7-AGNR, the band labeled as VB_2 in the experimental band map of Senkovskiy et al. [54], should rather be identified as VB_1 . However it is very likely, that the authors of the paper know about this circumstance, considering that the paper also includes DFT simulations of freestanding 7-AGNR. An explanation of why this difference may be present, is that the electronic structure of the simulated 7-AGNR is different from the actual electronic structure of 7-AGNR on Au(788). In other words, the simulation of the freestanding 7-AGNR is slightly incorrect due to the approximations made. It is noteworthy, that the VB_2 in Fig. 23b is horizontally compressed compared to the VB_1 in Fig. 23a. This observation is evidence that the labels VB_1 in Fig. 23a and VB_2 in Fig. 23b are both correct. The inclusion of the Au(111) layer in the simulation does not change this discrepancy between experiment and simulation, as can be seen in Fig. 27.

If one uses weak damping, the resulting band map looks like a mixture between Fig. 23a and 23c. It was decided against showing the figure with weak damping, since Figs. 23a and 23c show clearer, which features arise from the gold and which from the AGNR.

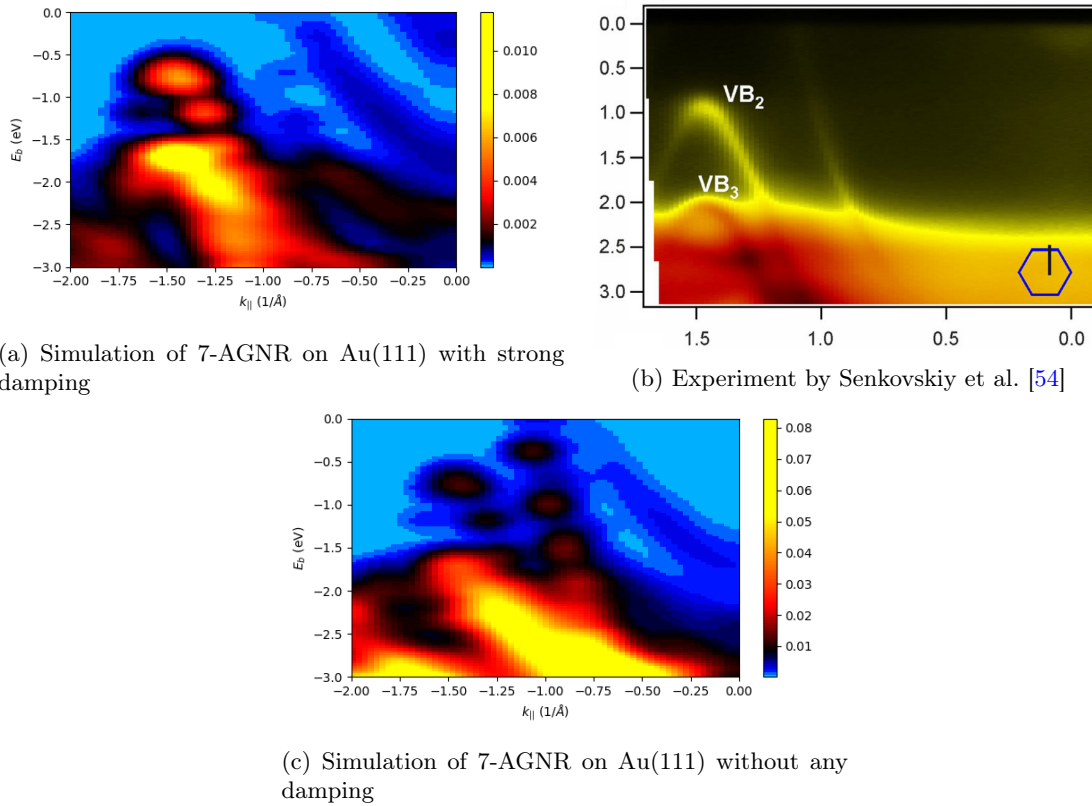


Figure 24: The band map of 7-AGNR/Au(111) parallel to the ribbon for a fixed value of $k_{\perp} = 0.3 \text{ \AA}^{-1}$ is shown. The simulated band maps are the ones of 7-AGNR on Au(111) and are smeared with $\sigma_E = 0.08 \text{ eV}$ and $\sigma_k = 0.08 \text{ \AA}^{-1}$. The experiment is performed with 7-AGNR on Au(788) [54]. The features in the lower part of the Figs. 24a and 24b have a much larger photoemission intensity than the features in the upper part of the picture. In order to see these features better, the colormap is adapted, making it roughly logarithmic. One can see artifacts of the calculation, since for example the dots in the upper part of Fig. 24c are in reality a line. The energy scales of the simulations are different than those of the experiment, because of different definitions of the Fermi level. Therefore, the simulated data appears to be shifted upwards by about 0.36 eV.

In addition to the band map with k_{\perp} fixed at 0 \AA^{-1} , also band maps for fixed values $k_{\perp} = 0.3 \text{ \AA}^{-1}$, 0.75 \AA^{-1} and 1.35 \AA^{-1} , respectively, have been simulated. Due to technical reasons, a high resolution in the simulation is currently only possible for $k_{\perp} = 0 \text{ \AA}^{-1}$. Nevertheless, for all band maps depicted in Figs. 23 - 26, one can see good agreement between simulation and experiment. The presented simulations are useful in identifying which features come from the 7-AGNR and which come from the Au(111) surface. As an example, the band in Fig. 24b to the right of VB_2

can be identified to arise from gold, by comparing Fig. 24a with Fig. 24c.

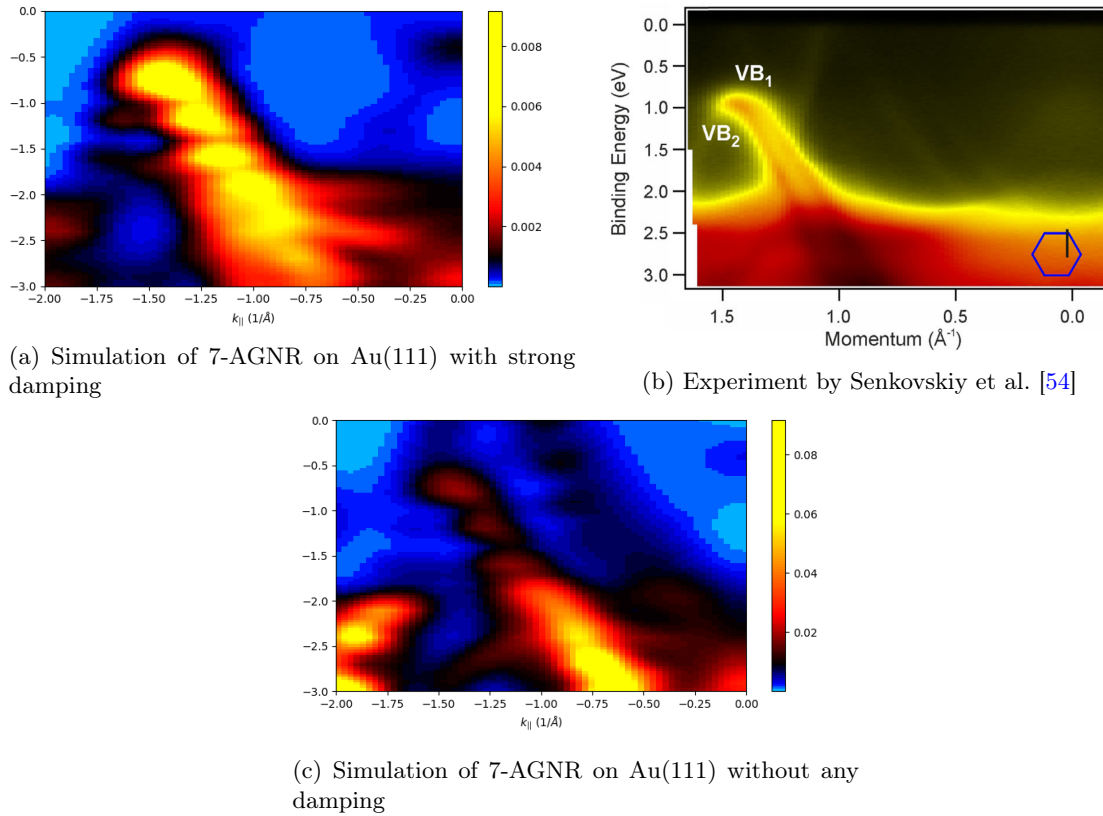
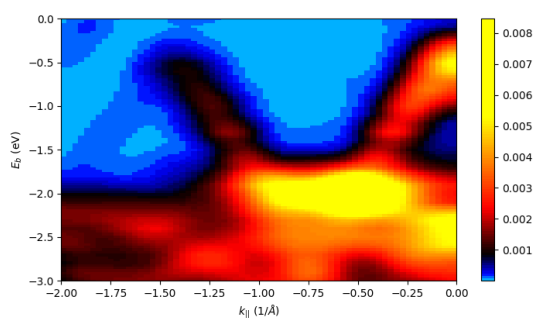
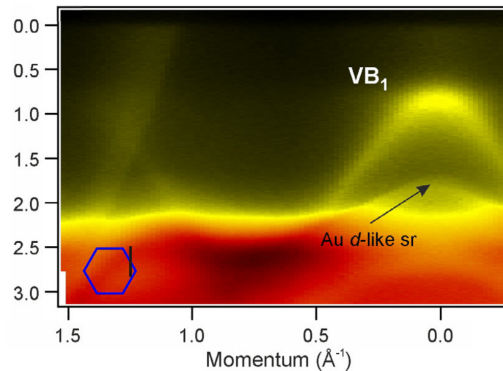


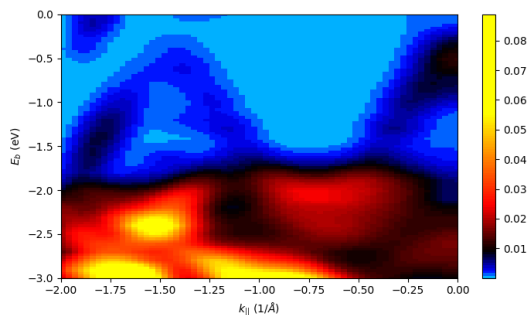
Figure 25: Band maps are depicted in a similar fashion as in Fig. 24, with the difference that k_{\perp} is here fixed at 0.75 \AA^{-1} .



(a) Simulation of 7-AGNR on Au(111) with strong damping



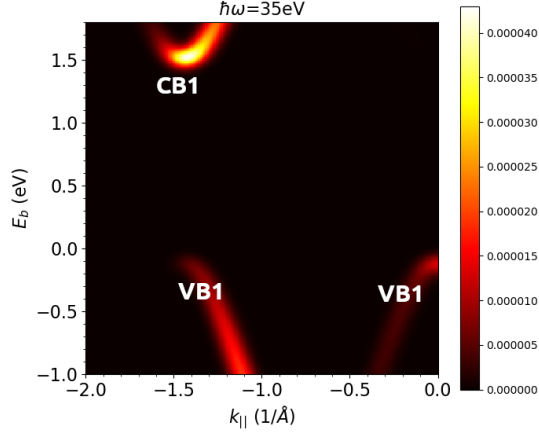
(b) Experiment by Senkovskiy et al. [54]



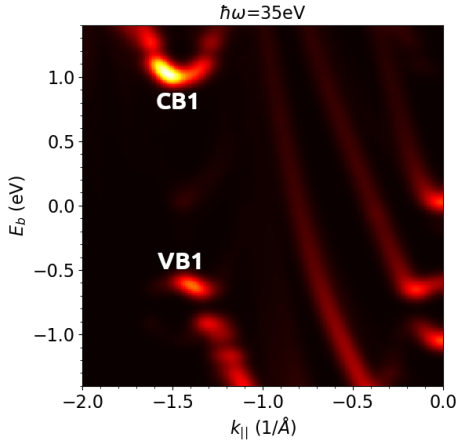
(c) Simulation of 7-AGNR on Au(111) without any damping

Figure 26: Band maps are depicted in a similar fashion as in Fig. 24, with the difference that k_{\perp} is here fixed at 1.35 \AA^{-1} .

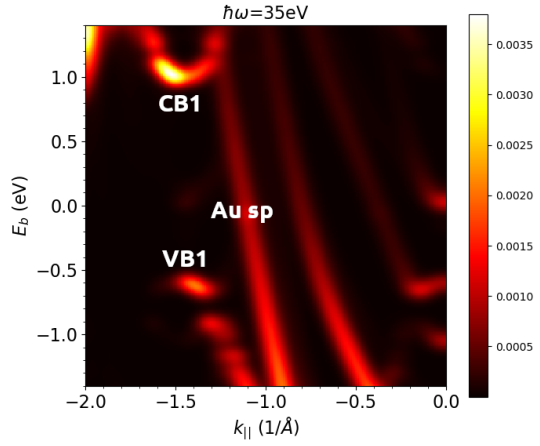
In the region between $1 < k_{\parallel} < 1.5 \text{ \AA}^{-1}$ in Fig. 26b there are two bands, which cross each other. By comparison of Fig. 26a with Fig. 26c, one can see that the band, that extends from the bottom left to the top right, comes from the gold and the band, that extends from the top left to the bottom right, comes from the AGNR. This finding can be used to identify the bands, that are seen in the experiment.



(a) Band map of freestanding 7-AGNR



(b) Band map of 7-AGNR on Au(111) with strong damping



(c) Band map of 7-AGNR on Au(111) with weak damping

Figure 27: Simulated band maps of 7-AGNR along $k_{||}$ are compared with each other. The energy range of the freestanding 7-AGNR is shifted by 0.4 eV, so that the Fermi energies align. Note that band maps are smeared with $\sigma_E = 0.05$ eV and $\sigma_k = 0.05$ eV. The differences to Fig. 23 are the binding energy range and the colormap.

Next we focus on the band structure in an energy window of ± 1.4 eV around the Fermi energy E_F , thus also including the lowest conduction band (CB_1). At this point it should be noted, that states above E_F are not visible in photoemission experiments. In Fig. 27a, one can see the lowest conduction band (CB_1) in the second Brillouin zone and the VB_1 in the first and second Brillouin zone. The first Brillouin zone is between -0.73 \AA^{-1} and 0.73 \AA^{-1} . Hence, the second Brillouin zone lies between -2.20 \AA^{-1} and -1.47 \AA^{-1} (see also Fig. 15). It is clearly visible, that the band structure of the freestanding 7-AGNR is shifted by 0.4 eV compared to the one of 7-AGNR on Au(111). The maximum photoemission intensities in Figs. 27b and 27c are similar, as can be seen in the colormap on the right. This makes it convenient to compare the two pictures with each other. There is one band, that is visible in Fig. 27c, but not in Fig. 27b. This band must come from the gold. To be more precise, it is the Au *sp*-band according to Senkovskiy et al. (Fig. 23) [54]. One can roughly measure the band gap of 7-AGNR on Au(111) to be 1.6 eV. It is very similar to the one of freestanding 7-AGNR, which is 1.61 eV. Given that the VB_1 of the freestanding 7-AGNR looks very much alike the band of 7-AGNR on Au(111), one can conclude that it is also the VB_1 in the case of the 7-AGNR on Au(111).

The band maps in Fig. 27 are created in the following way: The electron density of freestanding

7-AGNR was calculated with a $64 \times 8 \times 8$ k-mesh and was then kept constant during a second calculation, in which a $128 \times 1 \times 1$ k-mesh was used. The shown band map is converged with respect to the k-mesh. In the case of the 7-AGNR on gold, the electron density was calculated with a $8 \times 5 \times 3$ k-mesh. Then, DFT calculations with a $128 \times 1 \times 1$ and $64 \times 1 \times 1$ k-mesh were performed with fixed electron density. The band maps resulting from these two DFT simulations were compared with each other. They look exactly the same, thereby proofing convergence with respect to the k-mesh.

4.3.3 Photoemission Momentum Maps

A "momentum map" is plot of the photoemission intensity $I(k_{\perp}, k_{\parallel})$, where the two axis are the components of the wave vector k_{\parallel} and k_{\perp} . This chapter starts with a discussion of symmetry, which will be used to analyze the momentum maps. Then, it will be investigated, what role the different adsorption positions play on the momentum maps. Finally, simulated momentum maps of freestanding 7-AGNR and 7-AGNR on Au(111) will be analyzed and compared to experiment.

4.3.3.1 Symmetry Argument for Momentum Maps

In this section, the symmetries of the AGNR and Au(111) are reviewed, and consequences for the momentum maps are deduced from these symmetries. Looking at Fig. 10a, one can see that the AGNR and Au(111) surface have different symmetries in this top view. It is evident that the AGNR has a mirror symmetry around both the horizontal as well the vertical axis, which leads to a D_{2h} symmetry in Schönflies notation. Periodic boundary conditions should be kept in mind, which have the effect, that it does not matter for the momentum maps whether the AGNR is centered in the unit cell. Considering only a plane parallel to the surface, the Au(111) has only a symmetry about the horizontal axis and a 3-fold rotational symmetry, and thus has a D_3 symmetry in two dimensions.

In this paragraph, the consequences of aforementioned symmetries will be investigated. We will first consider the symmetry about the k_{\perp} -axis, and then the symmetry about the k_{\parallel} -axis. Since both the AGNR as well as the Au(111) have a symmetry about the horizontal axis k_{\perp} , this symmetry must be present in all momentum maps, if the symmetry axis of both subsystems align. They align for the "atom hollow", "atom top" and "bond hollow" adsorption site (Figs. 10a, 10b, 10c), but not for the "bond top" adsorption site (Fig. 10d). Indeed this symmetry about the horizontal axis k_{\perp} can be seen in all momentum map simulations, that have been performed. Even in the case of the "bond top" adsorption site, all momentum maps have this symmetry. Coming now to the symmetry about the k_{\parallel} -axis, it can be seen that the AGNR possesses this symmetry, while the Au(111) does not. This asymmetry can be seen in some momentum maps. For example the momentum maps in Fig. 28, do not possess a mirror symmetry with respect to the k_{\parallel} -axis. Said asymmetry cannot come from the AGNR alone, since it is symmetric about that axis. Rather, it must come from the gold or the interaction between the gold and the AGNR. The previous two sentences are at the heart of this symmetry argument. It is useful for analyzing momentum maps, because one can conclude that features, that are asymmetric about the central vertical axis, must stem from the gold or interactions between the gold and the AGNR. The term "interaction between the gold and the AGNR" can be understood very generally here, accounting for the displacement of atoms as well as changes to the electron density and resulting changes in the Kohn-Sham orbitals. However, it turns out that the former effect, the displacement of atoms, is negligible.

It will now be analyzed, where the asymmetry about the k_{\parallel} -axis is present. Said asymmetry is not at all present for strong damping ($\gamma = 0.5$, z_0 between topmost gold layer and AGNR) for all systems that are investigated in this work. These are the 7-, 9- and 13-AGNR on Au(111) at binding energies between 0 eV and -2.3 eV. The reason for this absence is that the strong damping nullifies the contribution of the region, from which this asymmetry arises. For weak damping ($\gamma = 0.1$, z_0 at topmost gold layer) one can see gold features, which possess this asymmetry, throughout the whole binding energy range. The stronger features, that mainly come from the AGNR, obey the symmetry for binding energies between 0.0 eV and -1.7 eV, while they are asymmetric between -1.8 eV and -2.3 eV, as in Fig. 28 for example. This finding is consistent with the density of states (DOS) in Fig. 17. The DOS of gold rapidly increases below about -1.8 eV due to emissions from the d -bands, which has the effect that the relative contribution of the gold gets much larger. Further analysis using this symmetry argument will be done in the corresponding sections about the momentum maps.

This section will be ended with some side notes on the symmetry argument. Taking into account also the third dimension, which is perpendicular to the slab, one can think about how the interaction between the Au(111) surface and the AGNR displaces the atoms in this direction. Of course the AGNR gets attracted or repelled until it is at its corresponding adsorption height. Apart from this effect, the displacement is very small, as can be seen in Fig. 6b. Except for a slight bending, the atoms basically remain in their original position prior to the adsorption on Au(111).

4.3.3.2 Differences in Momentum Maps due to Adsorption Positions

After having qualitatively analyzed the role of symmetry on the momentum maps in the previous subsection, we now discuss the influence of the adsorption site in detail. A comparison between momentum maps of the 7-AGNR on different adsorption sites can be seen in Fig. 28. All pictures look similar, however one can identify two pairs which look nearly identical. On the one hand the "atom hollow" and "bond hollow" site look almost identical, and the "atom top" and "bond top" configuration look almost identical as well. This observation is coherent with the adsorption energies in Fig. 13.

The largest difference due to adsorption positions can be seen for weak damping ($\gamma = 0.1$, z_0 at topmost gold layer) and in the region between binding energies E_b of -1.8 eV and -2.3 eV, which is the region that is dominated by Au d -states. (These are the minimum binding energies that were investigated in this work, since binding energies between 0 eV and -2.3 eV were analyzed.) This can be understood in terms of the symmetry argument presented in Sec. 4.3.3.1. The asymmetry about the axis, where $k_{\parallel} = 0$, is present in the E_b -range between -1.8 eV and -2.3 eV. This asymmetry comes from the gold or the interaction between the gold and AGNR. Different adsorption positions obviously change the interaction between gold and AGNR, therefore some change with respect to adsorption position is present in the E_b -range, where the effects of said interaction make an appearance in the momentum map.

Adding to this argument, one can also conclude that the differences due to adsorption sites must come from the interaction between the gold and AGNR, but not from the gold on its own. This must be the case, since the Au(111) surface is the same for all adsorption positions. It can not be concluded that all the horizontal asymmetry arises from the interaction between gold and AGNR, but only the differences between Figs. 28a, 28b, 28c and 28d, i.e. some asymmetry may come from the gold alone. Interestingly, the features at $(0, \pm 1.3) \text{ \AA}^{-1}$ are mostly unaffected by changing the adsorption position. This might be a hint that this feature arises from the AGNR. As will be shown in Fig. 32a, the AGNR indeed has a feature at this spot.

For Fig. 28, a binding energy, which maximizes the difference due to adsorption positions, has been chosen. It should be noted that, these differences are much smaller for other binding energies. More so, if strong damping ($\gamma = 0.5$, z_0 between topmost gold layer and AGNR) is used, the features are qualitatively identical for different adsorption positions. Some very slight differences can be spotted, which do not change the overall appearance of the features and are insignificant with respect to the accuracy of the calculation. Momentum maps of the "bond hollow" and "bond top" adsorption sites, which are the two sites with the largest energy difference, are compared with each other for binding energies between 0 eV and -2.4 eV and they were qualitatively identical for strong damping. For weak damping however, they were only qualitatively identical in the binding energy regions between 0 eV and -1.7 eV. Binding energies above 0 eV and below -2.4 eV were not investigated in this work.

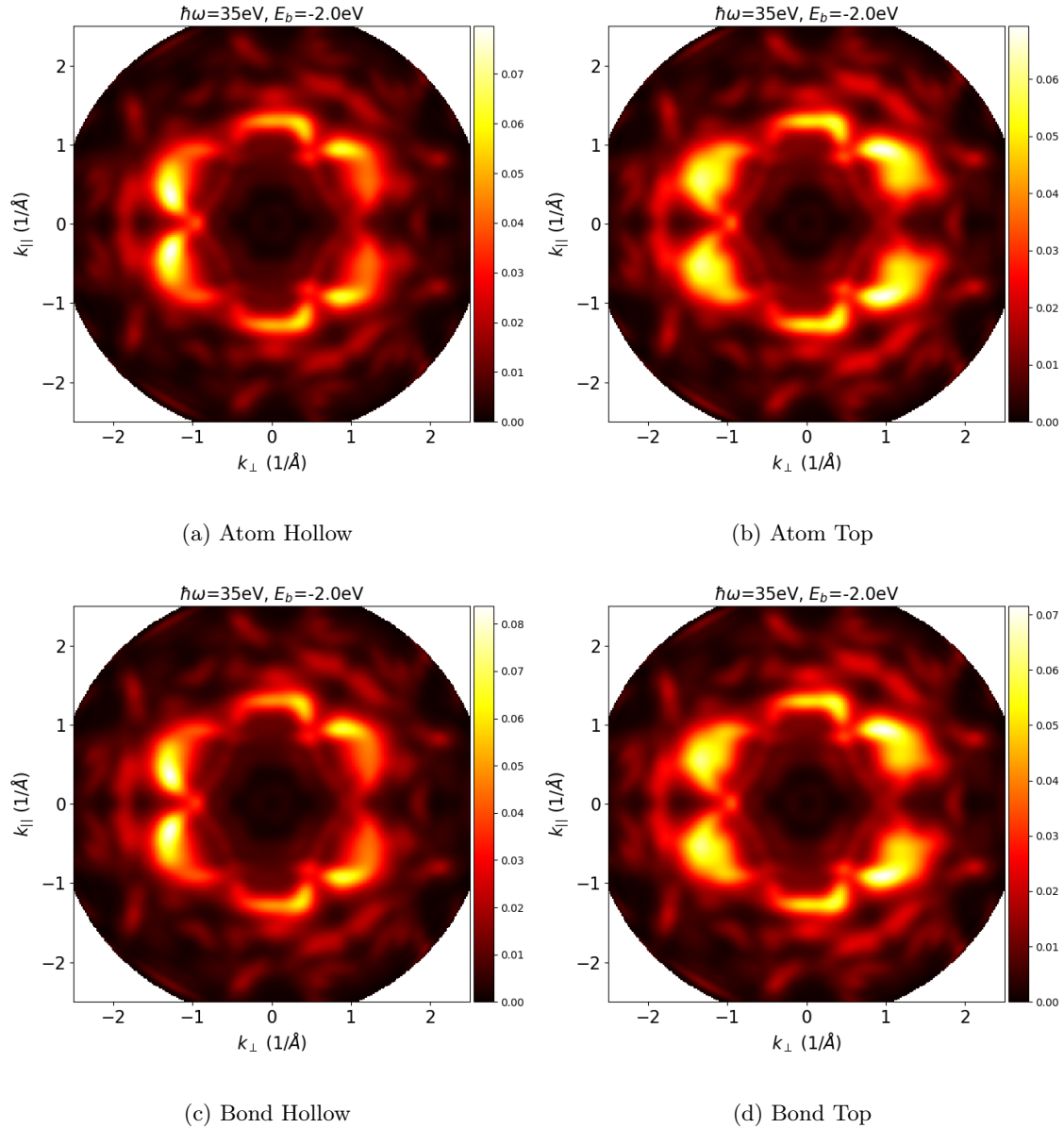


Figure 28: The influence of the adsorption site on simulated ARPES k-maps of 7-AGNR on Au(111) is shown. Most relevant simulation parameters are binding energy $E_b = -2.0$ eV, smearing in k-space $\sigma_k = 0.08 \text{ \AA}^{-1}$, photon energy $\hbar\omega = 35$ eV and weak damping ($\gamma = 0.1$, z_0 at topmost gold layer). The different colors indicate the photoemission intensity and a colormap can be seen on the right of each k-map.

From the finding that the k-maps look qualitatively the same for all four adsorption sites (except for weak damping between $E_b = -1.8$ eV and -2.3 eV), it can be concluded that different adsorption position generally do not have a significant impact on the qualitative features of the momentum maps. Therefore a thorough analysis of the exact adsorption position of AGNR on Au(111) is not necessary, if one is interested in the features of the momentum maps. On the other hand, one must also conclude that it is virtually impossible to deduce information about the adsorption site based on experimental ARPES data. In the following analysis of the momentum maps, one could choose any of the four adsorption positions and come to similar results, since this choice does not make a significant difference in the momentum maps. However, the lowest energy position is the natural choice, since it has the highest probability of being the true adsorption position or at least close to it. Wherever not stated otherwise, it was decided to choose the position with the lowest energy, which is the "bond hollow" position.

As a side note, one can see a slight downwards bending on both sides of the AGNR, like in Fig.

6b. This bending is roughly the same for all adsorption positions. An explanation of this bending is given by Weiß et al. for (3,1)-GNR/Cu(111) (Fig. 5 of [39]) and is further discussed at the end of Sec. 4.2.4.

4.3.3.3 Comparison with Senkovskiy et al.

For the freestanding 7-AGNR, a comparison between the result of this work and a DFT simulation from the literature was made and can be seen in Fig. 29. According to the paper, "the energy scale in DFT [...] calculations was rigidly shifted to align the experimental and calculated valence band maxima. [...] The calculated bands were broadened with $\beta = 0.1$ eV to compare with the experiment." [54] In order to obtain Fig. 29b the binding energy was shifted to align with 29a. In doing so it was found that, for a binding energy of -1.2 eV, which is 1.2 eV below the Fermi energy, both results align nicely. The broadening of the bands was chosen to be $\beta = 0.03$ eV and the photon energy was chosen to be 45 eV. Senkovskiy et al. used a k-point grid of $12 \times 1 \times 1$, while in this work a k-point grid of $64 \times 8 \times 8$ was used. Considering the difference in k-meshes with a simultaneously similar accuracy of the result, it is likely that Senkovskiy et al. used free boundary conditions within the FPLO package. In both works the forces on atoms were relaxed until they were less than 0.01 eV \AA^{-1} . A comparison of Fig. 29a to experiment can be found in the paper.

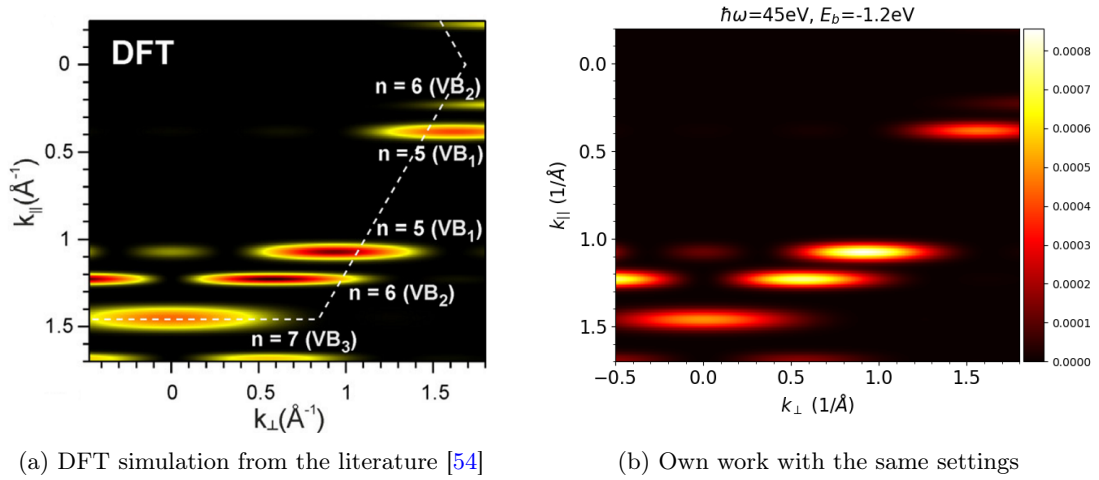


Figure 29: ARPES k-maps of freestanding 7-AGNR are compared with each other. In Fig. 29a a result from the literature is depicted and in Fig. 29b the result of this work can be seen. The different colors indicate the photoemission intensity, of which a colormap can be seen on the right of Fig. 29b. The units of the photoemission intensity are arbitrary.

4.3.3.4 Additional Comparisons with Experimental Data

The present simulations of ARPES momentum maps are further compared to experimental data recorded by Xiaosheng Yang and co-workers [49]. This data has been recorded using the toroidal electron energy analyzer located at the synchrotron in Berlin using a photon energy of 35 eV and covers a binding energy range from -2.4 eV to the Fermi edge. Due to practical reasons, the momentum maps are only shown at selected binding energies, as described in Sec. 4.3.1. In that section, the binding energies -0.4 eV, -1 eV and -1.8 eV were identified as binding energies of interest for momentum maps of 7-AGNR on Au(111). Note again that the binding energies of freestanding 7-AGNR are shifted by -0.4 eV with respect to the ones of 7-AGNR on Au(111). Thus, these are shown at binding energies of 0.0 eV, -0.6 eV and -1.4 eV. The following settings are used for the simulation of the ARPES k-maps: The photon energy is set to 35 eV. The k-map of the freestanding AGNR is smeared by 0.05 \AA^{-1} in both the k_{\parallel} - as well as the k_{\perp} -direction. The k-mesh of the AGNR on Au(111) has to be coarser due to limited computational resources. Thus the smearing is larger and set to 0.08 \AA^{-1} for the k-maps of AGNR on gold. These settings apply to 7-AGNR as well as to 9-AGNR and 13-AGNR. It should also be noted that the simulations are

performed on Au(111), while the experiments are performed on the stepped Au(788) surface. This might introduce differences between experimental and simulated k-maps, however these differences are expected to be small.

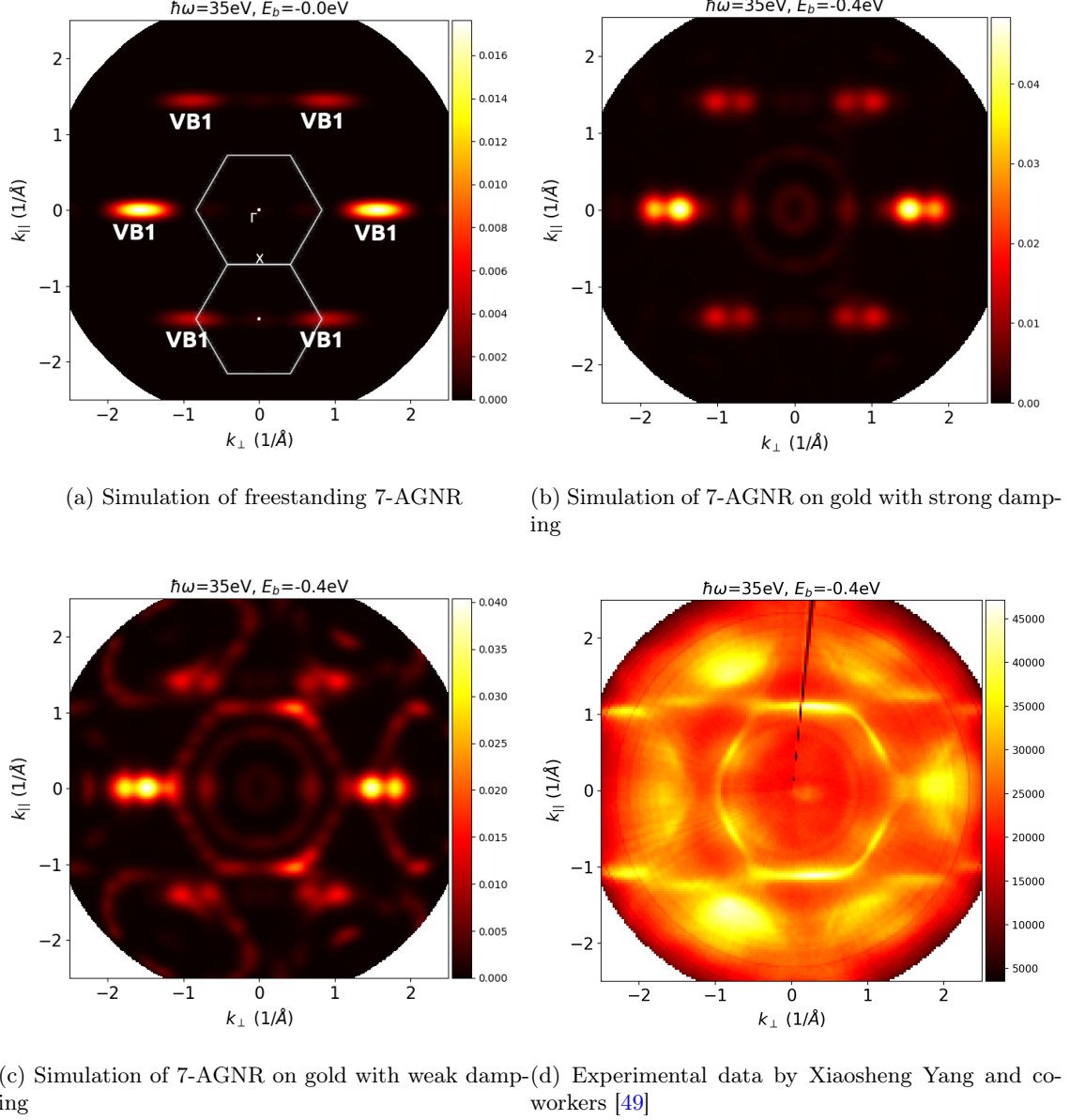
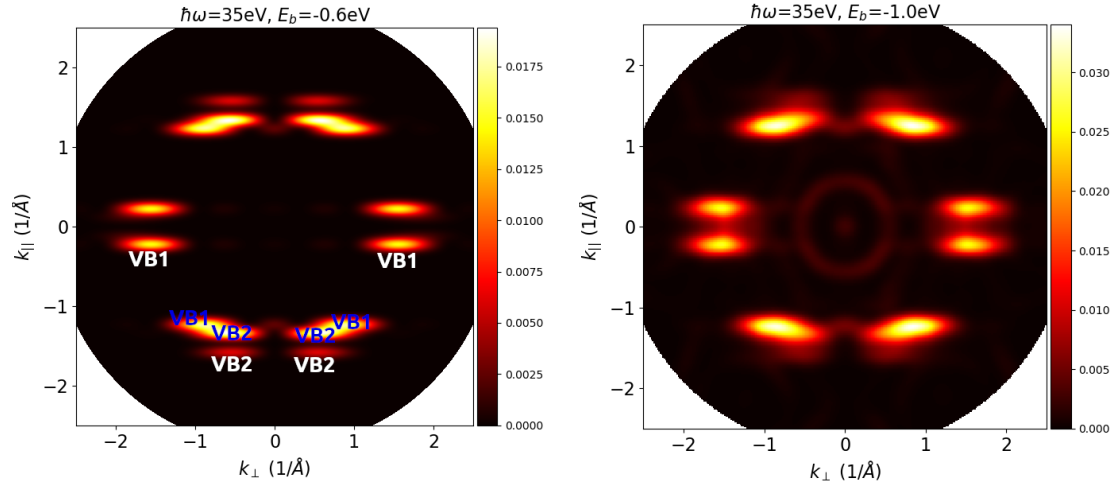


Figure 30: Simulated and experimental ARPES k-maps are compared with each other. The artificially introduced smearing amounts to 0.05 \AA^{-1} for the freestanding 7-AGNR and 0.08 \AA^{-1} for 7-AGNR on Au(111). The settings "strong damping" and "weak damping" are explained in the end of chapter 2.3. The highest valence band (VB_1) of the freestanding 7-AGNR is indicated in Fig. 30a. Additionally, the first and second Brillouin zones are shown, including the Γ - and X -point.

Fig. 30 will be analyzed in the following, starting with signatures of AGNR. Thereafter, effects of the gold will be explained. The most prominent feature of 7-AGNR can be seen at $(k_{\perp}, k_{\parallel}) = (0, \pm 1.7) \text{ \AA}^{-1}$ in Figs. 30a, 30b and 30c. This feature is also present in the experiment (Fig. 30d), however there it is broadened with respect to the simulation. It is a general aspect of ARPES, that spatially extended structures like the Au(111) surface give sharp k-map features, while spatially confined structures like an AGNR give broader features, that are more washed-out. This aspect can be clearly seen with said 7-AGNR feature at $(k_{\perp}, k_{\parallel}) = (0, \pm 1.7) \text{ \AA}^{-1}$. The broadening can

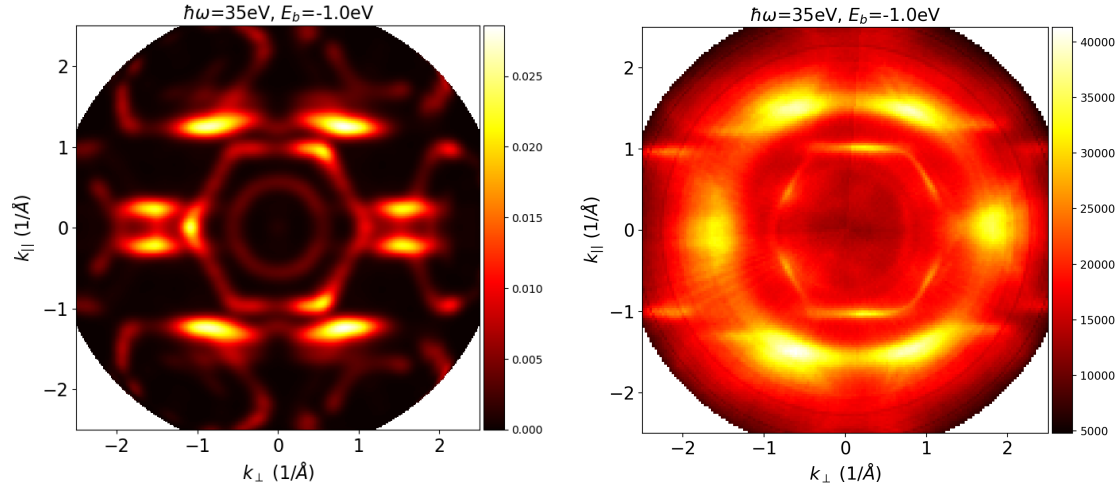
be understood by considering the finite length of the AGNRs in the experiment. The produced 7-AGNR do not all have the same length, rather there is a distribution of different nanoribbon lengths. (For example, this can be seen in the STM image of Fig. 3A in [57].) These nanoribbons of different lengths have slightly different electronic structures. ARPES averages over a region in space, thereby averaging over this distribution of nanoribbons. Additionally, the nanoribbons in the experiment may have slightly different orientations, which would have the same effect of broadening the AGNR features. In contrast to the real world experiment with a certain degree of disorder, in the simulation the AGNR is infinitely long and perfectly aligned. This explanation is affirmed by the observation, that the 7-AGNR features are broadened in the k_{\parallel} -direction, and much less so in the k_{\perp} -direction. Additionally to the feature at $(k_{\perp}, k_{\parallel}) = (0, \pm 1.7) \text{ \AA}^{-1}$, the 7-AGNR also has a feature at $(k_{\perp}, k_{\parallel}) = (\pm 0.9, \pm 1.5) \text{ \AA}^{-1}$. This feature can be seen in the simulation as well as the experiment, with broadening in the latter case. Overall, the features of 7-AGNR in the simulation agree reasonably well with experiment.

Coming now to the Au(111) features, we can easily identify them by comparing Figs. 30a, 30b and 30c with each other. Essentially, the gold features can be identified by subtracting the features of the freestanding 7-AGNR (Fig. 30a) from the k-map of weakly damped 7-AGNR on Au(111) (Fig. 30c). We can see that the "strong damping" (Fig. 30b) is indeed very strong, since barely any gold features remain after the damping is applied. The most prominent gold feature is a hexagon in the middle of the k-map. It can be recognized in the simulation (Fig. 30c) as well as the experiment (Fig. 30d). The horizontal lines at $(k_{\perp}, k_{\parallel}) = (\pm 2.1, \pm 1) \text{ \AA}^{-1}$ in Fig. 30d arise from the gold as well. The 7-AGNR feature at $(k_{\perp}, k_{\parallel}) = (0, \pm 1.7) \text{ \AA}^{-1}$ in Fig. 30d is superimposed by sharp lines, that come from the gold and form half a hexagon together with the features at $(k_{\perp}, k_{\parallel}) = (\pm 2.1, \pm 1) \text{ \AA}^{-1}$. Again, the features of Au(111) in the simulation agree fairly well with experiment.



(a) Simulation of freestanding 7-AGNR

(b) Simulation of 7-AGNR on gold with strong damping



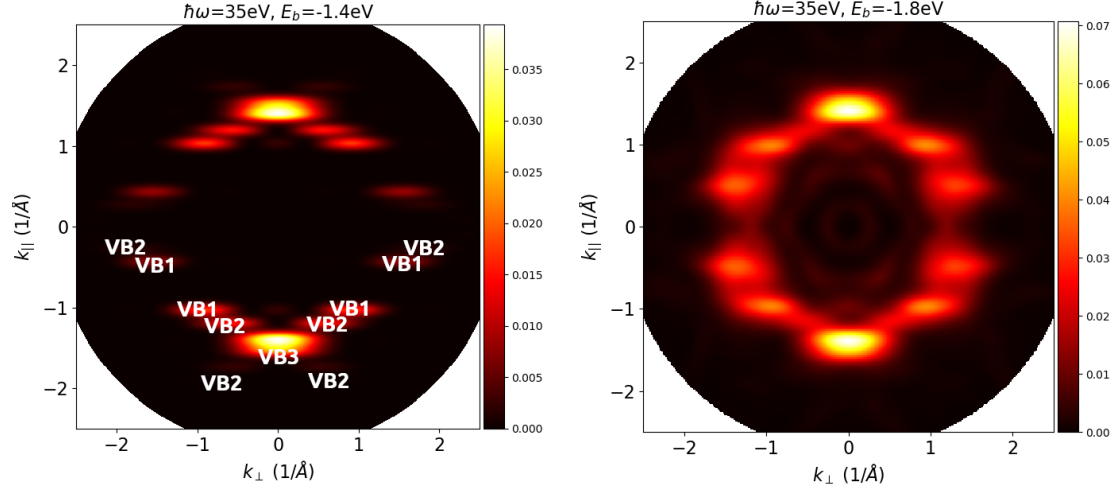
(c) Simulation of 7-AGNR on gold with weak damping

(d) Experimental data by Xiaosheng Yang and co-workers [49]

Figure 31: ARPES k-maps are compared to each other in the same fashion as in Fig. 30, but here they are shown at lower binding energies E_b . The binding energy of the freestanding 7-AGNR is shifted by 0.4 eV to align with the other k-maps, as explained in Sec. 4.3.1. In Fig. 30a and in the following, only the bands in the lower half will be labeled, the labels of the upper half follow in a trivial manner by mirroring the image. When necessary, labels are colored differently to increase visibility.

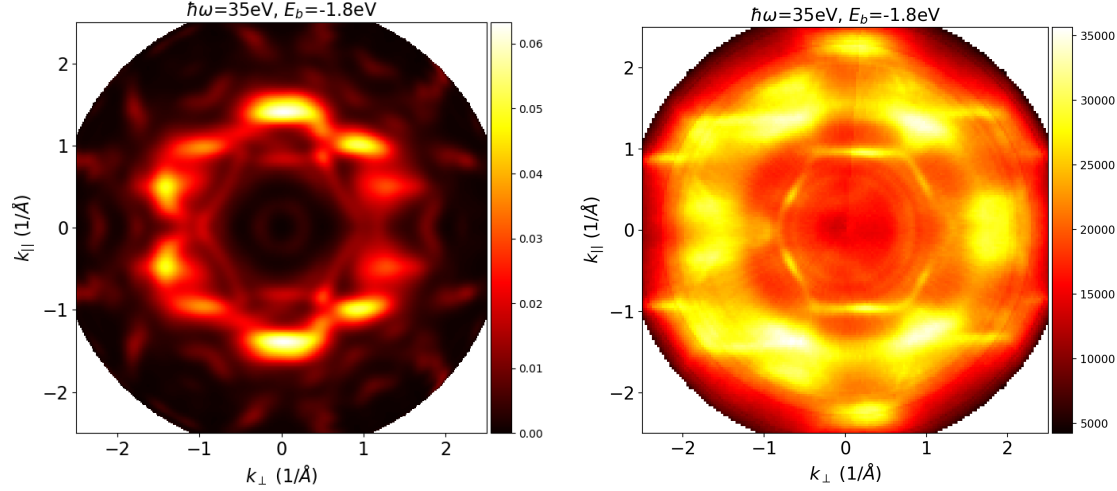
In the same manner as above, we will first focus on the 7-AGNR features in Fig. 31 and then move on to the gold features. In the band map of freestanding 7-AGNR (Fig. 19), it can be seen that the highest valence band (VB_1) gives rise to two features, if one makes a cut at $E_b = -0.6$ eV. Phrased differently, the feature at $(k_\perp, k_\parallel) = (0, \pm 1.7) \text{ \AA}^{-1}$ and $E_b = 0.0$ eV in Fig. 30a splits into two features if one moves to lower binding energies, like in Fig. 31a ($E_b = -0.6$ eV). This splitting is visible at $(k_\perp, k_\parallel) = (0, \pm 1.7) \text{ \AA}^{-1}$ in Figs. 32a, 31c and 31b. However, in the experiment (Fig. 31d) such a splitting is presumably smeared out due to disorder effects mentioned above. Nevertheless, upon close inspection, one may see a hint of this splitting.

A comparison of Fig. 31c with Figs. 32a and 31b reveals, which features come from the Au(111) surface. They look qualitatively the same as in Fig. 30. In total, the agreement between simulation and experiment is very good at this binding energy.



(a) Simulation of freestanding 7-AGNR

(b) Simulation of 7-AGNR on gold with strong damping



(c) Simulation of 7-AGNR on gold with weak damping

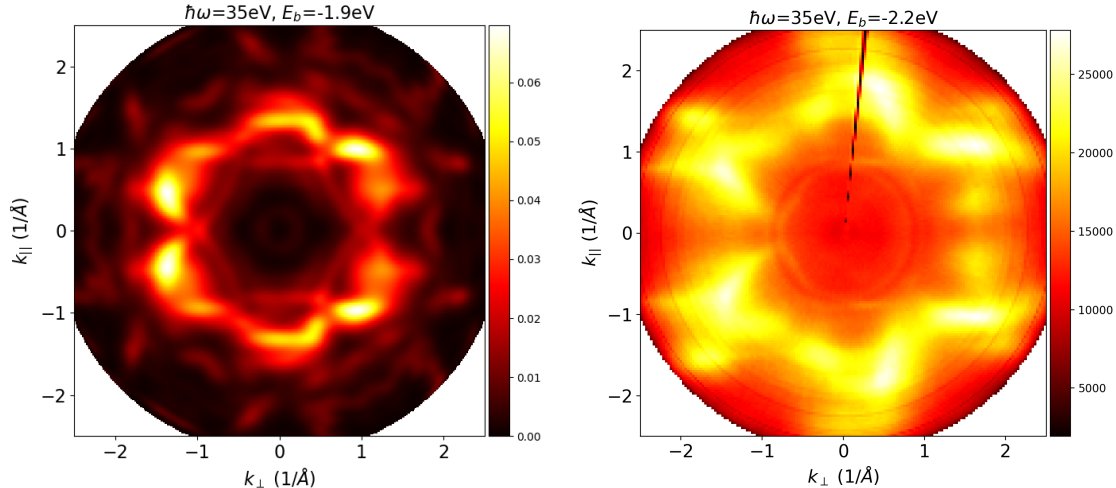
(d) Experimental data by Xiaosheng Yang and co-workers [49]

Figure 32: ARPES k-maps are compared to each other in the same fashion as in Fig. 30 and 31. Here, $E_b = -1.8$ eV in Figs. 32b, 32c and 32d. As above, the binding energy is 0.4 eV higher for freestanding 7-AGNR.

In the following analysis of Fig. 32, we will first focus on the 7-AGNR features and then move on the gold features. The strongest feature in the experiment (Fig. 32d) is the one at $(k_\perp, k_\parallel) = (\pm 0.9, \pm 1.3) \text{ \AA}^{-1}$ and it can be seen in the simulations (Figs. 32a, 32b, 32c) as well. This feature must stem from the 7-AGNR, since it is present in Fig. 32a and 32b. For this feature there is an agreement between simulation and experiment. Coming now to the disagreements, we can see that there are quite a few at first glance, however some of these will be resolved. The strong feature at $(k_\perp, k_\parallel) = (0, \pm 1.4) \text{ \AA}^{-1}$ is clearly present in the simulations (Figs. 32a, 32b, 32c), but it is not at all present in the experiment (Fig. 32d). This discrepancy will be explained in Fig. 33 and the discussion thereafter. In essence, the simulation should be compared to experiments at lower binding energies. At these energies, the feature at $(k_\perp, k_\parallel) = (0, \pm 1.4) \text{ \AA}^{-1}$ appears in the experiment. The discrepancies between the features near $(k_\perp, k_\parallel) = (\pm 1.5, \pm 0.5) \text{ \AA}^{-1}$ in Figs. 32c and 32d can also be explained by this argument. The most fundamental disagreement between experiment and simulation lies in the feature at $(k_\perp, k_\parallel) = (0, \pm 2.3) \text{ \AA}^{-1}$, that can be seen in the experiment (Fig. 32d). This feature is present in the experiment for binding energies between

$E_b = -1.6$ eV and $E_b = -2.1$ eV, while it is absent in all simulations.

As above, the gold features can be identified by their sharpness with respect to the 7-AGNR features. The hexagonal and the horizontal lines, coming from the gold, are similar to Figs. 30 and 31.



(a) Simulation of 7-AGNR on gold with weak damp- (b) Experimental data by Xiaosheng Yang and co-workers [49]

Figure 33: As an extension to Fig. 32, k-maps of simulation and experiment are shown at different binding energies.

Fig. 33 extends Fig. 32 and explains the absence of a feature at $(k_{\perp}, k_{\parallel}) = (0, \pm 1.4) \text{ \AA}^{-1}$ in Fig. 32d. This absence can be explained in the following fashion: According to Fig. 18, GGA erroneously results in a too small Π -band width. Therefore, the simulations should be compared with experimental data at lower binding energies. Following this argument, the binding energy of the experiment is rigidly shifted to align with the simulation. Good agreement is found for $E_b = -1.9$ eV of the simulation and $E_b = -2.2$ eV of the experiment, as can be seen in Fig. 33. With this setting, the features of the experiment and simulation align reasonably well, and discrepancies in the comparison shown in Fig. 32 can be dissolved. To be more precise, the feature at $(k_{\perp}, k_{\parallel}) = (0, \pm 1.4) \text{ \AA}^{-1}$ and the features near $(k_{\perp}, k_{\parallel}) = (\pm 1.5, \pm 0.5) \text{ \AA}^{-1}$, which are left-right-asymmetric, can be understood that way.

Figures 33a and 33b have a clear left-right-asymmetry overall. The symmetry argument from Sec. 4.3.3.1 can be applied here. In essence, it states that the left-right-asymmetry must come from the gold or the interaction of the gold with the AGNR. In the feature at $(k_{\perp}, k_{\parallel}) = (0, \pm 1.4) \text{ \AA}^{-1}$ such a left-right-asymmetry can be seen as well, therefore it must come (at least partially) from the gold or the interaction of the gold with the AGNR. Additionally, it must come (at least partially) from the 7-AGNR, because it is present in Fig. 32a and 32b. Thus, one comes to the interesting conclusion that this feature is a mix between gold and AGNR contributions. It should also be noted that, in this binding energy range, already emissions from Au d -states are to be expected. And since d -states are more localized in real space, their corresponding features in k -space are of comparable width as emission signatures from the AGNR.

In summary, all features of the comparison between simulation and experiment (Fig. 32) can be explained at least to some extent, with the exception of the feature at $(0, \pm 2.3)$ in Fig. 32d. The lack of this feature, might be due to inaccuracies in the simulation. One has to keep in mind that, multiple approximations, e.g. the generalized gradient approximation (GGA), are made in order to make the simulation computationally tractable.

At this point, it would be interesting to compare Fig. 33 with a simulation of a Au(111) surface without the AGNR. This is however not fruitful with the settings that are used in this work so far. The main reason for this is that the sp -states, which are present at the surface of the gold, extend over a relatively long distance into the gold. Thus many layers of gold would be necessary to describe them correctly (see Fig. 4.20 in [55]). Additionally, the plane wave final

state approximation is not well suited to describe a gold surface. A proper ARPES simulation of Au(111) was performed by Feidt et al. [56]. Performing such a simulation in addition to the other ones, that were already presented here, would go beyond the scope of this thesis and would miss the topic of this work, which are AGNRs.

4.4 Electronic Structure of 9-AGNR

This section is structured in analogy to Sec. 4.3, with the difference that here the 9-AGNR is treated instead of the 7-AGNR. First, the simulated band structure of freestanding 9-AGNR and the density of states (DOS) of freestanding 9-AGNR and 9-AGNR on Au(111) will be presented. Secondly, photoemission band maps of freestanding 7-AGNR as well as those of 9-AGNR on Au(111) are shown. Thirdly, momentum maps of freestanding 9-AGNR and 9-AGNR on Au(111) are presented.

4.4.1 Band Structure and DOS

The simulated band structure of freestanding 9-AGNR can be seen in Fig. 34. The band gap is 0.78 eV wide, which is in accordance with a DFT LDA result from Zhu et al, who calculated it to be 0.79 eV [50].

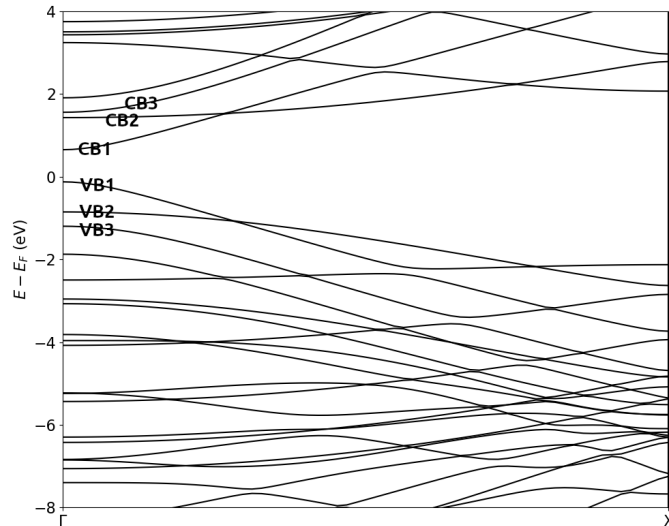


Figure 34: The band structure of freestanding 9-AGNR parallel to the ribbon is shown. The electron density is calculated with a $64 \times 8 \times 8$ k-mesh. Then, a DFT calculation with a $128 \times 1 \times 1$ is performed with fixed electron density. Finally, the latter calculation is used to calculate the band structure.

In the same manner as with 7-AGNR, the DOS of 9-AGNR was simulated. It is used to identify binding energies of interest for momentum maps.

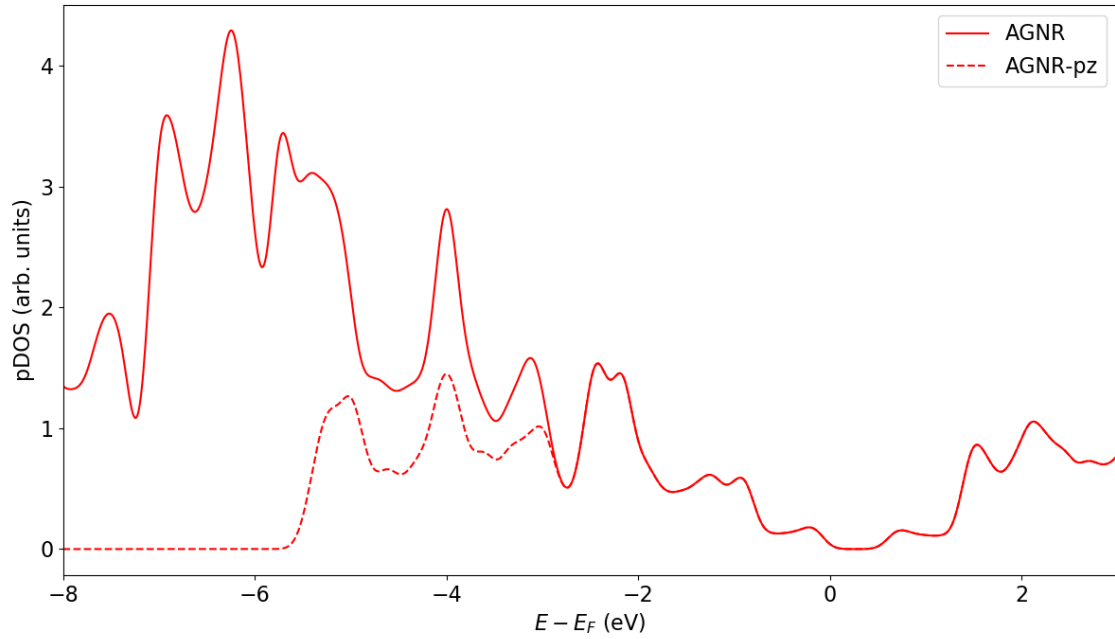


Figure 35: The DOS of the freestanding 9-AGNR is shown. It is smeared with 0.1 eV and a k-mesh of $45 \times 9 \times 12$ was used.

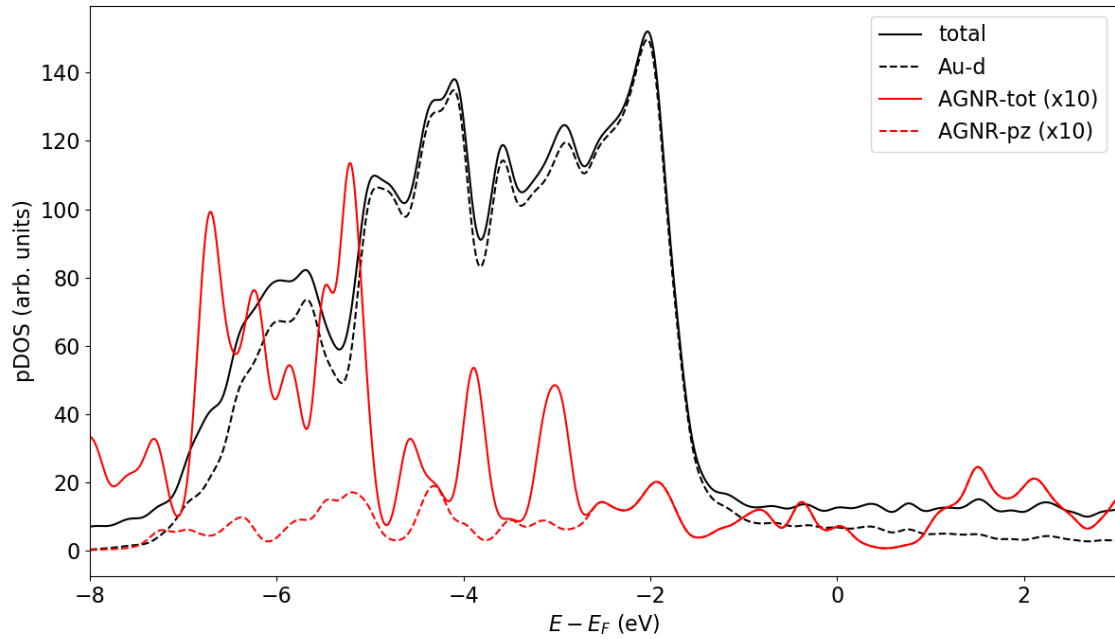


Figure 36: The DOS of 9-AGNR on Au(111) is shown. It is smeared with 0.1 eV and a k-mesh of $8 \times 4 \times 3$ was used.

When comparing the DOS for the freestanding and adsorbed 9-AGNR in Fig. 35 and 36, respectively, one can see that the former is shifted by about 0.1 eV to the left. This energy shift is also very clearly visible when comparing momentum maps of the two systems with each other. The binding energies -1.0 eV and -1.9 eV of 9-AGNR on Au(111) were identified as binding energies of interest for a k-map, because at these binding energies there is a peak in the DOS.

Note that for the case of 9-AGNR/Au(111), it is not confirmed by a calculation with a denser k-mesh that the DOS in Fig. 36 is converged with respect to the k-mesh, because the used k-mesh is the maximum of what is realistically possible with the available computational resources. However,

it is rational to assume that the DOS in Fig. 36 is in fact reasonably converged, considering the analogy to 7-AGNR on Au(111) in Fig. 17. The DOS in Fig. 35 is converged with respect to the k-mesh, since calculations with a $30 \times 6 \times 8$ and a $45 \times 9 \times 12$ k-mesh yield the same DOS.

4.4.2 Photoemission Band Maps

Band maps of 9-AGNR are presented with different E_b - and $k_{||}$ -ranges. Additionally, a comparison with experiment is shown.

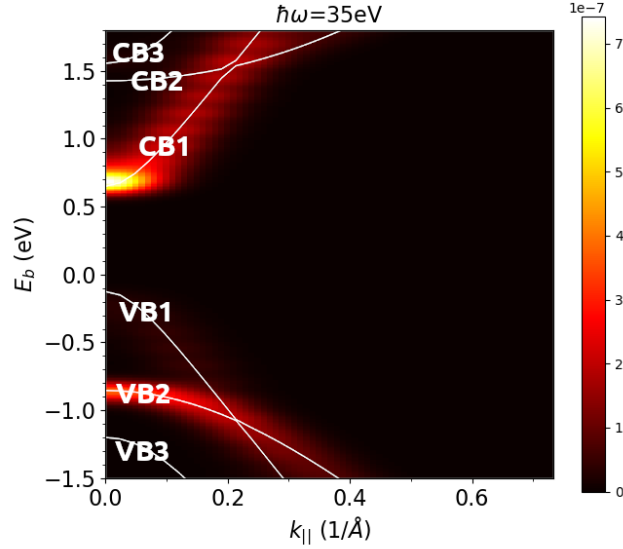


Figure 37: A simulated band map of freestanding 9-AGNR parallel to the armchair direction is shown. The colors specify the photoemission intensity in arbitrary units. As an overlay, the white lines are the band structure of Fig. 34. The $k_{||}$ range is the same as in Fig. 34.

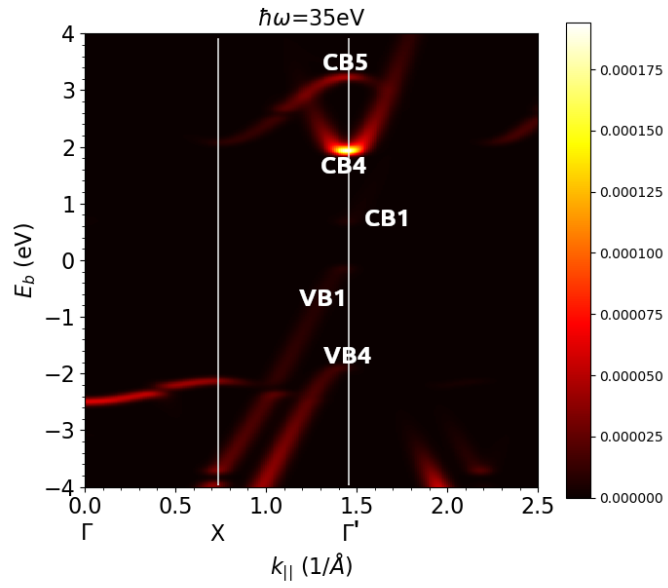
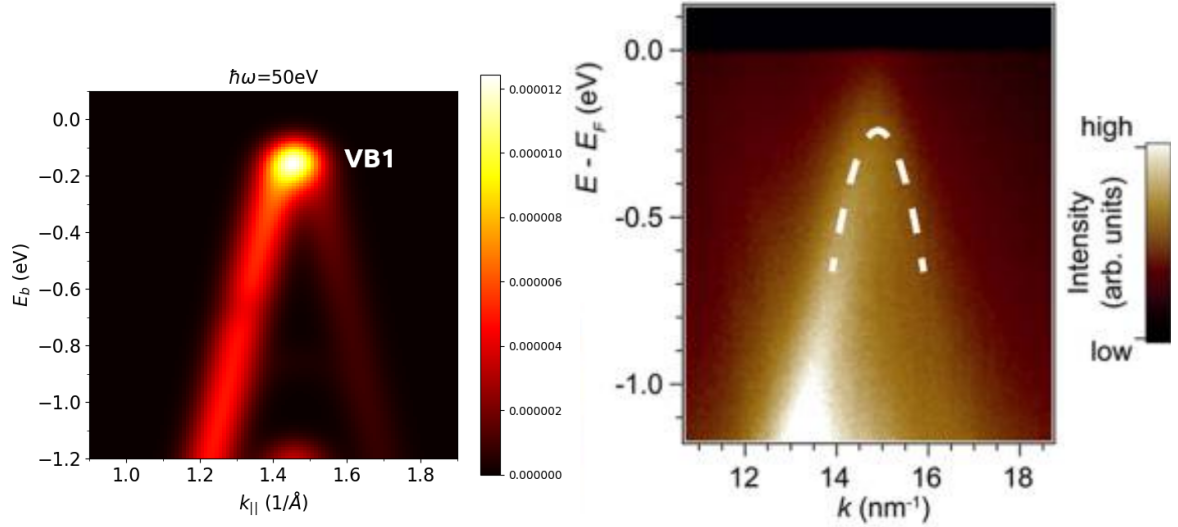
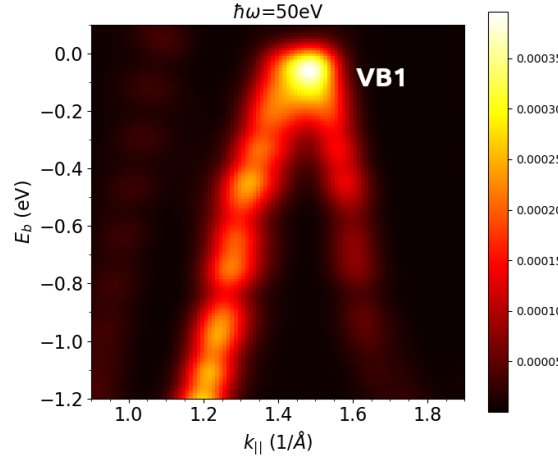


Figure 38: A simulated band map of freestanding 9-AGNR parallel to the armchair direction is shown. The difference to Fig. 37 is, that the axis span a wider range. The emissions around the Γ -point, that can be seen in Fig. 37, are not visible here due to their low photoemission intensity.



(a) Simulation of freestanding 9-AGNR

(b) Experiment by Talirz et al. [5]



(c) Simulation of 9-AGNR on Au(111)

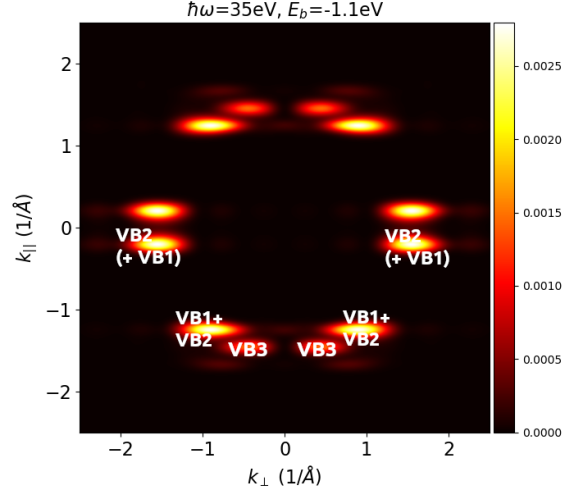
Figure 39: Simulated band maps of freestanding 9-AGNR and 9-AGNR on Au(111) are compared to an experiment of 9-AGNR on Au(788) from the literature [5]. The observed emissions arise from the topmost valence band (VB_1). The artificial smearing in Figs. 39a and 39c is $\sigma_E = 0.05$ eV and $\sigma_k = 0.05 \text{ \AA}^{-1}$. The used k-meshes are $128 \times 5 \times 5$ and $32 \times 1 \times 1$ for Fig. 39a and Fig. 39c respectively. The white dashed line in Fig. 39b "shows the best [parabolic] fit to the VB near $k = \frac{2\pi}{a} = 14.8 \text{ nm}^{-1}$ " [5]. The photon energy $\hbar\omega$ was chosen to be the same as in the experiment, namely 50 eV.

Good agreement between simulation and experiment can be seen in Fig. 39 and the observed emissions can be identified by the topmost valence band of 9-AGNR denoted as VB_1 . Note that the VB_1 in Fig. 39c is shifted upwards by 0.1 eV compared to Fig. 39a. This shift is in agreement with the shift in the DOS, that is presented in Sec. 4.4.1.

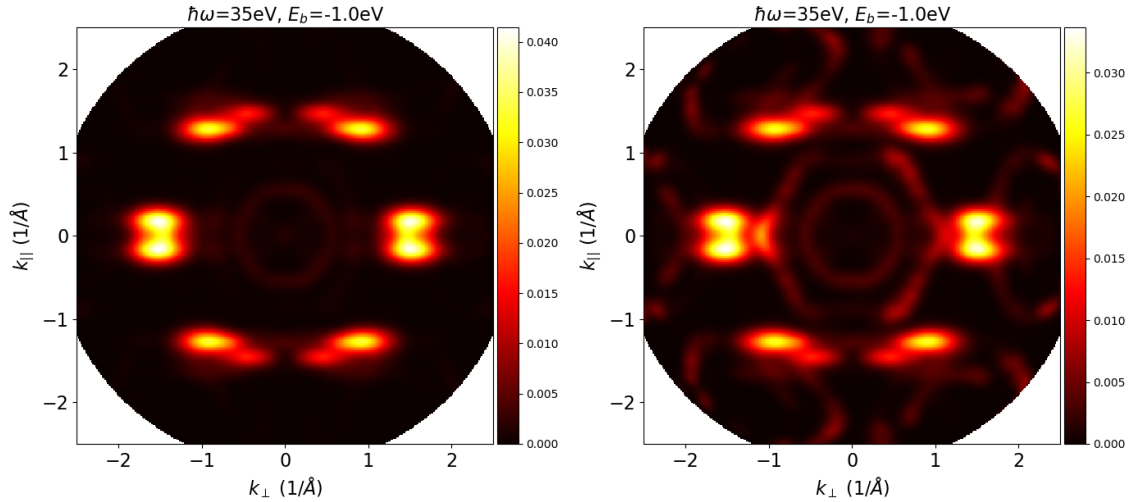
4.4.3 Photoemission Momentum Maps

In analogy to Sec. 4.3.3.4, the momentum maps of freestanding 9-AGNR, 9-AGNR on Au(111) with strong damping and 9-AGNR on Au(111) with weak damping are presented here. When speaking of "strong damping", the damping strength was set to $\gamma = 0.5 \text{ \AA}^{-1}$ and the start of it was set in the middle of the AGNR and the topmost gold layer. For the weaker damping, $\gamma = 0.1 \text{ \AA}^{-1}$ and it starts at the topmost gold layer. In all momentum maps in this section, the

artificially introduced smearing amounts to 0.05 \AA^{-1} for the freestanding 9-AGNR and 0.08 \AA^{-1} for 9-AGNR on Au(111). The binding energies of relevance are identified in Sec. 4.4.1. Unfortunately, experimental momentum maps for comparison are not available in the literature.

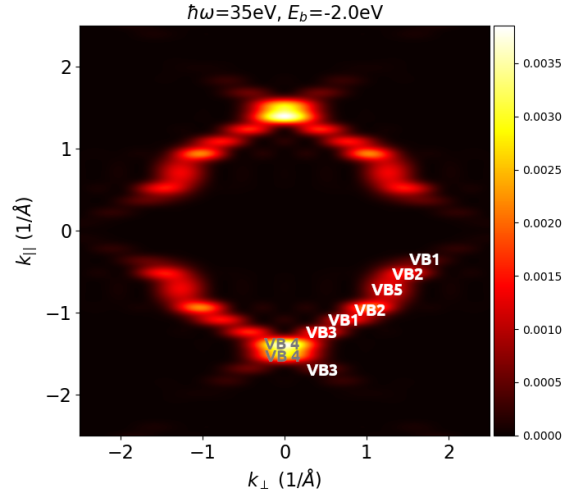


(a) Simulation of freestanding 9-AGNR

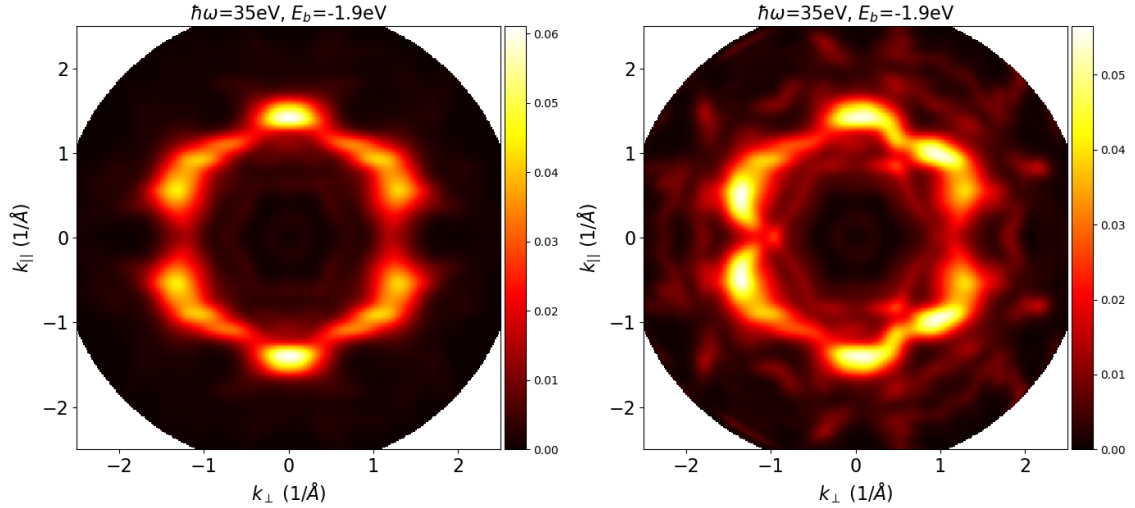


(b) Simulation of 9-AGNR on gold with strong damp- (c) Simulation of 9-AGNR on gold with weak damp-
ing ing

Figure 40: ARPES momentum maps of 9-AGNR are compared with each other analogous to the case of 7-AGNR in Sec. 4.3.3. Assigning the features to specific valence bands (VB) is difficult in this case, because the resolution of the momentum map is lower than the distance between VB_1 and VB_2 in the $k_{||}$ -direction (as can be seen in Fig. 37 at $E_b = -1.1 \text{ eV}$). The notation " $VB_2 (+VB_1)$ " here means that the feature mainly stems from the VB_2 , and additionally has a very small contribution from the VB_1 . The feature denoted by " $VB_1 + VB_2$ " stems in equal proportions from the VB_1 and VB_2 . The VB_1 contributes to the feature between $k_{\perp} = 0.5$ and 0.8 \AA^{-1} ; then, between $k_{\perp} = 0.8$ and 1.2 \AA^{-1} , the feature stems from the VB_2 . For the labeling of the bands, band repulsion is ignored in the sense that the bands in Fig. 34 are continued as if no band repulsion would be present.



(a) Simulation of freestanding 9-AGNR



(b) Simulation of 9-AGNR on gold with strong damping (c) Simulation of 9-AGNR on gold with weak damping

Figure 41: ARPES momentum maps of 9-AGNR are compared with each other. Similarly to 7-AGNR, one can see an asymmetry around the central vertical axis in Fig. 41c. According to the argument in Sec. 4.3.3.1, this asymmetry must come from the gold or the interaction between gold and AGNR. The label "VB₄" is grey simply to make it better visible. It is difficult to distinguish VB₁, VB₂, VB₃ and VB₅ from each other, therefore an erroneous assignment might have occurred.

4.5 Electronic Structure of 13-AGNR

In analogy to Sec. 4.3 and 4.4, here the electronic structure of 13-AGNR is investigated.

4.5.1 Band Structure and DOS

The calculated band gap is 0.87 eV wide, which is in agreement with a DFT LDA result from Zhu et al., who calculated it to be 0.89 eV [50].

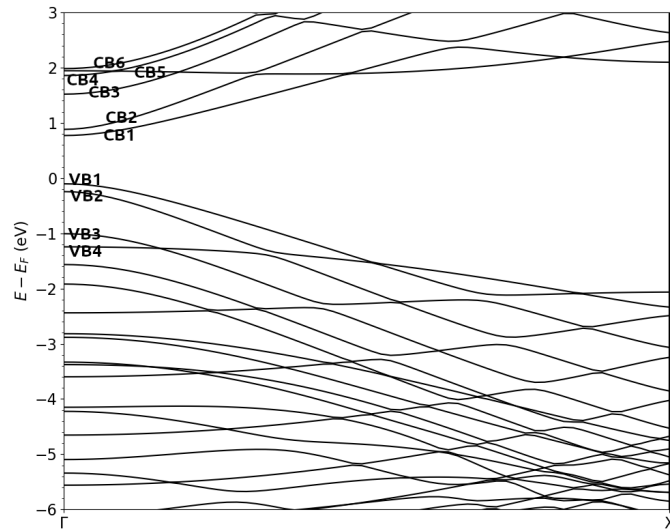


Figure 42: The band structure of freestanding 13-AGNR parallel to the armchair direction is shown. It is calculated using a $128 \times 8 \times 8$ k-mesh. The calculated GGA band gap is 0.87 eV wide.

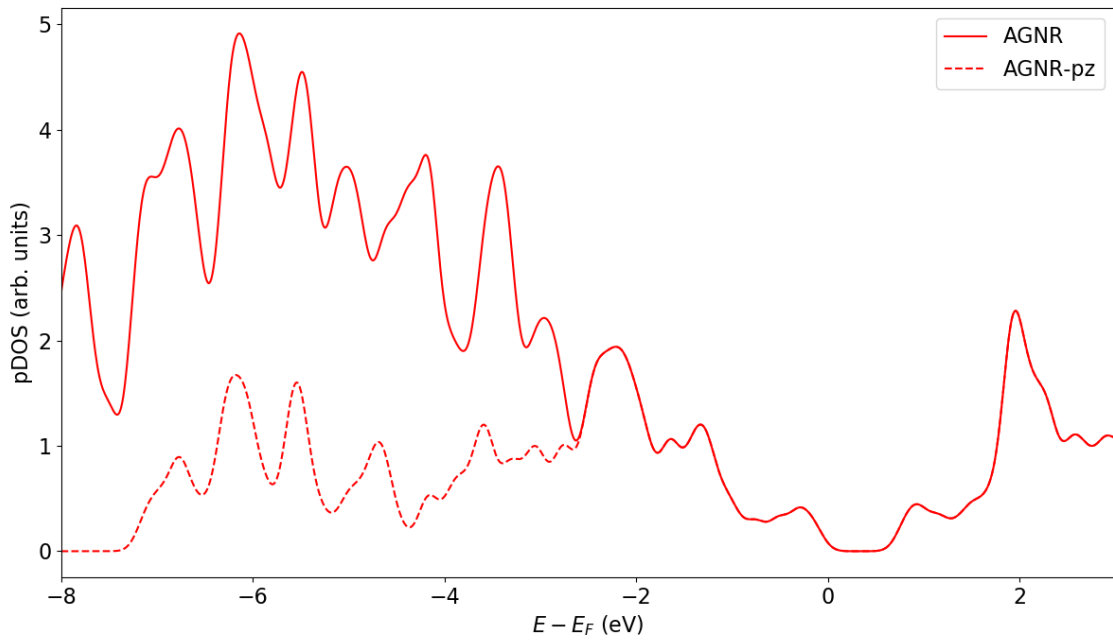


Figure 43: The DOS of the freestanding 13-AGNR is shown. It is smeared with 0.1 eV and a k-mesh of $30 \times 5 \times 8$ was used.

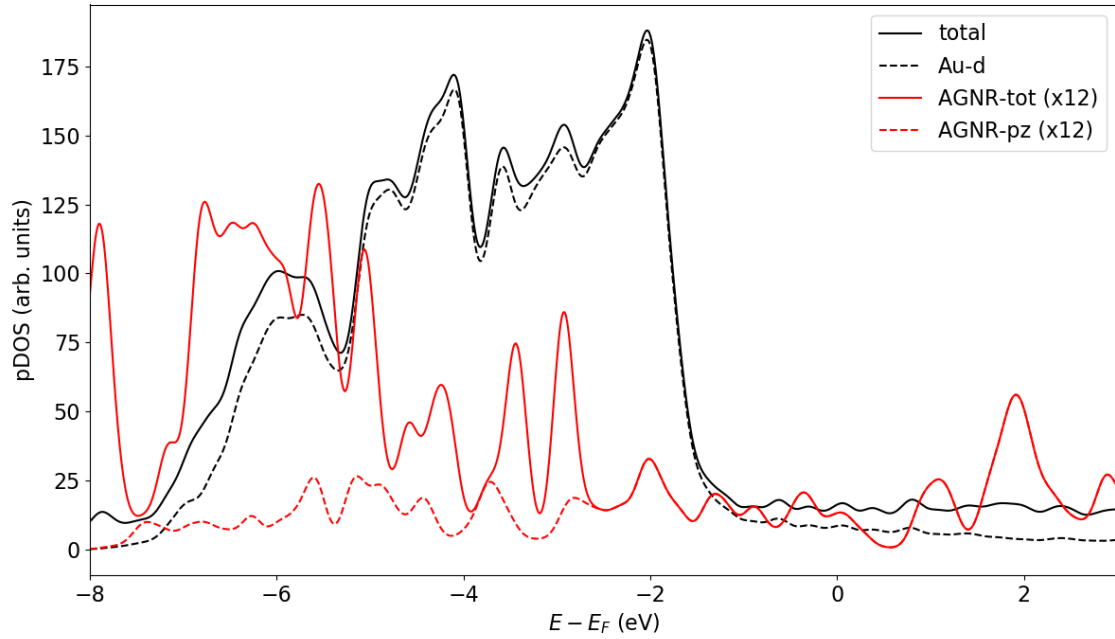


Figure 44: The DOS of 13-AGNR on Au(111) is shown. It is smeared with 0.1 eV and a k-mesh of $9 \times 3 \times 2$ was used.

In the same manner as for 7- and 9-AGNR, binding energies for a k-map are chosen. For 13-AGNR on Au(111), the binding energies -1.0 eV, -1.3 eV, -1.6 eV and -1.9 eV are selected. Contrary to the case of 7- and 9-AGNR, the DOS is not significantly shifted on the vertical axis between freestanding 13-AGNR (Fig. 43) and 13-AGNR on Au(111) (Fig. 44). This is consistent with the momentum maps, where there is also no shift in binding energy observable. The shift in binding energy seems to follow no apparent rule, when it is compared between differently sized AGNRs. To recap, the DOS of freestanding 7-AGNR is shifted by 0.4 eV to the right compared to 7-AGNR on Au(111). In the case of freestanding 9-AGNR, it is shifted by 0.1 eV to the left (not to the right!). Here, in the case of 13-AGNR, it is shifted less than could be observed, i.e. less than about 0.05 eV.

The ionization potential is the difference between the top of the valence band and the vacuum level. It is 5.0 eV, 4.7 eV and 4.7 eV for 7-, 9- and 13-AGNR on Au(111), respectively. Within the uncertainty of ± 0.1 eV it is in line with the trend of the shifts, which are 0.4 eV, -0.1 eV and 0.0 eV for 7-, 9- and 13-AGNR, respectively.

4.5.2 Photoemission Band Maps

A photoemission band map of 13-AGNR overlain by the band structure can be seen in Fig. 45.

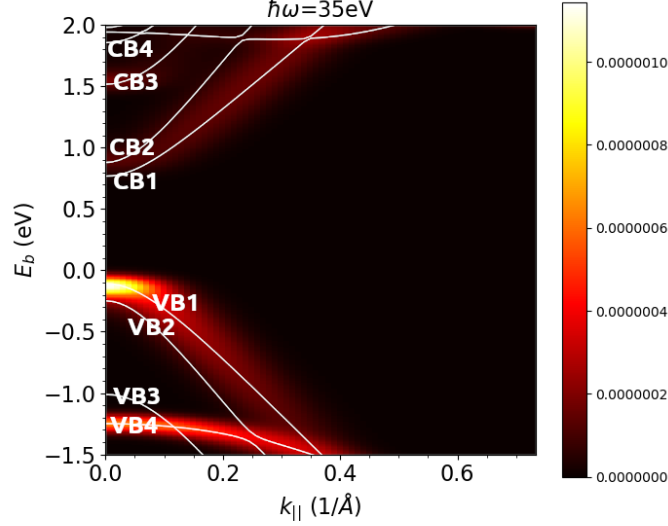
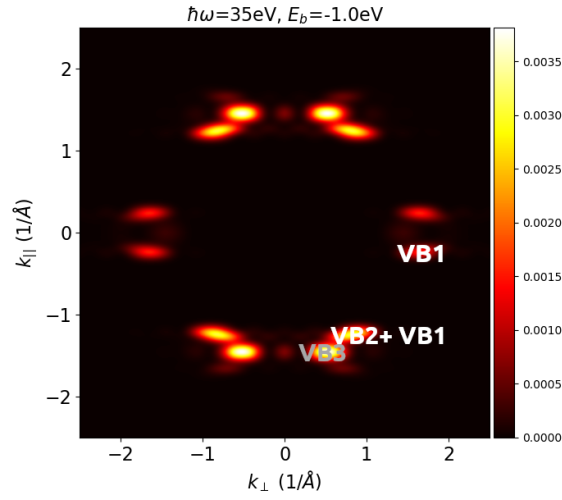


Figure 45: A simulated band map of freestanding 13-AGNR parallel to the armchair direction is shown. The colors specify the photoemission intensity. As an overlay, the white lines are the band structure of Fig. 42. The k_{\parallel} range is the same as in Fig. 42.

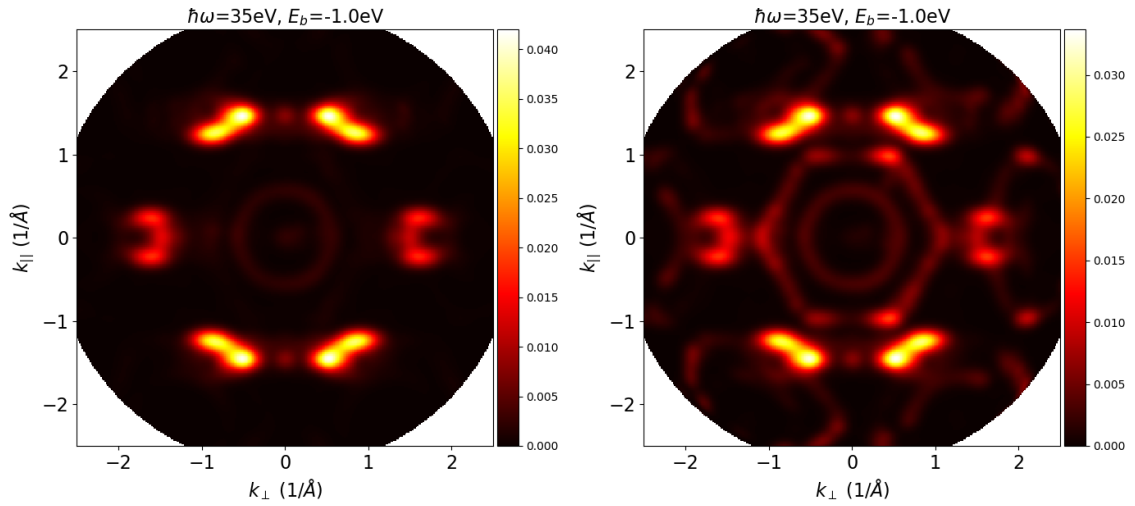
4.5.3 Photoemission Momentum Maps

Momentum maps at the binding energies -1.0 eV, -1.3 eV, -1.6 eV and -1.9 eV are shown in Figs. 46-49, respectively. In the following, the momentum maps of 13-AGNR on gold are depicted with strong and weak damping respectively. When speaking of "strong damping", the damping strength was set to $\gamma = 0.5 \text{ \AA}^{-1}$ and the start of it was set in the middle of the AGNR and the topmost gold layer. For the weaker damping, $\gamma = 0.1 \text{ \AA}^{-1}$ and it starts at the topmost gold layer. The artificially introduced smearing amounts to 0.05 \AA^{-1} for the freestanding 13-AGNR and 0.08 \AA^{-1} for 13-AGNR on gold.

Unfortunately, no experimental data is available for comparison. So the simulated momentum maps shown in Figs. 46-49 are compiled here for later reference. Overall it can be seen that the number of emission features is increased compared to 7- and 13-AGNR. Moreover the k_{\perp} -width of all emission features is further reduced compared to 7- and 9-AGNR owing to the increased width of the ribbon in real space. This effect will be analyzed in more detail in Sec. 4.6.3.

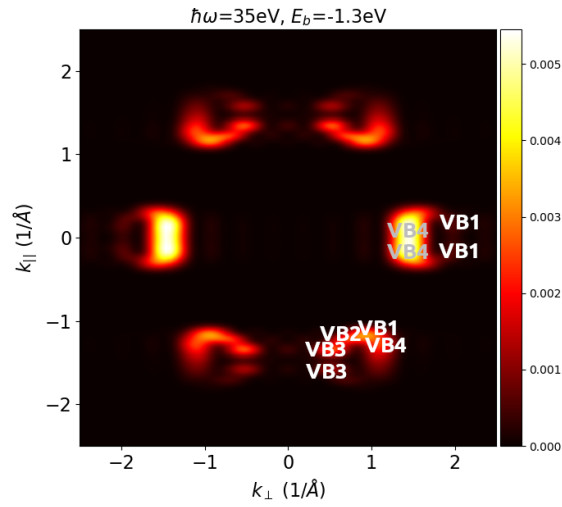


(a) Simulation of freestanding 13-AGNR

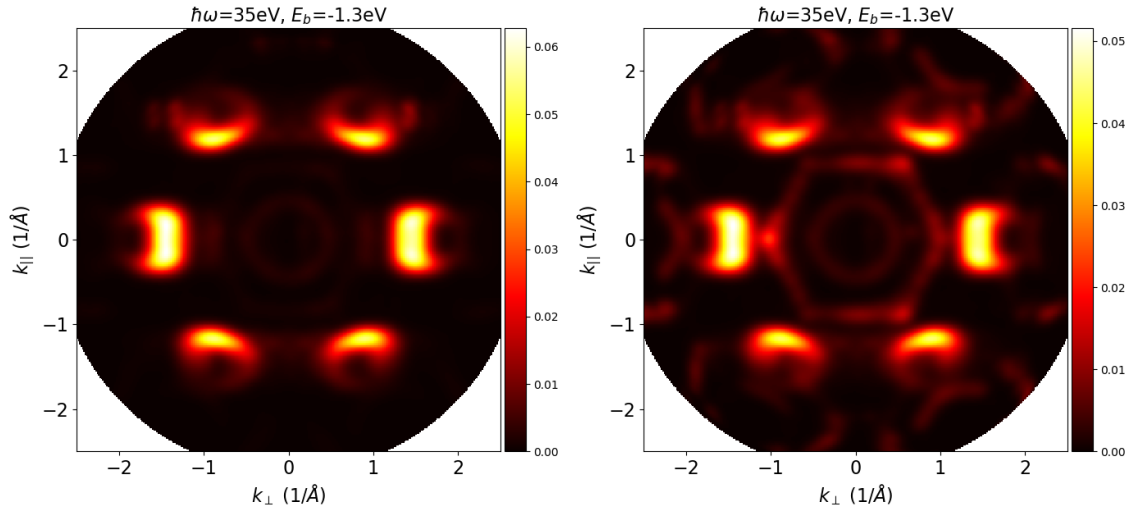


(b) Simulation of 13-AGNR on gold with strong damping (c) Simulation of 13-AGNR on gold with weak damping

Figure 46: ARPES momentum maps of 13-AGNR are compared with each other. The feature labelled " $VB_2 + VB_1$ " comes from both valence bands. The former contributes between $k_{\perp} = 0.6$ and 0.9 \AA^{-1} ; the latter contributes between $k_{\perp} = 0.9$ and 1.1 \AA^{-1} .

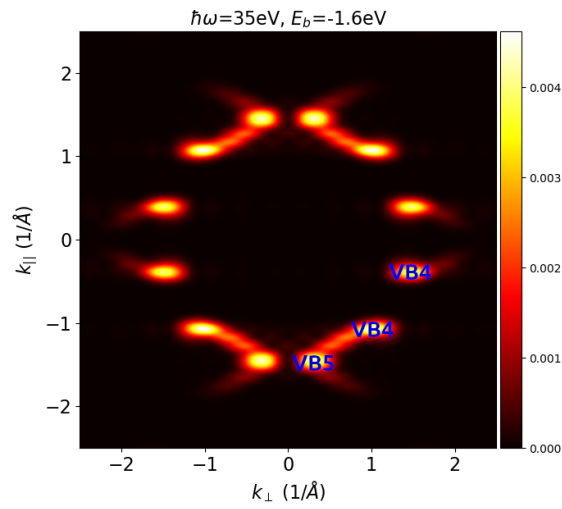


(a) Simulation of freestanding 13-AGNR

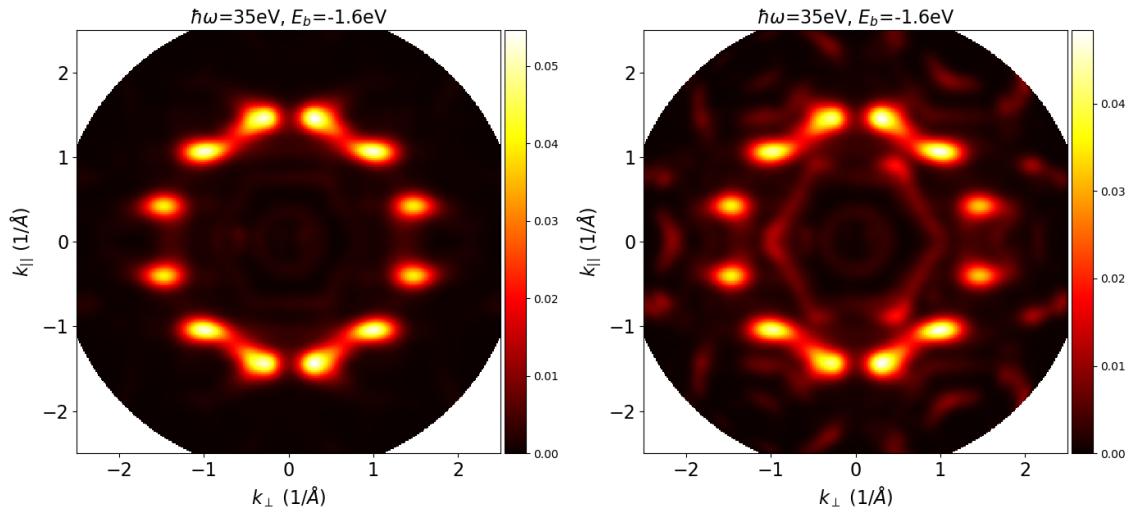


(b) Simulation of 13-AGNR on gold with strong damping (c) Simulation of 13-AGNR on gold with weak damping

Figure 47: ARPES momentum maps of 13-AGNR are compared with each other. For the feature at $(\pm 1, \pm 1.3)$, it cannot be clearly distinguished, which portions of the feature come from which valence band.

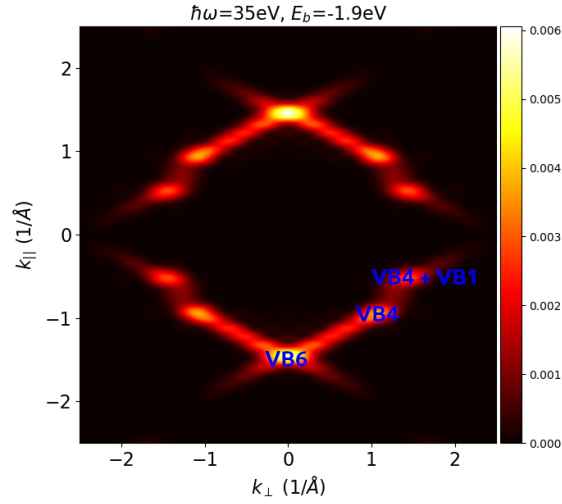


(a) Simulation of freestanding 13-AGNR

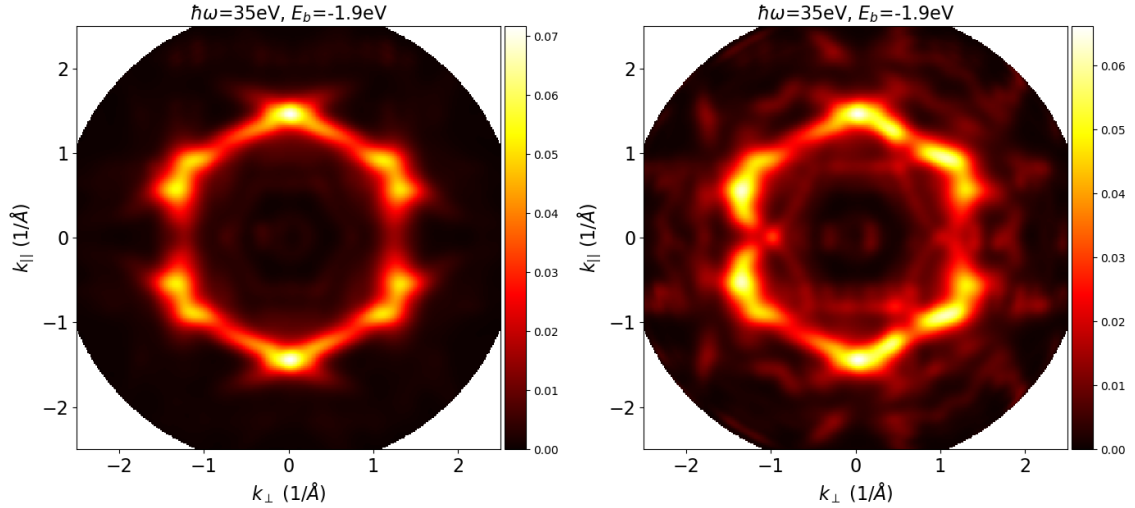


(b) Simulation of 13-AGNR on gold with strong damping (c) Simulation of 13-AGNR on gold with weak damping

Figure 48: ARPES momentum maps of 13-AGNR are compared with each other.



(a) Simulation of freestanding 13-AGNR



(b) Simulation of 13-AGNR on gold with strong damping (c) Simulation of 13-AGNR on gold with weak damping

Figure 49: ARPES momentum maps of 13-AGNR are compared with each other.

4.6 Comparison between 7-, 9- and 13-AGNR

In this section, various features of 7-, 9- and 13-AGNR are compared with each other, thereby it is investigated how the width of the nanoribbon affects them. First, band gaps, which were calculated with different methods, are presented and analyzed. Secondly, the charge density difference due to the interaction of the AGNR with the Au(111) surface is calculated. Thirdly, the influence, that the nanoribbons width has on the momentum maps, is examined.

4.6.1 Band Gaps

The band gaps of the freestanding 7-, 9- and 13-AGNR are already mentioned above, but are again given in Table 2. They are compared with the band gaps of the AGNRs on Au(111) from this work and band gaps from the literature. In this work, the band gaps of AGNRs on Au(111) are obtained from the band maps (Secs. 4.3.2, 4.4.2 and 4.5.2). Therefore, they have a larger numerical uncertainty (in the order of ± 0.1 eV) than the band gaps of freestanding AGNRs, which can be obtained from the band structure with an uncertainty in the order of ± 0.01 eV.

Table 2: Band gaps of AGNRs are tabulated. The unit of energy is eV.

Method Source	Freestanding AGNR DFT GGA This work	AGNR on Au(111) DFT GGA This work	Freestanding AGNR DFT LDA Zhu et al. [50]	AGNR on Au(111) Experiment [6, 57, 58, 5, 59]
7-AGNR	1.61	1.6	1.59	2.6 [6], 2.3 [57], 2.37 ± 0.06 [58]
9-AGNR	0.78	0.8	0.79	1.4 [5], 1.35 ± 0.07 [59]
13-AGNR	0.87	0.9	0.89	1.4 [6]

The experimental values have been measured in the following way:

- Chen et al. [6]: Scanning tunneling spectroscopy (STS) was used to determine the band gaps.
- Ruffieux et al. [57]: Scanning tunneling spectroscopy (STS) was used to measure the band gap. Additionally, ARPES was used to determine the effective mass and other quantities. The onset of the valence band measured by ARPES agrees with the valence band observed in STS.
- Sode et al. [58]: STS was used.
- Talirz et al. [5]: Fourier-transformed scanning tunneling spectroscopy (FT-STs) was used. Additionally, ARPES experiments and DFT simulations of the band structure were performed.
- Merino et al. [59]: STS was used.

In Table 2, one can see that the DFT results (columns 1, 2 and 3) agree with each other. The addition of the Au(111) surface does not change the band gap within the numerical uncertainty of ± 0.1 eV. DFT underestimates the band gap by about 40% and may thus be not the best theoretical approach to predict the band gap. Ruffieux et al. performed GW calculations including image charge (IC) corrections [57], which seem to predict a band gap that is closer to experiment.

4.6.2 Charge Density

Here, the electronic structure of AGNR on Au(111) is further discussed by analyzing the charge density differences upon adsorption of the nanoribbon on the surface. In particular, plots of the plane-averaged charge densities of the AGNRs on the "bond hollow" adsorption site were calculated and can be seen in Figs. 50, 51a and 51b. Three DFT simulations for each of the AGNRs, amounting to nine simulations in total, were necessary to obtain these plots. One was made for the combined relaxed system (AGNR on gold), one for the AGNR and one for the gold separately. In the latter two cases, the positions of the atoms were not relaxed, rather they were kept the same as in the combined system. This allows one to calculate the difference in charge density due to the interaction of the AGNR with the gold surface, which is defined as

$$\Delta\rho = \rho_{total} - (\rho_{Au(111)} + \rho_{AGNR}) \quad (39)$$

In the absence of a net charge transfer, this charge density difference is induced via Pauli-repulsion and is known as the push-back effect. This effect causes the gold's spill-out charge to be pushed back into the gold [60]. To nullify the dipole moment induced by this charge density difference, an artificial dipole layer was introduced in all calculations, as mentioned in Sec. 3. The chosen k-meshes are $6 \times 3 \times 1$, $6 \times 2 \times 1$ and $6 \times 2 \times 1$ for 7-, 9- and 13-AGNR respectively.

One can see that the chosen vacuum is sufficient, since the charge density ρ is approximately zero for a long distance. The charge densities of 9-AGNR and 13-AGNR on gold look very similar to the one for 7-AGNR, yet they are presented here for the sake of completeness. A difference is of course the number of electrons, which is noted on the left y-axis. Another distinction is that the charge density difference $\Delta\rho$ is multiplied by 300 for 7-AGNR, while it is multiplied by 500 for 9-AGNR and 13-AGNR. This was done to fit it in the plot and has no physical reason.

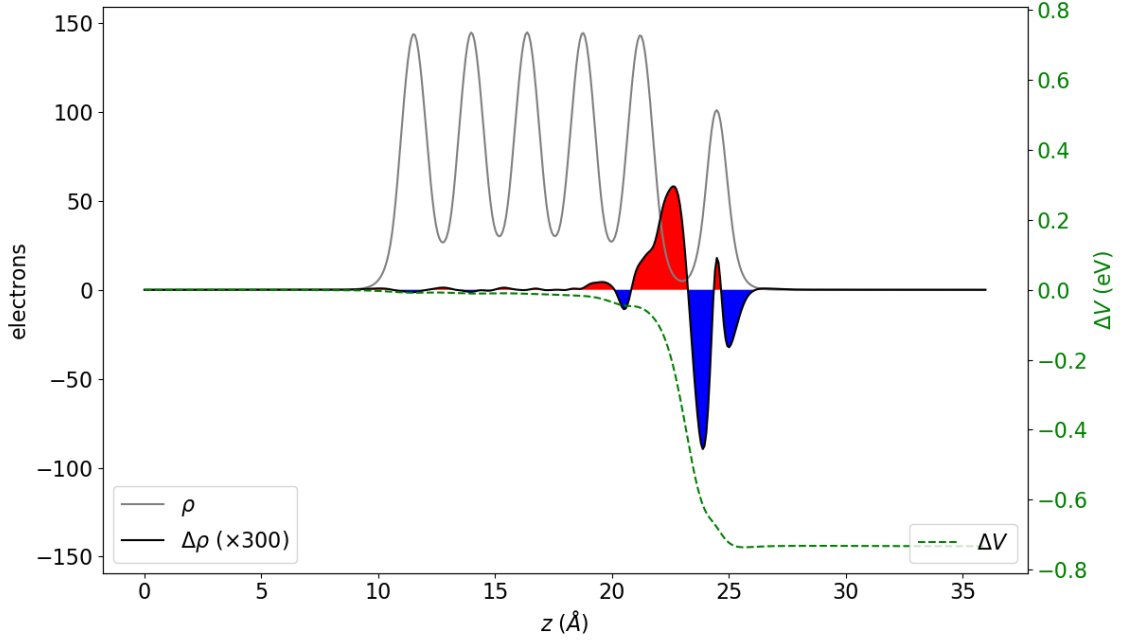


Figure 50: The following quantities are plotted: the charge density ρ of 7-AGNR on Au(111), the difference in charge density compared to 7-AGNR and Au(111) on their own $\Delta\rho$ and the electric potential difference ΔV of 7-AGNR on Au(111). Starting from the left one can see five gray peaks in the charge density ρ , which correspond to the five gold layers. Followed by it there is one lower peak on the right corresponding to 7-AGNR. Keeping in mind the periodic boundary conditions, a jump in the potential (green dashed line) can be seen between the maximum z -value at around $z = 36$ and $z = 0$. This jump of -0.67 eV corresponds to the artificially introduced dipole layer in the spirit of Neugebauer and Scheffler [37], as mentioned in Sec. 3. The work function of gold, which is 4.9 eV without 7-AGNR on top, is reduced by this value to 4.23 eV.

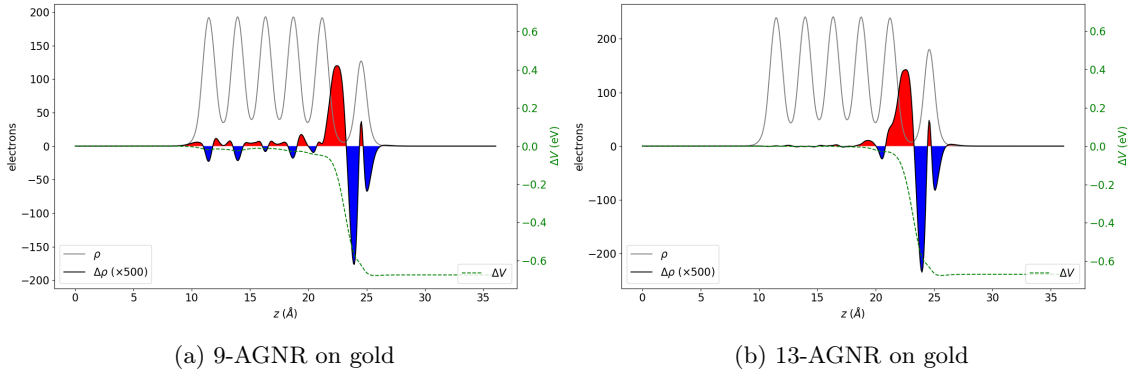
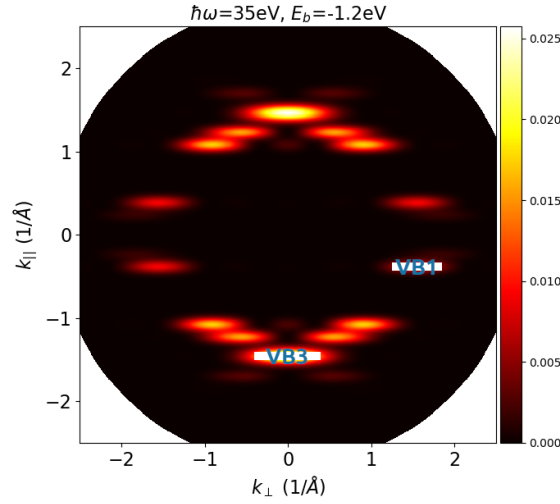


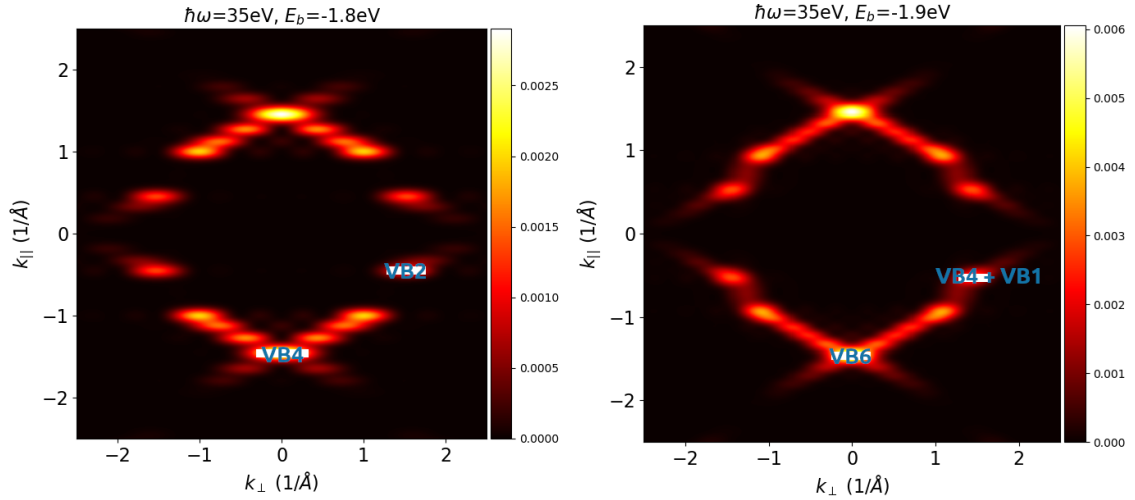
Figure 51: The charge densities of 9-AGNR and 13-AGNR on Au(111) are depicted in analogy to Fig. 50. The jump in ΔV is -0.63 eV for 9-AGNR on Au(111) and -0.64 eV for 13-AGNR on Au(111).

4.6.3 Momentum Maps of freestanding 7-, 9- and 13-AGNR

In this section, the momentum maps of freestanding 7-, 9- and 13-AGNR are compared among each other.



(a) Simulation of freestanding 7-AGNR



(b) Simulation of freestanding 9-AGNR

(c) Simulation of freestanding 13-AGNR

Figure 52: ARPES momentum maps of freestanding 7-, 9- and 13-AGNR are compared with each other. They are aligned in terms of binding energy in the following way: The binding energy, at which the strong feature at $(0, \pm 1.5)$ emerges, is identified for all AGNRs and then 0.1 eV are subtracted from that binding energy to make this feature more visible. The white boxes show the full width at half maximum, that is plotted in Fig. 53.

Representative for all binding energies, one comparison was made in Fig. 52. It can be generally said, that the features look somewhat similar. A difference is that the wider the ribbon, the more features are visible. For example there are two horizontal lines around $(k_{\perp}, k_{\parallel}) = (\pm 0.9, \pm 1.2) \text{ \AA}^{-1}$ for 7-AGNR, while there are three for 9-AGNR and even more for 13-AGNR.

Looking at Fig. 52, it is immediately apparent that features become thinner in the k_{\perp} -direction, the wider the AGNR is. In order to put this observation into numbers, the features at $(k_{\perp}, k_{\parallel}) = (0, \pm 1.5) \text{ \AA}^{-1}$ and $(k_{\perp}, k_{\parallel}) = (\pm 1.6, \pm 0.4) \text{ \AA}^{-1}$ were measured along the k_{\perp} -direction. To ensure a precise measurement, the program kMap.py was used [61]. With this program, horizontal line plots of the features were performed. In order to make a reproducible measurement of the features, a full width at half maximum was defined, i.e. the two points at which the photoemission intensity drops by 50% are defined to be the borders of the feature. The feature sizes, that were obtained in this way, are depicted in Fig. 53.

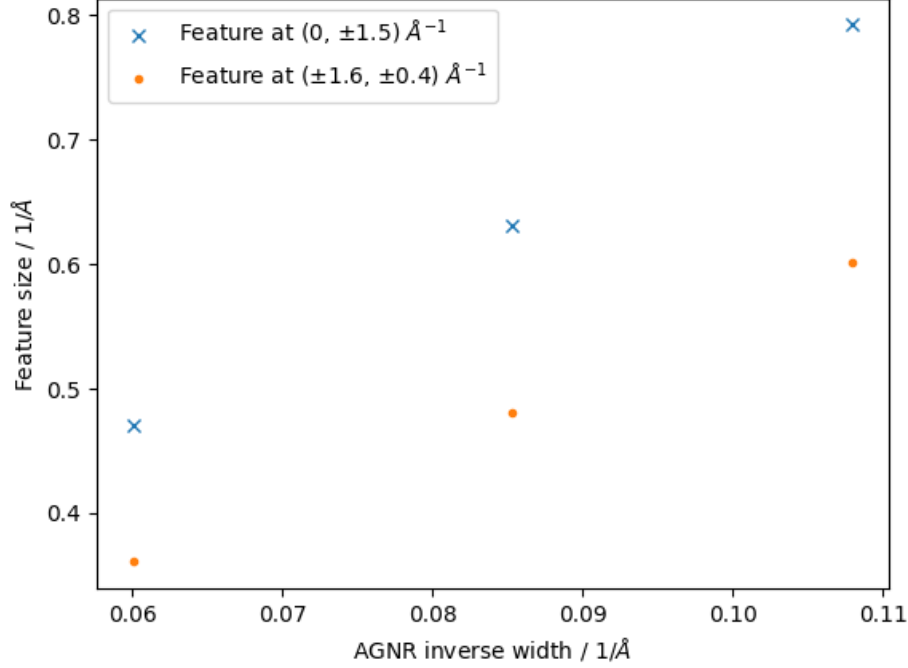


Figure 53: The horizontal widths of the features at $(k_{\perp}, k_{\parallel}) = (0, \pm 1.5) \text{ \AA}^{-1}$ and $(k_{\perp}, k_{\parallel}) = (\pm 1.6, \pm 0.4) \text{ \AA}^{-1}$ in Fig. 52 are compared with each other. The "feature size" is here defined to be the horizontal full width at half maximum of the feature. The x-axis is the inverse width of the nanoribbons, measured from one hydrogen atom to another. It is $\frac{1}{9.259} \text{ \AA}^{-1}$, $\frac{1}{11.721} \text{ \AA}^{-1}$ and $\frac{1}{16.659} \text{ \AA}^{-1}$ for 7-, 9- and 13-AGNR respectively.

In Fig. 53, one can clearly see a linear dependence of the feature size on the inverse width of the AGNR. One has to keep in mind, that the k-maps in Fig. 52 are smeared by $\sigma_k = 0.05 \text{ \AA}^{-1}$. Thus the measured feature sizes have an uncertainty in the order of 0.05 \AA^{-1} . Especially the small features, which are those of 13-AGNR, are effected by this smearing. Here, the smearing has the effect of enlarging them. This effect is most prominent in the feature at $(k_{\perp}, k_{\parallel}) = (\pm 1.6, \pm 0.4) \text{ \AA}^{-1}$ in Fig. 52c, since it is the smallest and almost circular due to the relatively strong smearing.

5 Conclusion

The aim of this thesis was to investigate the electronic structure of 7-, 9- and 13-armchair graphene nanoribbons (AGNR). In particular, it was of interest how the electronic structure changes when AGNRs adsorb on a Au(111) surface. A great portion of this work is dedicated to the simulation of angle-resolved photoemission spectroscopy (ARPES), which is typically performed on a Au(788) surface in the case of 7-AGNR. By applying density functional theory (DFT) simulations, new insight into the geometric and electronic structure of 7-, 9- and 13-AGNR adsorbed on a Au(111) surface has been gained.

First, the adsorption position of 7-, 9- and 13-AGNR on a Au(111) surface was investigated. The aim of this work was not to find a definitive adsorption position, rather a likely candidate was found and was compared to other high symmetry adsorption positions. The relative energies, adsorption heights and momentum maps of the different adsorption positions have been analyzed. The difference in energy is significant, insofar as it is higher than the thermal energy at room temperature. The DFT-D3 correction method of Grimme et al. [12] was used to account for Van der Waal interactions. The adsorption height of 7-AGNR on Au(111) was correctly predicted in comparison with experiment [39], thereby confirming the validity of the used method.

Next, the band structure and DOS of 7-, 9- and 13-AGNR have been calculated using DFT. The charge transfer between the AGNR and the Au(111) surface has been analyzed. The band gap was calculated, and it was found, that it does not change when the AGNR is adsorbed on the Au(111) surface. DFT simulations of the band gap from the literature [50] agree with the ones that were obtained in this work.

Finally, comparisons with ARPES experiments [54, 49, 5] have shown, that DFT in combination with the used ARPES formalism is well suited in describing the ARPES band maps and momentum maps. Simulated ARPES band maps and momentum maps of freestanding 7-AGNR and 7-AGNR on Au(111) were compared with each other, thereby the features and bands that come from the 7-AGNR and Au(111), respectively, were identified. This new insight was used to identify bands in band maps [54] and features in momentum maps [49]. The same comparison was performed for 9- and 13-AGNR on Au(111), however for these systems, no experimental data is available and simulations are compiled here for comparison with possible future experiments. Moreover, the momentum maps of freestanding 7-, 9- and 13-AGNR were compared with each other. It was found that the lateral feature size in the momentum maps depends linearly on the inverse width of the AGNR, i.e. the greater width of the 13-AGNR compared to 7-AGNR in real space causes the features of the former to be smaller in reciprocal space. It was investigated, how the different adsorption positions affect the momentum maps and it was found that they do not change the ARPES momentum maps qualitatively.

As an outlook to this thesis, future ARPES experiments of 9- and 13-AGNR would be desirable, since they could be compared to the momentum maps that were simulated in this thesis. The results of this work may be used as a guideline to understand the features that would be seen in such experiments. In the momentum maps of 7-AGNR, occasional differences between simulation and experiment suggest that there is room for further development of the DFT and ARPES simulations.

6 Acknowledgements

The computational results presented have been achieved using the computing facilities at the Karl-Franzens-Universität Graz and the Vienna Scientific Cluster (VSC). VESTA was used for the visualizations of atoms [62]. On a more personal side of things, I want to thank my supervisor Peter Puschnig for his guidance and illuminating explanations. Special thanks go out to Xiaosheng Yang for providing his experimental data and to Mathias Schwendt for stimulating discussions. Furthermore, I want to thank all my other colleagues, girlfriend, friends and family for their support.

References

- [1] Guillaume Vasseur, Mikel Abadia, Luis A Miccio, Jens Brede, Aran Garcia-Lekue, Dimas G de Oteyza, Celia Rogero, Jorge Lobo-Checa, and J Enrique Ortega. π band dispersion along conjugated organic nanowires synthesized on a metal oxide semiconductor. *Journal of the American Chemical Society*, 138(17):5685–5692, 2016.
- [2] Amina Kimouche, Mikko M Ervasti, Robert Drost, Simo Halonen, Ari Harju, Pekka M Joensuu, Jani Sainio, and Peter Liljeroth. Ultra-narrow metallic armchair graphene nanoribbons. *Nature Communications*, 6:10177, 2015.
- [3] Haiming Zhang, Haiping Lin, Kewei Sun, Long Chen, Yulian Zagranyski, Nabi Aghdassi, Steffen Duhm, Qing Li, Dingyong Zhong, Youyong Li, et al. On-surface synthesis of rylene-type graphene nanoribbons. *Journal of the American Chemical Society*, 137(12):4022–4025, 2015.
- [4] Han Huang, Dacheng Wei, Jiatao Sun, Swee Liang Wong, Yuan Ping Feng, AH Castro Neto, and Andrew Thye Shen Wee. Spatially resolved electronic structures of atomically precise armchair graphene nanoribbons. *Scientific Reports*, 2:983, 2012.
- [5] Leopold Talirz, Hajo Söde, Tim Dumslaff, Shiyong Wang, Juan Ramon Sanchez-Valencia, Jia Liu, Prashant Shinde, Carlo A Pignedoli, Liangbo Liang, Vincent Meunier, et al. On-surface synthesis and characterization of 9-atom wide armchair graphene nanoribbons. *ACS Nano*, 11(2):1380–1388, 2017.
- [6] Yen-Chia Chen, Dimas G De Oteyza, Zahra Pedramrazi, Chen Chen, Felix R Fischer, and Michael F Crommie. Tuning the band gap of graphene nanoribbons synthesized from molecular precursors. *ACS Nano*, 7(7):6123–6128, 2013.
- [7] Okan Deniz, Carlos Sánchez-Sánchez, Tim Dumslaff, Xinliang Feng, Akimitsu Narita, Klaus Müllen, Neerav Kharche, Vincent Meunier, Roman Fasel, and Pascal Ruffieux. Revealing the electronic structure of silicon intercalated armchair graphene nanoribbons by scanning tunneling spectroscopy. *Nano Letters*, 17(4):2197–2203, 2017.
- [8] Jinming Cai, Pascal Ruffieux, Rached Jaafar, Marco Bieri, Thomas Braun, Stephan Blankenburg, Matthias Muoth, Ari P Seitsonen, Moussa Saleh, Xinliang Feng, et al. Atomically precise bottom-up fabrication of graphene nanoribbons. *Nature*, 466(7305):470–473, 2010.
- [9] Juan Pablo Llinas, Andrew Fairbrother, Gabriela Borin Barin, Wu Shi, Kyunghoon Lee, Shuang Wu, Byung Yong Choi, Rohit Braganza, Jordan Lear, Nicholas Kau, et al. Short-channel field-effect transistors with 9-atom and 13-atom wide graphene nanoribbons. *Nature Communications*, 8(1):1–6, 2017.
- [10] Vikram Passi, Amit Gahoi, Boris V Senkovskiy, Danny Haberer, Felix R Fischer, Alexander Grüneis, and Max C Lemme. Field-effect transistors based on networks of highly aligned, chemically synthesized $n=7$ armchair graphene nanoribbons. *ACS Applied Materials & Interfaces*, 10(12):9900–9903, 2018.
- [11] Steffen Linden, Dingyong Zhong, A Timmer, N Aghdassi, JH Franke, H Zhang, Xinliang Feng, Klaus Müllen, H Fuchs, L Chi, et al. Electronic structure of spatially aligned graphene nanoribbons on au (788). *Physical Review Letters*, 108(21):216801, 2012.
- [12] Stefan Grimme, Jens Antony, Stephan Ehrlich, and Helge Krieg. A consistent and accurate ab initio parametrization of density functional dispersion correction (dft-d) for the 94 elements h-pu. *The Journal of Chemical Physics*, 132(15):154104, 2010.
- [13] Georg Kresse and Jürgen Furthmüller. Efficient iterative schemes for ab initio total-energy calculations using a plane-wave basis set. *Physical Review B*, 54(16):11169, 1996.
- [14] Pierre Hohenberg and Walter Kohn. Inhomogeneous electron gas. *Physical Review*, 136(3B):B864, 1964.
- [15] JF Janak. Proof that $\frac{\partial E}{\partial n_i} = \epsilon$ in density-functional theory. *Physical Review B*, 18(12):7165, 1978.

- [16] D. Sholl and J.A. Steckel. *Density Functional Theory: A Practical Introduction*. Wiley, 2009.
- [17] Peter E Blöchl. Projector augmented-wave method. *Physical Review B*, 50(24):17953, 1994.
- [18] Georg Kresse and Daniel Joubert. From ultrasoft pseudopotentials to the projector augmented-wave method. *Physical Review B*, 59(3):1758, 1999.
- [19] David Vanderbilt. Soft self-consistent pseudopotentials in a generalized eigenvalue formalism. *Physical Review B*, 41(11):7892, 1990.
- [20] G Kresse and J Hafner. Norm-conserving and ultrasoft pseudopotentials for first-row and transition elements. *Journal of Physics: Condensed Matter*, 6(40):8245, 1994.
- [21] Jan Hermann, Robert A DiStasio Jr, and Alexandre Tkatchenko. First-principles models for van der waals interactions in molecules and materials: Concepts, theory, and applications. *Chemical Reviews*, 117(6):4714–4758, 2017.
- [22] Martin A Blood-Forsythe, Thomas Markovich, Robert A DiStasio, Roberto Car, and Alán Aspuru-Guzik. Analytical nuclear gradients for the range-separated many-body dispersion model of noncovalent interactions. *Chemical science*, 7(3):1712–1728, 2016.
- [23] John P. Perdew, Kieron Burke, and Matthias Ernzerhof. Generalized gradient approximation made simple. *Phys. Rev. Lett.*, 77:3865–3868, Oct 1996.
- [24] Wikipedia contributors. ARPES analyzer cross section. https://commons.wikimedia.org/wiki/File:ARPES_analyzer_cross_section.svg, 2020. Accessed: 2020-10-31.
- [25] Daniel Lüftner. *Orbital tomography: Understanding photoemission of organic molecular films*. PhD thesis, 2015.
- [26] Stephan Hüfner. *Photoelectron spectroscopy: principles and applications*. Springer Science & Business Media, 2013.
- [27] Andrea Damascelli. Probing the electronic structure of complex systems by arpes. *Physica Scripta*, 2004(T109):61, 2004.
- [28] M Dauth, M Wiessner, V Feyer, A Schöll, P Puschnig, F Reinert, and S Kümmel. Angle resolved photoemission from organic semiconductors: orbital imaging beyond the molecular orbital interpretation. *New Journal of Physics*, 16(10):103005, 2014.
- [29] Ryan P Day, Berend Zwartsenberg, Ilya S Elfimov, and Andrea Damascelli. Computational framework chinook for angle-resolved photoemission spectroscopy. *npj Quantum Materials*, 4(1):1–10, 2019.
- [30] M Pl Seah and WA Dench. Quantitative electron spectroscopy of surfaces: A standard data base for electron inelastic mean free paths in solids. *Surface and interface analysis*, 1(1):2–11, 1979.
- [31] Simon Moser. An experimentalist’s guide to the matrix element in angle resolved photoemission. *Journal of Electron Spectroscopy and Related Phenomena*, 214:29–52, 2017.
- [32] Daniel Lüftner, Simon Weiß, Xiaosheng Yang, Philipp Hurdax, Vitaliy Feyer, Alexander Gottwald, Georg Koller, Serguei Soubatch, Peter Puschnig, Michael G. Ramsey, and F. Stefan Tautz. Understanding the photoemission distribution of strongly interacting two-dimensional overlayers. *Phys. Rev. B*, 96:125402, Sep 2017.
- [33] S Tanuma, CJ Powell, and DR Penn. Calculations of electron inelastic mean free paths. ix. data for 41 elemental solids over the 50 eV to 30 keV range. *Surface and interface analysis*, 43(3):689–713, 2011.
- [34] Dario Wolf Knebl. Shockley surface states from first principles. Master’s thesis, University of Graz, 2013.

- [35] Ask Hjorth Larsen, Jens Jørgen Mortensen, Jakob Blomqvist, Ivano E Castelli, Rune Christensen, Marcin Dułak, Jesper Friis, Michael N Groves, Bjørk Hammer, Cory Hargus, Eric D Hermes, Paul C Jennings, Peter Bjerre Jensen, James Kermode, John R Kitchin, Esben Leonhard Kolsbjerg, Joseph Kubal, Kristen Kaasbjerg, Steen Lysgaard, Jón Bergmann Maronsson, Tristan Maxson, Thomas Olsen, Lars Pastewka, Andrew Peterson, Carsten Rostgaard, Jakob Schiøtz, Ole Schütt, Mikkel Strange, Kristian S Thygesen, Tejs Vegge, Lasse Vilhelmsen, Michael Walter, Zhenhua Zeng, and Karsten W Jacobsen. The atomic simulation environment—a python library for working with atoms. *Journal of Physics: Condensed Matter*, 29(27):273002, 2017.
- [36] MPAT Methfessel and AT Paxton. High-precision sampling for brillouin-zone integration in metals. *Physical Review B*, 40(6):3616, 1989.
- [37] Jörg Neugebauer and Matthias Scheffler. Adsorbate-substrate and adsorbate-adsorbate interactions of na and k adlayers on al (111). *Physical Review B*, 46(24):16067, 1992.
- [38] Neil W Ashcroft, N David Mermin, et al. *Solid state physics*, volume 2005. holt, rinehart and winston, new york London, 1976.
- [39] S Weiß, D Gerbert, A Stein, AK Schenk, X Yang, C Brülke, R Kremring, S Feldmann, FC Bocquet, M Gille, et al. Dependence of the adsorption height of graphenelike adsorbates on their dimensionality. *Physical Review B*, 98(7):075410, 2018.
- [40] Benedikt P Klein, Juliana M Morbec, Markus Franke, Katharina K Greulich, Malte Sachs, Shayan Parhizkar, François C Bocquet, Martin Schmid, Samuel J Hall, Reinhard J Maurer, et al. Molecule–metal bond of alternant versus nonalternant aromatic systems on coinage metal surfaces: Naphthalene versus azulene on ag (111) and cu (111). *The Journal of Physical Chemistry C*, 123(48):29219–29230, 2019.
- [41] Axel D Becke and Erin R Johnson. A density-functional model of the dispersion interaction. *The Journal of Chemical Physics*, 123(15):154101, 2005.
- [42] Victor G Ruiz, Wei Liu, Egbert Zojer, Matthias Scheffler, and Alexandre Tkatchenko. Density-functional theory with screened van der waals interactions for the modeling of hybrid inorganic-organic systems. *Physical Review Letters*, 108(14):146103, 2012.
- [43] Victor G Ruiz, Wei Liu, and Alexandre Tkatchenko. Density-functional theory with screened van der waals interactions applied to atomic and molecular adsorbates on close-packed and non-close-packed surfaces. *Physical Review B*, 93(3):035118, 2016.
- [44] Alexandre Tkatchenko and Matthias Scheffler. Accurate molecular van der waals interactions from ground-state electron density and free-atom reference data. *Physical Review Letters*, 102(7):073005, 2009.
- [45] Evgenni Mikhailovich Lifshitz, M Hamermesh, et al. The theory of molecular attractive forces between solids. In *Perspectives in Theoretical Physics*, pages 329–349. Elsevier, 1992.
- [46] Eugene Zaremba and Walter Kohn. Van der waals interaction between an atom and a solid surface. *Physical Review B*, 13(6):2270, 1976.
- [47] Alexandre Tkatchenko, Robert A DiStasio Jr, Roberto Car, and Matthias Scheffler. Accurate and efficient method for many-body van der waals interactions. *Physical Review Letters*, 108(23):236402, 2012.
- [48] Alberto Ambrosetti, Anthony M Reilly, Robert A DiStasio Jr, and Alexandre Tkatchenko. Long-range correlation energy calculated from coupled atomic response functions. *The Journal of Chemical Physics*, 140(18):18A508, 2014.
- [49] Xiaosheng Yang, Serguei Soubatch, and F. Stefan Tautz. unpublished data.
- [50] Xi Zhu and Haibin Su. Scaling of excitons in graphene nanoribbons with armchair shaped edges. *The Journal of Physical Chemistry A*, 115(43):11998–12003, 2011.

- [51] Shiyong Wang, Leopold Talirz, Carlo A Pignedoli, Xinliang Feng, Klaus Müllen, Roman Fasel, and Pascal Ruffieux. Giant edge state splitting at atomically precise graphene zigzag edges. *Nature Communications*, 7(1):1–6, 2016.
- [52] Peter Puschnig and Daniel Lüftner. Simulation of angle-resolved photoemission spectra by approximating the final state by a plane wave: from graphene to polycyclic aromatic hydrocarbon molecules. *Journal of Electron Spectroscopy and Related Phenomena*, 200:193–208, 2015.
- [53] BV Senkovskiy, D Haberer, D Yu Usachov, AV Fedorov, N Ehlen, M Hell, L Petaccia, G Di Santo, RA Durr, FR Fischer, et al. Spectroscopic characterization of n= 9 armchair graphene nanoribbons. *physica status solidi (RRL)–Rapid Research Letters*, 11(8):1700157, 2017.
- [54] Boris V Senkovskiy, Dmitry Yu Usachov, Alexander V Fedorov, Danny Haberer, Niels Ehlen, Felix R Fischer, and Alexander Grüneis. Finding the hidden valence band of n= 7 armchair graphene nanoribbons with angle-resolved photoemission spectroscopy. *2D Materials*, 5(3):035007, 2018.
- [55] Bernd Kollmann. Shockley surface states calculated within density functional theory. Master’s thesis, University of Graz, 2014.
- [56] M Feidt, S Mathias, and M Aeschlimann. Development of an analytical simulation framework for angle-resolved photoemission spectra. *Physical Review Materials*, 3(12):123801, 2019.
- [57] Pascal Ruffieux, Jinming Cai, Nicholas C Plumb, Luc Patthey, Deborah Prezzi, Andrea Ferretti, Elisa Molinari, Xinliang Feng, Klaus Müllen, Carlo A Pignedoli, et al. Electronic structure of atomically precise graphene nanoribbons. *ACS Nano*, 6(8):6930–6935, 2012.
- [58] Hajo Söde, Leopold Talirz, Oliver Gröning, Carlo Antonio Pignedoli, Reinhard Berger, Xinliang Feng, Klaus Müllen, Roman Fasel, and Pascal Ruffieux. Electronic band dispersion of graphene nanoribbons via fourier-transformed scanning tunneling spectroscopy. *Physical Review B*, 91(4):045429, 2015.
- [59] Néstor Merino-Díez, Aran Garcia-Lekue, Eduard Carbonell-Sanroma, Jingcheng Li, Martina Corso, Luciano Colazzo, Francesco Sedona, Daniel Sánchez-Portal, Jose I Pascual, and Dimas G de Oteyza. Width-dependent band gap in armchair graphene nanoribbons reveals fermi level pinning on au (111). *ACS Nano*, 11(11):11661–11668, 2017.
- [60] M Willenbockel, D Lüftner, B Stadtmüller, G Koller, C Kumpf, S Soubatch, P Puschnig, MG Ramsey, and FS Tautz. The interplay between interface structure, energy level alignment and chemical bonding strength at organic–metal interfaces. *Physical Chemistry Chemical Physics*, 17(3):1530–1548, 2015.
- [61] Dominik Brandstetter, Xiaosheng Yang, Daniel Lüftner, F Stefan Tautz, and Peter Puschnig. kmap. py: A python program for simulation and data analysis in photoemission tomography. *Computer Physics Communications*, page 107905, 2021.
- [62] Koichi Momma and Fujio Izumi. *VESTA3* for three-dimensional visualization of crystal, volumetric and morphology data. *Journal of Applied Crystallography*, 44(6):1272–1276, Dec 2011.